

**INVESTIGATION OF CONFORMAL
HIGH-IMPEDANCE GROUND PLANES
THESIS**

Michael A. Saville, First Lieutenant, USAF

AFIT/GE/ENG/00M-17

20000815 163

**DEPARTMENT OF THE AIR FORCE
AIR UNIVERSITY**

AIR FORCE INSTITUTE OF TECHNOLOGY

Wright-Patterson Air Force Base, Ohio

APPROVED FOR PUBLIC RELEASE; DISTRIBUTION UNLIMITED.

DTIC QUALITY INSPECTED 4

The views expressed in this thesis are those of the author and do not reflect the official policy or position of the United States Air Force, Department of Defense, or the U.S. Government.

AFIT/GE/ENG/00M-17

INVESTIGATION OF CONFORMAL HIGH-IMPEDANCE GROUND PLANES

THESIS

Presented to the Faculty

Department of Electrical and Computer Engineering

Graduate School of Engineering and Management

Air Force Institute of Technology

Air University

Air Education and Training Command

In Partial Fulfillment of the Requirements for the

Degree of Master of Science in Electrical Engineering

Michael A. Saville, B.S.E.E.

First Lieutenant, USAF

March, 2000

APPROVED FOR PUBLIC RELEASE; DISTRIBUTION UNLIMITED.

INVESTIGATION OF CONFORMAL HIGH-IMPEDANCE GROUND PLANES

Michael A. Saville, B. S. E. E.
First Lieutenant, USAF

Approved:



Maj Peter Collins (Chairman)

14 MAR 00

Date



Lt Col Lawrence Chilton

14 Mar 00

Date



Maj John Crown

14 Mar 00

Date



Dr Andrew Terzuoli

14 MAR 00

Date

Acknowledgements

I offer my sincere gratitude to all the people who helped with this research. Foremost are my research advisor Major Peter Collins (AFIT/ENG) and research sponsor Dr Stephen Schneider (AFRL/SNRP), who each have a genuine passion for research and mentoring. To my committee members Dr Andrew Terzuoli, Lt Col Lawrence Chilton (AFIT/EN), and Major John Crown (AFIT/EN) who may believe their part was small in the overall effort, but I always reached a milestone after meeting with them.

Sincere thanks to Dr John Mehr (Mission Research Corporation) and Mr James Mudd (AFRL/SNRP), who patiently fabricated antennas, graciously shared measurement experiences and techniques, and kindly clarified “theory versus measurement.” If it were not for their guidance I would still be making measurements.

Recognition of Dr Jill Ullet (Georgia Tech Research Institute) and Mr Stan Bashore (AFRL/SNS) for providing and assisting me with the focused beam measurement facility. To Mr Charlie McNeely (AFIT/ENG), thanks for allowing me to make a mess of the microwave lab and clean it up in an untimely manner. My thanks to the AFIT model shop for an exceptional job making the surface wave test fixture.

To my classmates 1Lt Geoffrey Akers, Capt Daniel Richards, and Capt Scott Rupert for solving numerous problems by just listening and Dr Daniel Sievenpiper for placing his dissertation on the internet.

Finally and most importantly, to my wife, Deysi, and children, Michael, Kristen, and Caitlyn. There are not words to express enough thanks to you for your love, support, and patience during the long months that I was “away” at AFIT.

Michael Andrew Saville

Table of Contents

Acknowledgements.....	iv
List of Figures.....	viii
List of Tables	xii
Abstract.....	xiii
1. Introduction.....	1
1.1. Motivation.....	2
1.1.1. New technology.....	2
1.1.2. Demonstrated for limited applications.....	2
1.2. Research Goal.....	3
1.3. Overview.....	3
2. Background	4
2.1. The high-impedance ground plane defined.....	4
2.2. Photonic Crystals.....	8
2.2.1. Photonic band engineering.	8
2.2.2. Classes of photonic crystals.....	9
2.2.3. 2-D VS 3-D crystals.....	11
2.2.4. Analysis of photonic crystals.....	12
2.2.5. Photonic Crystal Measurements	16
2.3. Planar High-Impedance Ground Planes.....	17
2.3.1. Surface wave suppression.....	18

2.3.2. Effective medium model and frequency bandwidth.....	24
2.3.3. Antenna Performance	25
2.4. Conformal antenna research.....	26
2.5. Chapter Summary	27
3. Methodology	28
3.1. Method to achieve research goal.....	28
3.2. Computational techniques.....	30
3.2.1. Finite-difference time domain software.....	31
3.2.2. Periodic moment method	33
3.3. Design and fabrication of thumbtack HIGP.....	37
3.3.1. Choice of patterns	37
3.3.2. Materials	37
3.3.3. Layout.....	37
3.3.4. Fabrication.....	40
3.4. Reflection of high-impedance ground planes.....	41
3.4.1. Reflection measurements.....	42
3.5. Measuring surface wave suppression.....	49
3.5.1. Surface wave coupling on the planar HIGP.....	50
3.5.2. Surface wave coupling of singly curved HIGP.....	52
3.6. Antenna pattern measurements.....	54
4. Results and Analysis	58
4.1. Computational Analysis.....	58
4.1.1. Finite difference time domain.....	58

4.1.2. Periodic moment method	66
4.2. Reflection measurements.....	77
4.2.1. Georgia Tech Research Institute (GTRI) Focused Beam.	77
4.2.2. AFIT arch.	90
4.2.3. Waveguide Probe.....	92
4.3. Surface wave measurements.....	93
4.3.1. Planar HIGP surface wave coupling.....	93
4.3.2. Singly curved HIGP surface wave coupling.....	98
4.4. Antenna pattern measurements.....	106
4.4.1. Antenna selection and design.	106
4.4.2. Folded monopole over PEC, Duroid substrate, and HIGP.....	106
5. Conclusions and Suggestions for Further Work	111
5.1. Review of objectives.....	111
5.2. Conclusions.....	111
5.3. Recommendations.....	112
5.3.1. Computational electromagnetics.....	112
5.3.2. Effective medium model.....	112
5.3.3. Broadband designs.....	112
5.3.4. Antenna applications.	113
References.....	129
Vita.....	131

List of Figures

Figure 1. Ground plane in different antenna configurations [1]. (a) Parabolic and paraboloid reflector antennas and (b) microstrip patch antennas.	4
Figure 2. Reflection of magnetic and electric fields determined from boundary conditions and right-hand rule. (a) PEC, and (b) PMC.	5
Figure 3. Electric currents over infinite PEC and PMC ground planes. (a) Images shown with currents, and (b) radiation pattern of dipoles over respective ground plane and without ground plane. PEC image cancels electric current, but PMC image doubles radiation pattern.	6
Figure 4. “Thumbtack” high-impedance ground plane [18]. Side view on the left and top view on the right.	7
Figure 5. Brillouin zones for the body centered cubic (BCC), and face centered cubic (FCC).	9
Figure 6. Diamond lattice PC’s fabricated with printed circuit boards. (a) MDPC with metal islands that form capacitive bonds between metal elements [11], and (b) Metallic PC with metal posts connecting the metal elements to form conductive bonds between elements [10]....	11
Figure 7. Typical dispersion diagram for a 2-D photonic crystal [19] with first Brillouin zone.	12
Figure 8. Seven layer PBG reflector [17]. (a) Transverse view of reflector showing alternating layers of dielectric and air to form PBG structure, (b) Computational domain of 2-D model which includes the focal point in the model, (c) 3-D model which substitutes an equivalent surface impedance model for the PBG.	15
Figure 9. Textured surfaces. (a) Bumpy metal surface for suppressing surface waves, (b) corrugated block with quarter wavelength depth that provides high impedance, and (c) <i>Thumbtack</i> , 2-D photonic crystal that suppresses surface waves and has high impedance [18].	17
Figure 10. Coplanar waveguide on silicon substrate [21]. (a) Top view showing signal line, ground lines, and open area in glass substrate, and(b) cross sectional view showing removed portion of silicon substrate after micromachining.	19

Figure 11. Cavity backed printed antenna. (a) Single spiral element, and (b) cross sectional view of absorber filled cavity	20
Figure 12. Parallel circuit model of Sievenpiper's patented two layer thumbtack design [18].....	22
Figure 13. Ku-band patch antenna surrounded by the 2-D PBG lattice [20].....	26
Figure 14. Horizontal monopole radiating over a high-impedance ground plane.	28
Figure 15. Square pattern HIGP modeled as thin slots in PMM. (a) Pattern with reference element highlighted, and (b) piece-wise sinusoid current modes on reference element. Piecewise sinusoidal current modes overlap to simulate the infinite slot length.....	35
Figure 16. Hexagon pattern HIGP modeled as thin slots in PMM. (a) Pattern with reference element highlighted, and (b) piece-wise sinusoid current modes on reference element.....	36
Figure 17. Layouts for fabrication. Dielectric is duroid 5880 ($\epsilon_r=2.51$). (a) Square pattern, and (b) hexagon pattern.	39
Figure 18. Planar high-impedance ground plane after production. (a) Test samples side by side, and (b) close up of element patterns.....	41
Figure 19. GTRI Focused beam system connected to HP8510 Network Analyzer. As shown, configured for normal incidence reflection and/or transmission. Courtesy of the Signatures Technology Branch, Air Force Research Laboratory.	43
Figure 20. Sources of errors for the GTRI Focused beam system. Courtesy of the Signatures Technology Branch, Air Force Research Laboratory, Wright-Patterson Air Force Base, Ohio.....	44
Figure 21. Far field reflection measurement set-up. Shown are the HP8510C Network Analyzer, two standard gain horns, and a copper reference sheet.	46
Figure 22. Waveguide probe technique shown with square element HIGP. Also shown are the calibration short, offset, and load with the Ku-band waveguide probe.	48
Figure 23. Surface wave experiment configuration. (a) Test fixture, (b) sources of errors, and (c) cross-sectional view of test fixture.	51
Figure 24. Test body for conformal ground plane surface wave measurement. Can also be used for antenna measurements. Shown is the original drawing of the Top, Front, and Side view.....	53

Figure 25. Log-periodic dipole antenna layout. Small inner circles are holes for coaxial feed, larger circles are copper pad for solder connection.	55
Figure 26. The Radiation and Scattering Compact Antenna Laboratory (RASCAL), Applied Aperture and Receiver Technology Branch, Air Force Research Laboratory, Wright-Patterson Air Force Base, Ohio.....	56
Figure 27. FDTD 2-D grid and boundary.	59
Figure 28. Computational domain for plane wave excitation.	60
Figure 29. Plane wave incident on metal plate. (a) Incident wave before striking plate, (b) incident wave as it just strikes the plate, (c) diffraction occurs at the plate edge after reflection of the wave, (d) numerical dispersion and instability effects begin at the bottom of the grid, (e) and instability overcomes the two regions.....	62
Figure 30. Time domain signal of incident plane wave. There are 3660 time step.....	64
Figure 31. FDTD model of square high-impedance ground plane. Shown are the measurement probes, the domain size, the ground plane, and the projection of the E-field magnitude at one time step.	65
Figure 32. PMM phase response of Γ for square pattern. (a) TM polarization, and (b) TE polarization.	68
Figure 33. PMM phase response of Γ for hexagon pattern. (a) TM polarization, and (b) TE polarization.....	70
Figure 34. PMM comparisons of Hex and Square phase response for TM and TE polarization. (a) Normal incidence, (b) 35 degrees incidence, (c) 60 degrees incidence, and (d) 70 degrees incidence.....	73
Figure 35. Measured phase response of Γ for square and hexagon using the GTRI focused beam system. (a) TM/square element, (b) TE/square element, (c) TM/hexagon element, and (d) TE/hexagon element.	79
Figure 36. Focused beam comparisons of Hex and Square phase response for TM and TE polarization. (a) Normal incidence, (b) 35 degrees incidence, (c) 60 degrees incidence, and (d) 70 degrees incidence.....	82
Figure 37. Electric field excitation of charge on HIGP elements.	86
Figure 38. Comparison of PMM and measured phase of Γ	87

Figure 39. Sensitivity of f_r for varying gap and lattice spacing. (a) f_r increasing with increasing gap size, and (b) f_r decreasing with increasing lattice constant.....	89
Figure 40. Far field reflection measurement results at normal incidence. (a) Square pattern, and (b) hexagon pattern.	90
Figure 41. Comparison of PMM, focused beam, and far field reflection data. Data shown is for the square pattern at normal incidence.	91
Figure 42. Typical waveguide probe measurement of Γ . (a) Hexagon pattern, and (b) square pattern.	93
Figure 43. TM coupled surface waves on planar hexagon HIGP. (a) measurement 1, (b) measurement 2, and (c) measurement 3.....	95
Figure 44. TE surface wave coupling. On planar (a) duroid 5880, (b) PEC, (c) hexagon HIGP, and (d) square HIGP.....	98
Figure 45. Doghouse test body for surface wave measurements. Shown with high-impedance ground plane in window, and reference plate.....	99
Figure 46. TM surface wave coupling on conformal ground planes. (a) Duriod 5880, (b) PEC, (c) hexagon HIGP, and (d) square HIGP.....	101
Figure 47. TM surface wave coupling on pec plate with 6 inch probe separation.	102
Figure 48. TE surface wave coupling. On conformal (a) duroid 5880, (b) pec, (c) hexagon HIGP, and (d) square HIGP.	105
Figure 49. Frequency scan of LPD antenna with different feed locations.....	107
Figure 50. Frequency scan of monopole antenna above different ground planes. (a) Duriod, (b) pec, (c) hexagon HIGP, and (d) square HIGP.	109

List of Tables

Table 1. List of tasks to achieve goal.....	30
Table 2. Test matrix for FDTD simulations.....	33
Table 3. Test matrix for PMM analysis	35
Table 4. Test procedure for GTRI reflection measurements.	45
Table 5. Test matrix for far field reflection measurement	47
Table 6. Test matrix for surface wave measurements.....	52
Table 7. Test procedure for planar surface wave measurement.....	52
Table 8. Log-periodic antenna design lengths.	55
Table 9. Test matrix for antenna measurements.	57
Table 10. Symbol definitions for plotted results.....	67
Table 11. Results of PMM test matrix.....	75
Table 12. F-tests for PMM resonant frequency model.	76
Table 13. Least square mean resonant frequencies and standard error of PMM model... ..	76
Table 14. F-tests for PMM bandwidth model.....	77
Table 15. Results of focused beam test matrix.	84
Table 16. F-tests for focused beam resonant frequency results.	84
Table 17. Least square mean resonant frequencies and standard error of measured data.	85
Table 18. F-tests for focused beam BW results.	87
Table 19. Table of comparisons of f_r for PMM and measured data.	88
Table 20. Results of far field reflection measurement.....	91
Table 21. Mean resonant frequency of waveguide probe measurement.....	92

Abstract

Applique antennas are a long range vision for military vehicles because they are lighter, quicker to replace, less expensive, and can have better performance than conventional antennas. Two newly reported high-impedance ground planes have potential to begin the realization of the applique antenna vision and each is investigated for use with thin conformal antenna structures. Bistatic reflection measurements completely characterize the high-impedance region of planar, thumbtack high-impedance ground planes, and periodic moment method models validate the measurement results. Rigorous planar and conformal surface wave coupling measurements clarify the reported photonic band gap behavior of the thumbtack high-impedance ground plane, and give evidence that the published surface wave suppression results may in fact be inconclusive.

In addition, an analysis of variance test identifies the optimum antenna frequency for horizontal wire antenna applications. Broadband antenna applications are explored using a printed log-periodic wire antenna, but unpredicted losses outside the high-impedance region produced inconclusive results and prevented the conformal antenna measurements.

INVESTIGATION OF CONFORMAL HIGH IMPEDANCE GROUND PLANES

One cannot escape the feeling that these mathematical formulas have an independent existence and an intelligence of their own, that they are wiser than we are, wiser even than their discoverers, that we get more out of them than was originally put into them.

– Heinrich Hertz on Maxwell's Equations

1. Introduction.

Over 120 years ago James Clerk Maxwell derived the equations modeling electromagnetic wave propagation and with those equations, Heinrich Hertz built the first antenna to demonstrate the existence of electromagnetic waves. Today, military and civilian life alike enjoy and even depend on control of the entire spectrum through a plethora of electromagnetic applications such as direct broadcast satellite, wireless internet, personal communication, medical imaging and treatment, air traffic control, and global positioning systems. The United States military exploits the electromagnetic spectrum to lead the world in the development of communication, navigation, remote sensing, guidance and control, and fatally accurate smart weapons. A principal reason for sustaining superiority is that military researchers continually investigate scientific discoveries and capitalize on new technologies.

1.1. Motivation.

1.1.1. New technology.

The recently reported high impedance ground plane is one such discovery that has the potential to radically improve the performance of many antennas designed for military weapon systems. This novel ground plane has been reported to suppress electromagnetic surface waves (a recurring problem for designing conformal antennas, large printed antenna arrays, and some stealth applications) and it also behaves as a perfect magnetic conductor (+1 E-field reflection coefficient) within a select frequency band. Unlike the perfect electric conductor (-1 E-field reflection coefficient), a simple metal surface used with most antennas, the PMC does not short tangential electric fields at the surface of the ground plane. Potential advantages of the high impedance ground plane include improved antenna patterns, doubled antenna gain, and cheaper and simpler fabrication of conformal antennas.

1.1.2. Demonstrated for limited applications.

Since the ground plane was initially demonstrated for planar printed antennas with narrow frequency bandwidth, further investigation is needed to understand the potential for use with conformal antennas and antennas of broad frequency bandwidth. Antennas for military aircraft and missiles are typically studied to determine how well they will perform when conformed to the shape of a wing edge or fuselage. Also, aircraft often have several different antennas for communications, navigation, and threat warning, but each may require operation over several frequency bands. Therefore, broadband antennas are of primary interest to the designers of these types of systems.

1.2. Research Goal.

The research goal is to determine if the newly reported high-impedance ground plane is suitable for conformal or structurally integrated antennas. Applying a small amount of curvature is not expected to significantly alter the behavior of the new ground plane, therefore it is believed that a non-planar antenna placed directly above a conformal high-impedance ground plane will have higher gain and smoother radiation patterns.

1.3. Overview.

Chapter two is a review of photonic crystal technology and the development of the high-impedance ground plane, conventional techniques to suppress surface waves for antennas and stealth applications, and modern conformal antenna research. Chapter three discusses the details of the different computational and measurement methods used to determine the impact of a single radius of curvature on the performance of the reported high-impedance ground plane. Chapter four provides qualitative analysis of the planar and curved ground plane when used as an antenna ground plane, and the statistical analysis of the results to determine limitations of the conformal high-impedance ground plane. Chapter five provides conclusions and recommendations for further research based on the analysis of chapter four.

2. Background

2.1. The high-impedance ground plane defined.

Metals are nearly perfect electric conductors and are commonly used as electric ground planes with reflector and microstrip printed antennas, Figure 1. The reflector directs radiating energy to shape the beam and increase antenna gain.

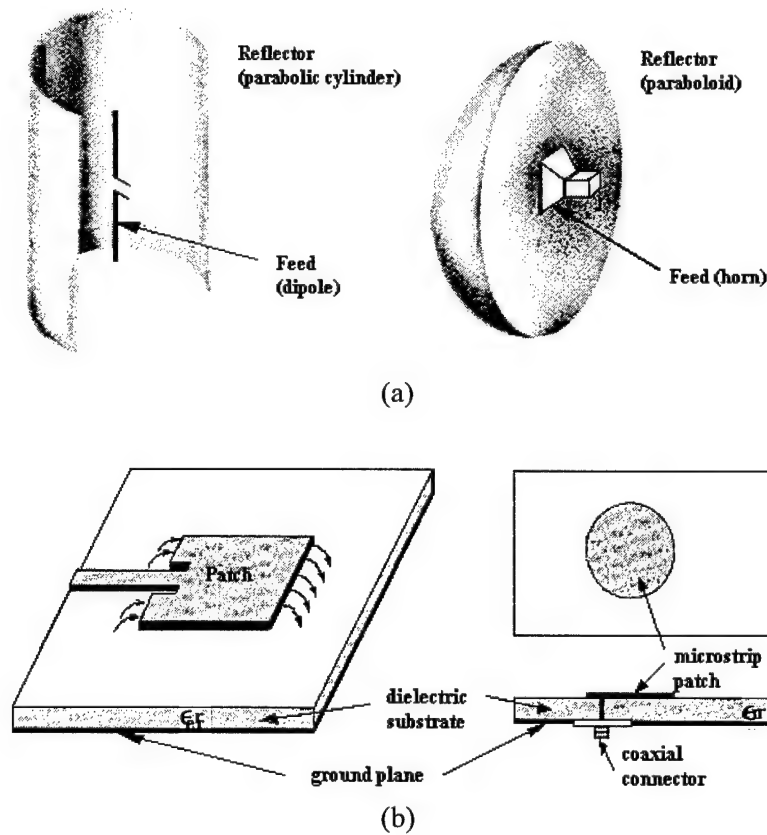


Figure 1. Ground plane in different antenna configurations [1]. (a) Parabolic and paraboloid reflector antennas and (b) microstrip patch antennas.

According to the time harmonic Maxwell Equations for lossless homogeneous media and the boundary conditions for a perfect electric conductor (PEC), the tangential electric field (E-field) must equal zero at the boundary between a dielectric–PEC interface because the tangential E-fields are continuous across the boundary, i.e.

$$E_{t1} = E_{t2} = 0, \quad (1)$$

where E_{t1} is the tangential E-field on one side of the boundary, and E_{t2} is the zero E-field on the PEC side of the boundary. The result of Equation (1) is that the tangential electric fields reflect off a PEC surface completely but have a 180-degree change in phase at the boundary [1].

Conversely, the perfect magnetic conductor (PMC) has the same behavior for tangential magnetic fields but not for electric fields. Thus, tangential electric fields reflect off a PMC completely but do not have a phase change at the boundary, (Figure 2).

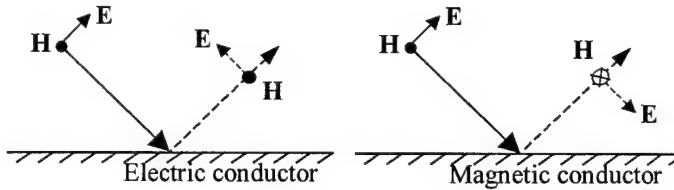


Figure 2. Reflection of magnetic and electric fields determined from boundary conditions and right-hand rule. (a) PEC, and (b) PMC.

Another way to look at the PMC is to consider what happens to a horizontal dipole antenna when placed above a PEC versus a PMC. Figure 3 (a) shows the dipoles and their images (from the boundary conditions) for both ground planes and how the radiation pattern is improved for the horizontal dipole above a PMC. The PMC has in phase image currents which

add to the dipole current, thus doubling the radiated power. However, the PEC has an out of phase image and the currents cancel, resulting in no radiated power. Practical antennas are not directly placed over the ground plane, so Figure 3 (b) shows a small pattern for the PEC case. Antennas that use PEC ground planes require that the ground plane be placed a quarter wavelength away from the antenna, thus reducing the antenna efficiency for all other frequencies.

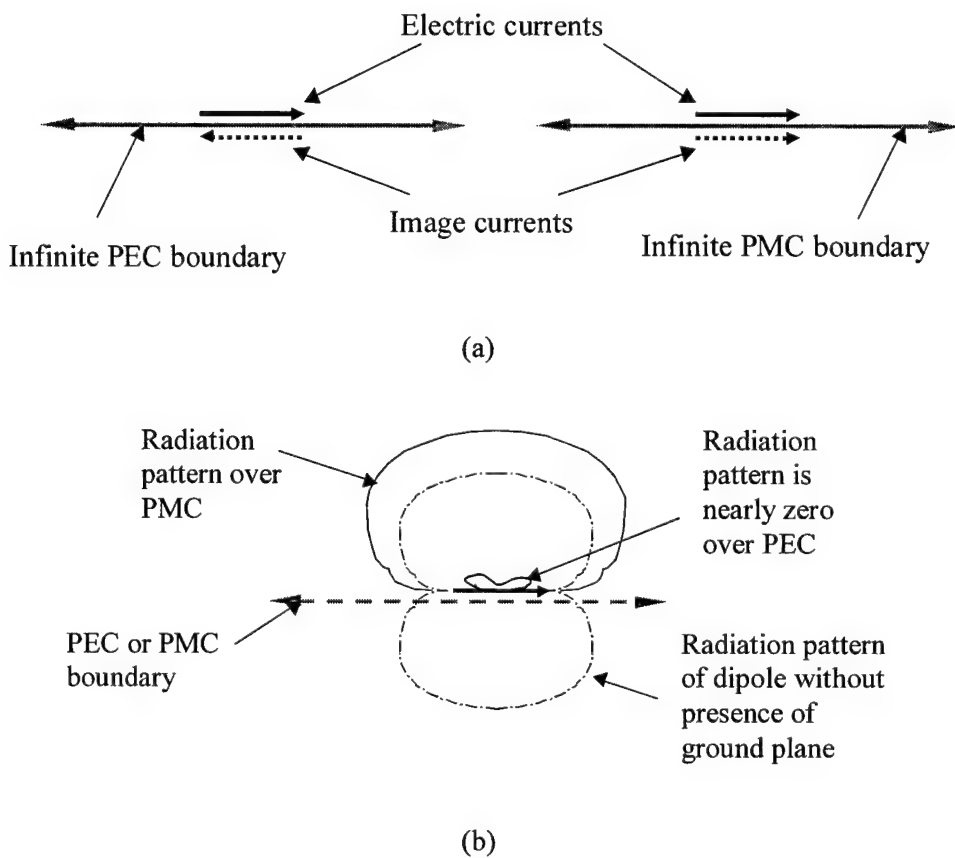


Figure 3. Electric currents over infinite PEC and PMC ground planes. (a) Images shown with currents, and (b) radiation pattern of dipoles over respective ground plane and without ground plane. PEC image cancels electric current, but PMC image doubles radiation pattern.

Although PEC's are easily approximated with metal surfaces, the PMC has limited use because there are no simple, naturally occurring materials that have PMC characteristics over large bandwidths. Materials with large permittivity (heavy dielectrics) are sometimes used to approximate PMC's but the heavy dielectric is inherently lossy to EM wave propagation.

A recently reported high-impedance ground plane behaves like a PMC just as a metal surface behaves as a PEC [3]. It is a two dimensional, periodic structure, shown in Figure 4. The metal islands are connected to the ground plane with plated through holes and the overall effect is to create a high, surface impedance for electromagnetic waves of discriminate frequencies. Since the theory and metrology of the new ground plane's design is rooted in photonic crystal technology, a review of the science is warranted.

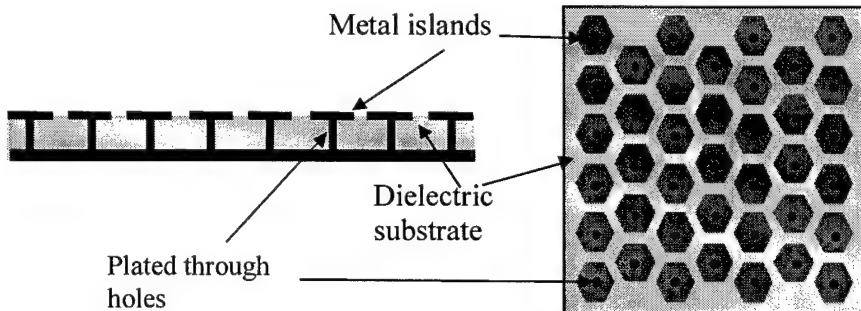


Figure 4. "Thumbtack" high-impedance ground plane [18]. Side view on the left and top view on the right.

2.2. Photonic Crystals.

2.2.1. Photonic band engineering.

“Photonic Band Engineering,” a phrase coined by the US Army Research Office (USARO) [3], is the engineering of periodic structures that block electromagnetic wave propagation. A photonic band gap (PBG) is defined as the band of frequencies for which EM waves do not propagate.

Over a decade ago, Yablonovitch [4] suggested that the quality, or Q, of a semiconductor laser cavity might be enhanced if one could prohibit spontaneous emission over the laser’s spectral bandwidth. He hypothesized that a three dimensionally periodic structure could inhibit electromagnetic wave propagation. From this inception, he and others spent several years searching for such a geometric shape that would exhibit a complete photonic band gap; i.e., a photonic band gap for all directions of propagation [5]. The partial photonic band gap, or prohibition for some directions, was seen throughout many of the early designs using body center and face center cubic crystal structures.

Yablonovitch [6] explains that the face center cubic crystal is preferred because it’s Brillouin zone deviates the least from a sphere. The Brillouin zone is the unit cell of the reciprocal lattice [7] and the reciprocal lattice is obtained by transforming the spatial lattice vectors to wave vectors. Figure 5 shows the Brillouin zones for the body center and face center cubic crystals and how the face center cubic crystal more closely resembles a sphere. Thus, a complete band gap could be achieved in all directions of space. In 1990 and 1991, groups at Iowa State [9] and UCLA [8], respectively, demonstrated theoretically and experimentally a complete photonic band gap for a diamond crystal lattice. Although the diamond structure provided only

part of the requirements to make a photonic crystal, it was not difficult to find materials that had the right electrical properties from which to build the crystal.

Today photonic band engineering encompasses a broad range of microwave, millimeter wave, and optical wave applications such as antenna reflectors and ground planes, transmission line substrates, microwave amplifiers, extremely high Q laser cavities, and high efficiency light emitting diodes. Of particular interest is the use of photonic crystals as printed antenna ground planes and substrates because the crystals do not allow EM waves to propagate within their structure. Therefore, the energy is not lost in the substrate and the radiation pattern is improved because the ground plane edges do not scatter surface waves.

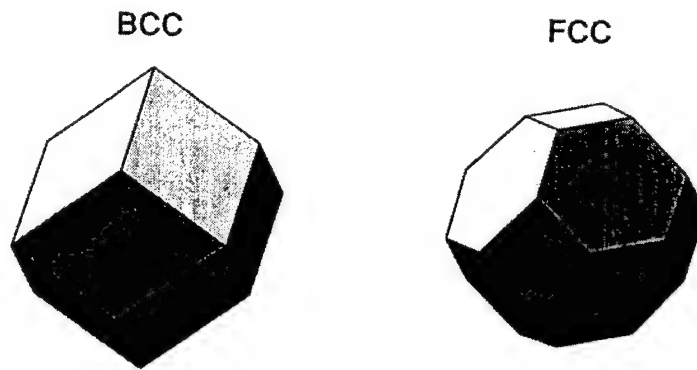


Figure 5. Brillouin zones for the body centered cubic (BCC), and face centered cubic (FCC).

2.2.2. Classes of photonic crystals.

Schloer [10] gives a thorough review of photonic crystal (PC's) history, theory, and applications for antenna reflectors. In detail, he describes the three classes of photonic crystals: metallic, dielectric, and metallocodielectric (MDPC).

To summarize the differences between the three classes from [10],

The first radio frequency (RF) electromagnetic crystals were all metal and all dielectric structures. They consisted of dielectric blocks drilled with holes, wire meshes, and metal grids sandwiched between dielectric slabs. The MDPC's are the most advanced PC and are fabricated with a blend of dielectric and metal to make the crystal unit cell smaller than a wavelength.

The all-dielectric PC has a lattice constant on the order of one wavelength. Thus, it's band gap size is restricted, and the structure must be very large and heavy to achieve usable stop bands. The metallic PC overcomes these limitations because the cutoff frequency occurs for lattice constants on the order of one-half wavelength. However, aside from the finite size, there is no control over the lower frequency band edge. This is the distinguishing feature of a MDPC, which does have a controllable upper and lower frequency band edge. The basic equations for estimating the upper and lower band edges are

$$f_{lower} \approx \frac{1}{2\pi\sqrt{LC}}, \quad (2)$$

$$f_{upper} \approx \frac{c_o}{a\sqrt{\epsilon_r}}, \quad (3)$$

where L and C are the inter-element inductance and capacitance, c_o is the speed of light, a is the lattice constant, and ϵ_r is the relative permittivity of the dielectric material.

An additional feature of each of the different classes is the thickness of the PC's.

Typically, the number of layers depends on the amount of rejection desired in the stop band.

Schloer [10], and Sievenpiper et al. [11] made three layer diamond lattice crystals (Figure 6).

Although each is a different class of PC, both demonstrate complete PBG behavior because they form complete three-dimensional crystals.

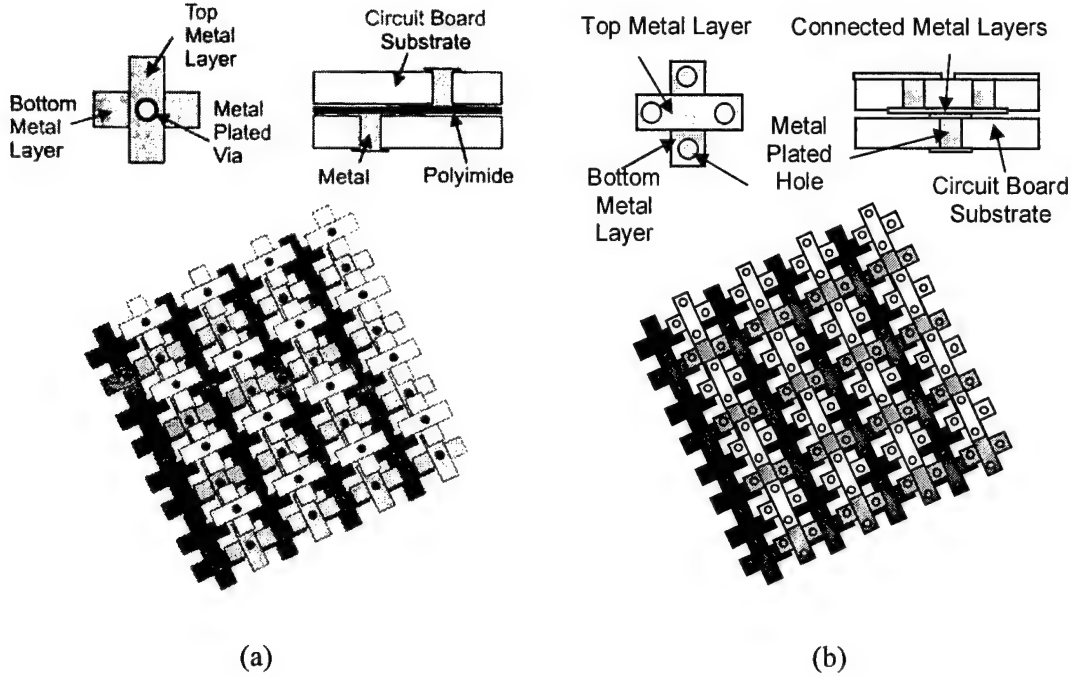


Figure 6. Diamond lattice PC's fabricated with printed circuit boards. (a) MDPC with metal islands that form capacitive bonds between metal elements [11], and (b) Metallic PC with metal posts connecting the metal elements to form conductive bonds between elements [10].

2.2.3. 2-D VS 3-D crystals.

Joannopoulos [12] steps through the wave propagation theory for one, two and three dimension PC's. Three-dimensional PC's allow complete band gaps, but are more difficult and time consuming to fabricate than the 2-D PC. The choice of 3-D vs. 2-D photonic crystals depends on the application. For high Q cavities, the 2-D PC is sufficient if appropriately designed [3]. The 2-D PC is also easier to analyze and led to the surface impedance model used to design the high-impedance ground plane.

2.2.4. Analysis of photonic crystals.

Wave propagation through electromagnetic crystals, or photonic crystals, is typically demonstrated with a reciprocal space dispersion diagram. Figure 7 shows the complete bandgap where the letters X, M, and Γ map the smallest Brillouin zone in reciprocal space. They represent the directional wave vectors and show that, for all possible wave vectors, there does not exist a frequency at which EM waves propagate. The heavy dotted lines represent TE and TM modes. The gray region between the lowest pair of lines represents the complete band gap. It is possible for another band gap to exist between the higher pair of lines.

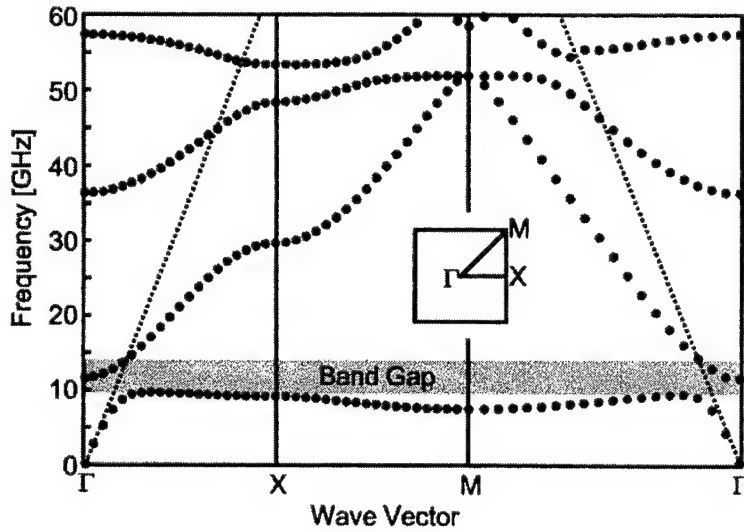


Figure 7. Typical dispersion diagram for a 2-D photonic crystal [19] with first Brillouin zone.

These diagrams have been computed using several methods to include full-wave analysis computer codes such as moment-method and Finite-Element Method (FEM). The workhorse has been the Finite-Difference Time Domain (FDTD), because the computational time can be less

than that for moment-method codes and FDTD gives direct insight into the EM wave propagation over time. Also, hybrid methods consisting of a combination of surface impedance models and FDTD have helped developed the high-impedance ground plane. The FDTD model used is based on the Yee algorithm as described by Taflove [26]. The Periodic Moment-Method (PMM) is a moment-method technique developed by The Ohio State University [27].

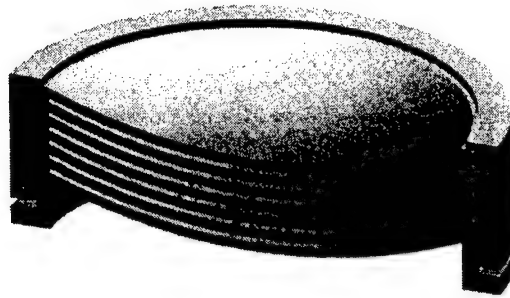
Boroditsky et al. [13] explained that the computational domain for FDTD can be reduced to a single unit cell if appropriate periodic and absorbing boundary conditions are used. They used a 2-D dielectric block perforated with holes, Block boundary conditions on the side walls, and absorbing boundary conditions on the top and bottom domain walls. From the FDTD code they calculated the dispersion diagram for the PC and showed this particular photonic crystal to be a good candidate for high Q LED nanocavities. Kelly et al. [14] used FDTD to analyze photonic band structures of finite thickness. They used a 2-D structure consisting of dielectric rods and periodic boundary conditions to simulate an infinite PBS layer. They achieved very good agreement between the measurement and simulation results. Colburn and Rahmat-Samii [15] demonstrated improved directivity of a linear taper slot antenna with a FDTD model. They also used a two dimensional structure but had to use very small Yee cell sizes of 1/40 and 1/80 wavelengths. The small cell sizes increase the mesh density, the required memory, and the computation time.

Besides the FDTD, the periodic moment-method has seen limited use because of its applicability to 2-D periodic structures. Barlevy et al. [16] used PMM to analyze screens of tripole elements. Their model was limited to stacked planar screens. The computational time exceeded an hour for each frequency of interest so for successive frequencies, they used an interpolation technique to fill the impedance matrix. They explored capacitive loading of closely

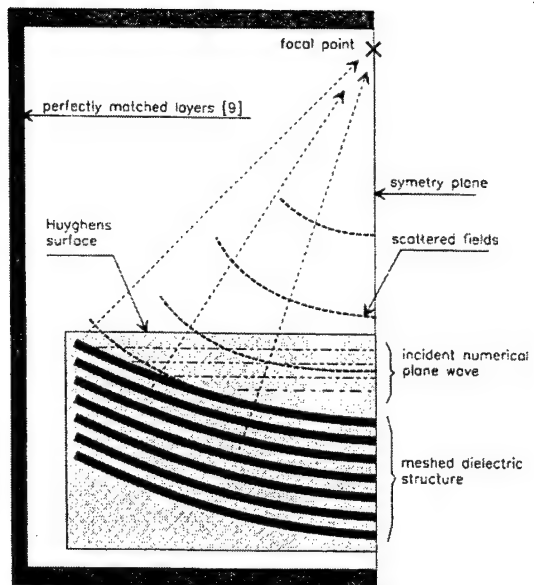
spaced screens and used a model very similar to the model used for the 3-D MDPG reported by Sievenpiper et al [11].

However, almost all of the published results are for planar PC's. One report of a curved photonic crystal structure used FDTD to model a seven layer parabolic PBG reflector [17]. This work was unique because the reflector was first modeled as a 2-D structure based on the transverse view of the reflector. Figure 8 (a), (b) shows the transverse section of the reflector and the corresponding 2-D FDTD computational domain. The two dimensional PBG reflector had better gain and beamwidth performance than a metallic reflector and these results laid the ground work for a 3-D model of the PBG reflector. However, when they tried to include the focal point of the reflector in the 3-D computational domain, the mesh density became too immense for a straight FDTD model. As an alternative approach, they substituted an equivalent surface impedance model for the PBG reflector, Figure 8(c), excluded the focal point from the domain, and extrapolated the EM fields in time for evaluation of the signal at the focal point. The FDTD results had good agreement with measured results for a narrow bandwidth. This example shows the power of a surface impedance model.

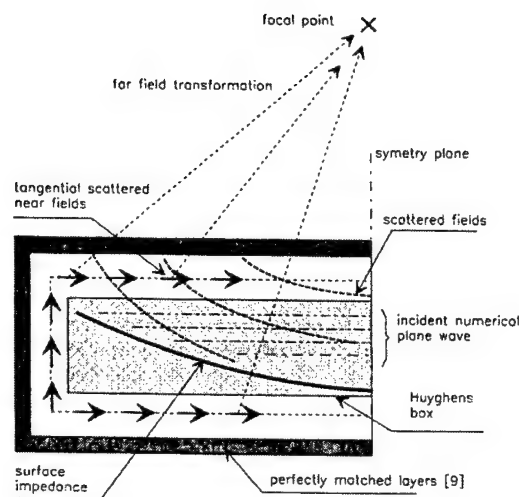
One final note regarding the published FDTD models is that the reported codes required additional techniques, such as Block boundary conditions and perfectly matched layers. In other words, each code was a homebrew so to speak.



(a)



(b)



(c)

Figure 8. Seven layer PBG reflector [17]. (a) Transverse view of reflector showing alternating layers of dielectric and air to form PBG structure, (b) Computational domain of 2-D model which includes the focal point in the model, (c) 3-D model which substitutes an equivalent surface impedance model for the PBG.

2.2.5. Photonic Crystal Measurements

Although the computational techniques have shown good results, development of photonic crystal technology has grown primarily from experimentation. Early photonic band gap structures were scaled to sizes appropriate to microwave wavelengths because the sub-micron size of optical structures are difficult and costly to fabricate. Photolithography and micromachining are the most common ways to build optical devices, but microwave devices can be manufactured using simpler and less expensive techniques ranging from the drilling of holes in dielectric blocks to the stacking of printed circuit boards (PCBs) [10]. In addition the measurement equipment is less sophisticated and often simpler to use.

Typically, the transmission and reflection coefficients are measured to identify the frequency bandgap of the PC, and antenna radiation patterns are measured to demonstrate improved radiation pattern, i.e., surface wave suppression. If an antenna is placed over a finite ground plane the edges of the ground plane are illuminated by the antenna radiation pattern which cause fringing and perturbations to the radiation pattern [1]. Also, the antenna gain is reduced because the edge scatters the radiating energy away from the main beam. When a PC is used as a reflecting, finite ground plane, surface waves are suppressed and the antenna pattern does not illuminate the reflector edges. Instead, the energy is reflected above the ground plane and it adds to the radiation pattern and antenna gain.

This research is mostly experimental, therefore the different techniques for measuring reflection, transmission, and surface wave suppression are deferred to the next chapter.

2.3. Planar High-Impedance Ground Planes.

Although high impedance ground planes are not a new idea, it is difficult to fabricate such a structure that is broadband, nearly lossless, lightweight, and conformable. Sievenpiper et al. [18] compare their patented ground plane to traditional textured surfaces like bumpy metal surfaces and corrugated metal surfaces, shown in Figure 9. Electric fields that traverse a bumpy surface are scattered by the bumps, thus EM waves do not propagate along the surface.

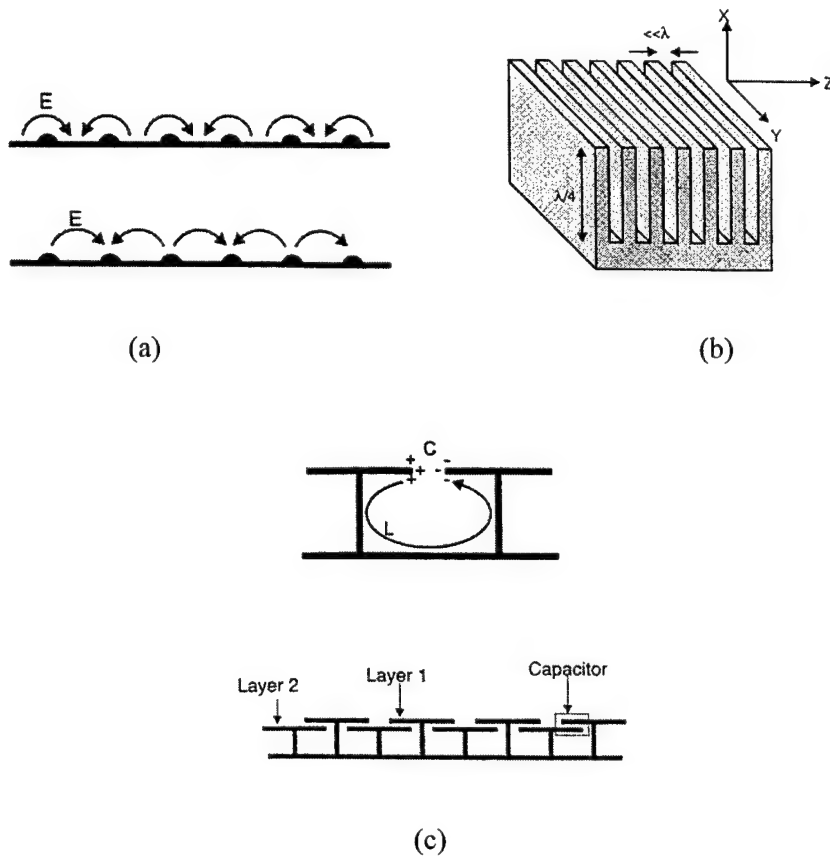


Figure 9. Textured surfaces. (a) Bumpy metal surface for suppressing surface waves, (b) corrugated block with quarter wavelength depth that provides high impedance, and (c) *Thumtack*, 2-D photonic crystal that suppresses surface waves and has high impedance [18].

The corrugated metal surface has cuts that are a quarter wavelength deep. From transmission line theory, a short appears as an open when observed a quarter wavelength away. This is analogous to an infinite, or very high impedance. However, the corrugated block is thick for microwave frequencies and only has a high impedance at a single frequency. The Sievenpiper et al design, shown in Figure 9 (c), uses planar bumps and posts that work similarly to corrugations.

2.3.1. Surface wave suppression.

Essentially, the HIGP was designed to suppress the dominant TM_0 modes, i.e., surface waves, in microstrip-based planar antennas fabricated on high-dielectric substrates [20]. Higher dielectric materials, such as silicon, gallium-arsenide, and indium-phosphorus, are commonly used with monolithic microwave integrated RF circuits because of the small sizes that are achievable. However, severe losses are incurred due to attenuation by the dielectric substrate, resulting in reduced signal strength, and reduced antenna gain and efficiency. Also, higher cross-polarization and mutual coupling occur between elements of antenna arrays.

Other techniques are available for reducing surface waves, but usually at a cost of size, structural robustness, or reduced radiated power. Tea et al. [21] reduced surface wave attenuation in a coplanar waveguide transmission line from ~ 35 dB/cm to 2-4 dB/cm. Figure 10 shows the amount of silicon substrate they removed with micromachining techniques. For CMOS sized circuitry this is an acceptable technique because the suspended transmission line is still sturdy. However, larger structures need the support from the substrate, and, in the case of microstrip-based narrowband antennas, the dielectric substrate supports both the antenna and ground plane. The ground plane must be placed a quarter wavelength away from the antenna so that reflecting energy returns to the antenna in-phase and constructively adds to the radiating

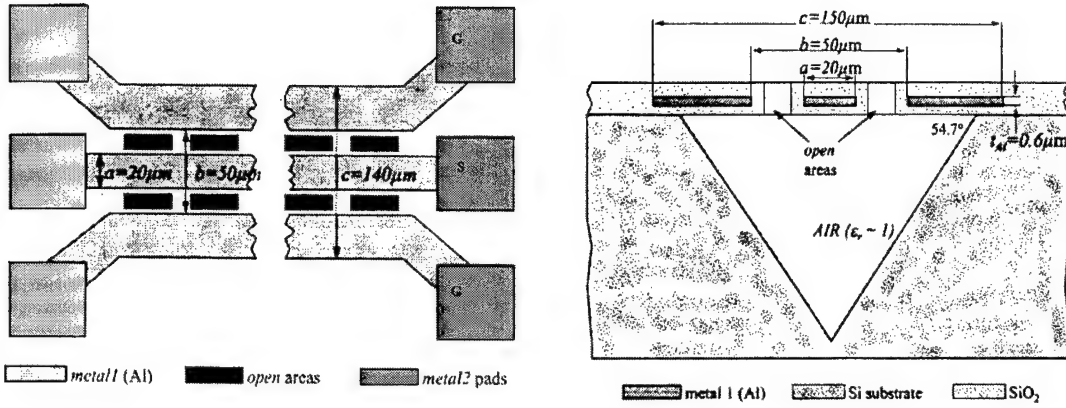


Figure 10. Coplanar waveguide on silicon substrate [21]. (a) Top view showing signal line, ground lines, and open area in glass substrate, and(b) cross sectional view showing removed portion of silicon substrate after micromachining.

pattern. The higher dielectric constant allows smaller distances because the guided wavelength is inversely proportional to the square root of the permittivity, i.e.

$$\lambda_g = \frac{\lambda_0}{\sqrt{\epsilon_r}}, \quad (4)$$

where λ_0 is the free space wavelength, and ϵ_r is the permittivity constant. Equation (4) implies that broadband microstrip-based antennas can not be designed in the same fashion because the ground plane does not move with respect to the antenna. For some wavelengths, the reflection is constructive while for others it is destructive to the pattern.

Zaren [22] investigated an effective moving ground plane by placing a series of frequency selective surfaces (FSS) behind a log-periodic printed antenna. The FSS is transparent at select frequencies and incident angles, but it reflects just like a PEC ground plane at all others. His method was to place FSS layers at the appropriate distances behind the antenna so that

constructive reflections would occur and provide wide bandwidth. His results were inconclusive "due to atypical gain characteristics of the absorber filled cavity design" which he measured. The absorber filled cavity remains the most common way to provide wide antenna bandwidth.

Figure 11 shows a broadband, printed spiral antenna over an absorber loaded cavity. The antenna radiates both above and below the substrate. However, the absorber attenuates the backward traveling energy so that the reflection off the bottom of the cavity is greatly reduced by the time it returns to the antenna. Only the undisturbed, forward propagating energy remains, but it is at a reduced power level. The trade-off is power for bandwidth.

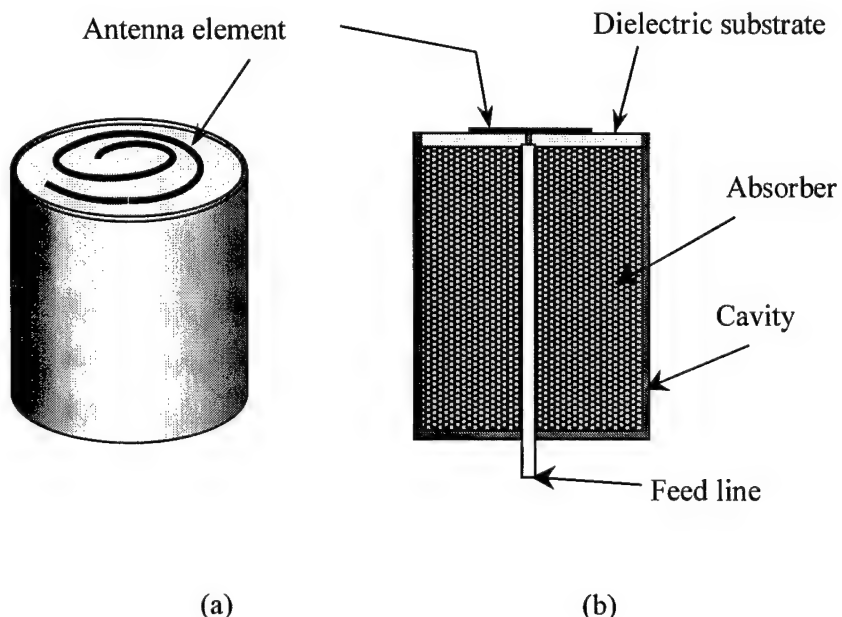


Figure 11. Cavity backed printed antenna. (a) Single spiral element, and (b) cross sectional view of absorber filled cavity.

The thumbtack ground plane is a compromise (with modest bandwidth) between the traditional ground plane of microstrip-based antennas and the absorber backing of cavity-backed antennas. Since the ground plane suppresses surface waves, it is classified as a PC, i.e., the

thumbtack posts create a periodic lattice which prohibit EM wave propagation. However, this does not necessarily provide antenna gain. The combination of the textured surface elements and the thickness of the dielectric substrate create a high-impedance at a single frequency. Since the image currents are in phase, all of the energy reflects in the forward direction. This, combined with the surface wave suppression, has an overall effect of increasing antenna gain and improving radiation patterns.

2.3.1.1. Surface impedance model.

The principal theories for explaining the behavior of the high-impedance ground plane are the surface impedance and effective medium models. Sievenpiper et al.[19] derive the first order design approximations of the high-impedance ground plane by starting with the surface impedance of a metal sheet, i.e.

$$Z_s = \frac{E_z}{H_y} = \frac{1+j}{\sigma\delta}, \quad (5)$$

where E_z and H_y are the field components which are tangential to the surface, σ is the conductivity of the metal in mhos/square, and δ is the skin depth of the metal in meters. By applying a texture to the surface, the impedance is altered and is different for transverse magnetic (TM) and transverse electric (TE) mode. They can be shown to be [19]:

$$Z_s(TM) = \frac{j\alpha}{\omega\epsilon}, \quad (6)$$

and

$$Z_s(TE) = \frac{-j\omega\mu}{\alpha}, \quad (7)$$

where

$$\alpha \approx \frac{\omega}{c} \sqrt{\frac{\omega \epsilon}{2\sigma}} (1 - j), \quad (8)$$

ω is the frequency in rad/sec, ϵ is the permittivity constant of the dielectric substrate, c is the free space speed of light in meters/sec, and σ is the conductivity of the metal layer in mhos/square.

As seen from Equations (6)-(8), the surface impedance changes with frequency and differently for the TM and TE modes. The complex impedance for TM modes is positive and decreases with increasing frequency while the impedance for TE modes is negative and increases with frequency. From textbooks of elementary electromagnetics, this means that the TM modes have an inductive impedance and the TE modes have a capacitive impedance.

Figure 12 shows the parallel circuit model of the two-layer thumbtack design. The small gap between metallic islands provides the capacitance and the thickness of the substrate provides the inductance. For microwave applications the sheet capacitance is typically about 0.05 pF^2 and the sheet inductance is typically about 2 nH^2 , depending on the island geometry [18].

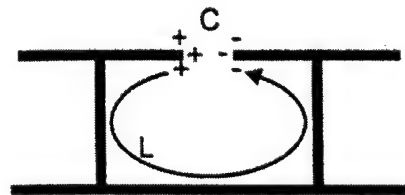


Figure 12. Parallel circuit model of Sievenpiper's patented two layer thumbtack design [18].

A parallel LC circuit has impedance equal to

$$Z = \frac{j\omega L}{1 - \omega^2 LC}, \quad (9)$$

where L is the inductance, C is the capacitance, and ω is the frequency in rad/sec. When the complex part of the impedance equals zero, the circuit is resonant at the frequency

$$\omega_0 = \frac{1}{\sqrt{LC}}. \quad (10)$$

Sievenpiper calculates the inductance as

$$L = \mu_r \mu_0 t, \quad (11)$$

where μ_r is the relative permeability constant for the dielectric material (typically assumed equal to 1.0), μ_0 is the permeability constant, and t is the substrate thickness. He also describes the inter-elemental capacitance as a fringing capacitance, i.e.,

$$C = \frac{w(\varepsilon_1 + \varepsilon_2)}{\pi} \operatorname{Cosh}^{-1} \left(\frac{a}{g} \right), \quad (12)$$

where w is the edge of an element, ϵ_1 is the permittivity of air, ϵ_2 is the permittivity of the substrate, a is the gap between elements, and g is the distance between the outer edges of two adjacent elements.

It is important to note that Equations (9) - (12) are only valid at the single frequency ω_0 and for normally incident plane waves. The assumed permeability constant is not frequency dependent and the gap spacing a and element size (related to g) are not dependent on polarization. A thorough explanation with several examples are given in [19].

2.3.2. Effective medium model and frequency bandwidth.

Sievenpiper explains how the surface impedance model does not accurately predict the bandgap. The conducting vias which create leaky waves, (traveling waves that shed as they traverse the surface), are not accounted for by the surface impedance model. Therefore, he added a parallel damping resistance to make an effective medium model that is dependent on the angle of incidence (and E-field polarization), i.e.,

$$R_{damping} = \eta \cos(\theta), \quad (13)$$

where η is the impedance of free space (377 ohms), and θ is the angle at which the E and H fields are projected onto the surface. $R_{damping}$ allows the leaky waves to satisfy the phase matching condition across the boundary [19]. Although the waves travel slightly, his effective medium model shows a complete bandgap.

Equation (13) is valid only for one frequency; therefore, there exists a region about ω_0 where the phase response of the reflection coefficient is about zero degrees. Sievenpiper calls this the high-impedance region [19] and defines it as the region where the phase response of the

reflection coefficient is between -90 degrees and +90 degrees. None of the other references defined any metrics for establishing the high-impedance region.

The square element and hexagon element HIGPs [18] have approximately 4 and 6 GHz bandwidths, respectively. Although these bandwidths are sufficient for covering Ku- and lower frequency bands, these are still considered narrowband because the in-phase response at -90 or +90 degrees is where the minimum amount of constructive reflection occurs.

2.3.3. Antenna Performance.

The original thumbtack design goal was to suppress surface waves using a PBG lattice [20]. A square patch antenna was designed for 14 GHz and imbedded into the PBG lattice. The center frequency of the PC was also 14 GHz. Figure 13 shows the antenna, feed line, and PBG lattice. Surface waves are excited by the antenna and suppressed by the PC. There is a small buffer of dielectric material left between the PBG lattice and the antenna for improved performance. The results showed a 3.4% increase in bandwidth over the PEC reference antenna and ~1.6 dB more gain.

Additional measurements [19] demonstrated pattern improvements due to the unusual reflection phase. Vertical and horizontal monopole patterns were measured. For the case of the vertical monopole over the finite ground plane, the backlobe was significantly reduced as well as the center null above the antenna. The pattern was also smoother because the surface waves were suppressed and did not scatter off the edge of the ground plane. The horizontal wire antenna, when placed over the HIGP, had a -10 dB return loss, which is only a 10% reflection as compared to a 100% reflection from the reference antenna.

Each antenna demonstration showed significant improvement for a narrowband, planar antenna. Surface waves were suppressed and an in-phase reflection occurred, resulting in higher gain, smoother patterns, and new potential for previously limited designs.

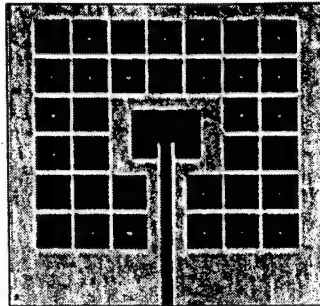


Figure 13. Ku-band patch antenna surrounded by the 2-D PBG lattice [20].

2.4. Conformal antenna research.

The need for conformal antennas stem from the fact that many military aircraft have 60-70 single function antennas and each antenna contributes to the weight and drag of the aircraft [23]. Many of the antennas must compete for the best location on the aircraft, yet they must not interfere with each other's radiation pattern.

Although there are many reasons to flush mount or conform an antenna to the platform's structure, the design is difficult. A planar antenna does not necessarily perform the same when shaped so new designs are often required. Other difficulties with conformal antennas include computational analysis and fabrication versus the payoff of gain, beamwidth, and bandwidth. Although conformal antennas are a benefit to both civilian and military aircraft alike, most of the current literature regarding military research is limited in distribution.

2.5. Chapter Summary

The high-impedance ground plane causes electromagnetic waves to reflect similar to that of a perfect magnetic conductor (PMC, +1 reflection coefficient). A PMC also has in phase image currents and allows electric currents, such as that from a horizontal antenna element, to radiate when placed directly above the ground plane. The resulting antenna patterns have higher gain and are smoother as they are not plagued by edge scattering from surface waves.

In addition, the high-impedance ground plane reportedly suppresses surface waves. For this reason it has been classified as a photonic band structure, or photonic crystal. Photonic crystals do not support propagating electromagnetic modes within a select frequency band, regardless of the direction of incidence and also suppress surface waves.

Computational surface wave coupling models and measured antenna patterns of the planar, thumbtack, high-impedance ground plane have shown improved radiation patterns, but to date there is no reported data for conformal high-impedance ground planes of this type. Conformal antenna research could benefit from this new technology.

3. Methodology

3.1. Method to achieve research goal.

Determination of the performance of the conformed, thumbtack HIGP is best achieved through experimentation for lack of published literature on the subject of conformal, photonic crystal measurement and computation. The ultimate antenna goal is to place a conformal printed antenna directly on a conformal high-impedance ground plane. This is complicated by the fact that periodic structures like the HIGP do not reflect energy equally for all directions.

Figure 14 shows a simple horizontal monopole antenna placed over a high-impedance ground plane. The energy radiates in all directions transverse to the monopole and the phase response for each direction is centered about the phase of the specular reflection (reflection at normal incidence). The HIGP has a positive phase response over a limited frequency band, but if the variance of the resonant frequency changes greatly with the direction of incidence then the resonant frequency of the antenna may not fall in the bandgap, resulting in lower antenna efficiency.

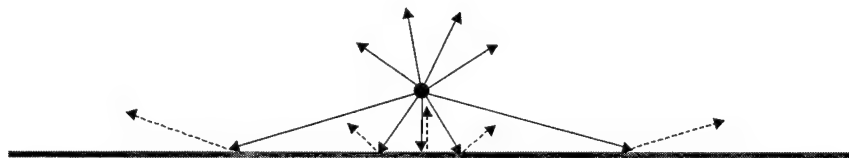


Figure 14. Horizontal monopole radiating over a high-impedance ground plane.

By measuring the variation of the phase response for different angles of incidence, the antenna can be designed to match the mean resonant frequency, thus, providing optimal efficiency. Reflection measurements are the best means of determining the mean resonant frequency because they are easy to compare with known reference plates. Following the set of reflection measurements is a set of surface wave measurements that show how well the HIGP suppresses surface waves. Then the results can be analyzed to determine the necessary size of the high-impedance ground plane when used as an antenna ground plane. The combination of reflection and surface wave analysis helps to decide which type of antenna is best suited for the planar and conformal ground planes.

The first set of experiments is conducted on multiple planar designs and then a second set of experiments is conducted on the same HIGP's after conforming them to a single radius of curvature. The radius is based on those radii used in current conformal antenna shapes. A single radius of curvature is chosen because of the ease at which it can be applied, and to reduce the possibility of confounding errors of doubly curved surfaces.

Without the benefit of published results on measured performance, curvature effects are studied via comparison to a planar structure. When considering the computing power of today, one might ask, "*Why not use computer simulations?*" The answer is that it could be done, however not necessarily within the time frame available. Both frequency and time domain models are based on the solution of simultaneously solved partial differential equations, a difficult task that would still require empirical validation.

In order to meet a compromise between the rigors of developing a new simulation code and sole dependency on accurate measurements, two off-the-shelf codes will be evaluated to determine their suitability to analysis of periodic structures. Measured reflection data of the

reported hexagon HIGP [18] and Schloer's [10] 3-D PC will be used as validation tools. With that, the complete research methodology is listed in Table 1.

Table 1. List of tasks to achieve goal.

<i>Task #</i>	<i>Task description</i>
1	Investigate potential of off-the-shelf, full-wave solvers for use with periodic structures.
2	Design and fabricate thumbtack high-impedance ground planes.
3	Build HIGP and verify the reflected phase response of planar HIGP.
4	Measure the amount of surface wave suppression of planar and curved HIGP.
5	Select/design an antenna appropriate to both planar and curved surfaces
6	Measure the antenna radiation patterns using PEC and high-impedance ground planes.
7	Apply statistical model to results of test matrices and determine effect of curved surface.

3.2. Computational techniques.

The purpose of exploring computational codes was to allow the option of designing a new PBG-based high-impedance ground plane. Two codes that were immediately obtained were the finite-difference time-domain code, *LC*, from SGI and Cray industries, and the government owned periodic moment method code, simply named *PMM*. *LC* is currently a free beta version that has technical support from Cray and a subscriber's e-mail bulletin board. It runs on SGI and Cray UNIX-based machines with single and multiple processors. *PMM* is of course free to government agencies, and runs on a desktop computer. While there is no technical support for *PMM*, there is ample experience within AFIT and the Air Force Research Laboratory when assistance is needed.

3.2.1. Finite-difference time domain software.

LC [25] is a graphical user interface (GUI) based software package that is based on the FDTD Yee algorithm as derived in Taflove [26]. The code supports perfectly matched layers and Mur boundary conditions of first and second order. Also, it has its own computer aided drawing tool kit and accepts various others such as *AutoCad* dxf files and *Iges* design files. For analysis, both plane wave excitation and source excitation are allowed and various probe types and values are supported. Fourier transforms and plots of results are included in the Tools menu.

The test of *LC*'s versatility to model 3-D periodic structures was a model of the reflection measurement system used by Schloer [10]. Schloer measured the reflection coefficient, Γ , of the 3-D diamond lattice photonic crystal by illuminating the test sample with a plane wave source and then calculated Γ as the ratio of the test sample to an equally sized and positioned PEC plate. His measured results were readily available and at the time that *LC* was studied there were not any published results for the thumbtack HIGP. Since *LC* supports plane wave excitation and saves the results in a convenient format, modeling Schloer's experiment seemed the best way to substantiate *LC*'s predictions.

3.2.1.1. Potential benefits of LC.

The fact that it is a time domain code allows one to see the resonant behavior of the periodic structures. Also, the GUI allows quick analysis of the results with minimal reliance on external processing software. If the simulations matched well with measured data, and the computational costs of time and memory were not too burdensome, then *LC* could also be used to design other high-impedance ground planes for conformal applications.

3.2.1.2. Modeling considerations.

Considerations for using FDTD are the mesh size and number of time steps. As the mesh size decreases, more time steps are needed because the time step is automatically determined from the mesh size and *magic time step*, the time step where stability is ensured [26] Also, for a predetermined domain size, the mesh density quadruples if the mesh size is halved. These considerations required a powerful workstation or supercomputer, such as at the Major Shared Resource Center (MSRC). Nonetheless, one goal was to limit computer resources to a parallel processor workstation.

3.2.1.3. Computing resources.

Immediately available was a four processor (195MHz each) Silicon Graphics Origin with 4 Gbytes of RAM. This was convenient since the same machine had other mathematical processing programs that could be used to compute the reflection coefficient. However, there was no way to predict the length of time needed for the simulations *a priori*, because the photonic crystal structures are resonate structures. The only way to determine the time would be to run a simulation; then, verify that the signal decayed sufficiently before applying a Fourier Transform. This was one of the factors in considering LC's usefulness for design work.

3.2.1.4. FDTD test matrix.

Table 2 lists the initial test matrix. The test variables are the same as those of the measurement test matrix in Section 3.4.1.1. Polarization is the orientation of the incident E-field with respect to the incident plane. The azimuth angle is the rotation of the test sample in its own plane. The elevation angle is the angle of incidence of the illuminating source.

Table 2. Test matrix for FDTD simulations.

Polarization	Azimuth Angle (deg)	Elevation Angle (deg)	Polarization	Azimuth Angle (deg)	Elevation Angle (deg)
TM	0	0	TE	0	0
TM	0	35	TE	0	35
TM	0	45	TE	0	45
TM	0	55	TE	0	55
TM	0	65	TE	0	65
TM	45	0	TE	45	0
TM	45	35	TE	45	35
TM	45	45	TE	45	45
TM	45	55	TE	45	55
TM	45	65	TE	45	65

The complex reflection coefficient is then calculated as

$$\Gamma(f) = \frac{\text{fft}(E_{PBG}(t) - E_{inc}(t))}{\text{fft}(E_{inc}(t))}, \quad (14)$$

where $E_{PBG}(t)$ is the reflected time signal from the PBG simulation, $E_{inc}(t)$ is the incident time signal. As can be seen from Equation (14), the test matrix must be run two times to generate the required fields. Fortunately, *LC* uses command line arguments, so a script file can be executed to run the entire matrix in a batch.

3.2.2. Periodic moment method.

Unlike FDTD, PMM [27] is a frequency-domain moment method technique. It is well suited for analysis of infinite periodic arrays. However, it is currently limited to planar two-dimensional thin wire or thin slot arrays (the aspect ratio, the ratio of slot length to slot width, should be kept greater than 10:1). The dimensions of the 3-D crystal do not satisfy the aspect ratio, so it is uncertain if PMM can predict reasonable results. Additionally, only normal incidence can be considered because it is only at normal incidence that the metal vias are completely shielded by the planar elements. Fortunately, a small amount of HIGP results were

published at the time PMM simulations were beginning. Although the currents exist in the narrow gaps, which can excite currents on the metal posts, PMM still has the potential to coarsely predict the reflection coefficient of the HIGP at normal incidence because the metal posts are not directly excited by the incident E-field.

3.2.2.1. Benefits of PMM.

One benefit PMM has over FDTD is that *PMM* calculates the reflection coefficient so no post-processing is needed. Second, it runs on a desktop computer, and typically, much faster than FDTD for simple structures. If reasonable results could be achieved for normal incidence, then PMM could serve as a course design tool for other high-impedance ground plane designs.

3.2.2.2. Modeling considerations.

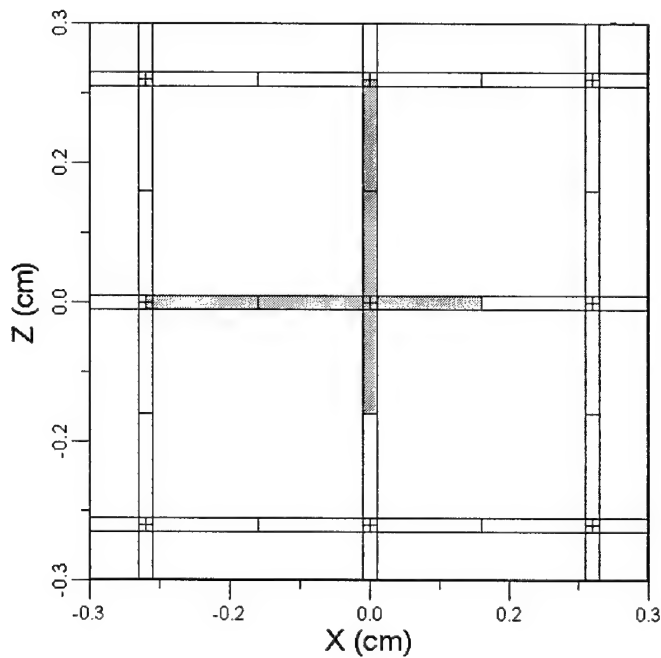
Other considerations for the PMM model are the selection of current modes, and the number of segments in a slot. For initial runs, the minimum number of segments, two, will be used along with the default convergence tolerance. One important point to remember is that PMM is for infinite arrays. Therefore, the computed results must be kept in perspective of the measured results for a finite structure.

3.2.2.3. PMM test matrix

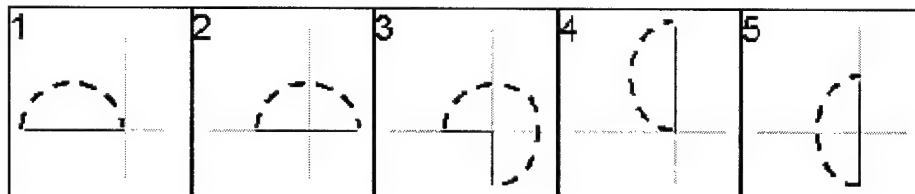
Table 3 shows the basic test matrix for the PMM computations. This test matrix is for the HIGP [19]. Only reflection data at normal incidence was published, but the test matrix follows the proposed measurement matrix in Section 3.4.1. The two samples are hexagon and square elements. The elevation angle is the direction of the illuminating source, and polarization is again, the orientation of the E-field. Figure 15 and Figure 16 show the square and hexagon reference elements and their associated current modes, respectively.

Table 3. Test matrix for PMM analysis.

Polarization	Sample	Angle (deg)	Polarization	Sample	Angle (deg)
TM	Hex	0	TE	Hex	0
TM	Hex	35	TE	Hex	35
TM	Hex	60	TE	Hex	60
TM	Hex	70	TE	Hex	70
TM	Square	0	TE	Square	0
TM	Square	35	TE	Square	35
TM	Square	60	TE	Square	60
TM	Square	70	TE	Square	70



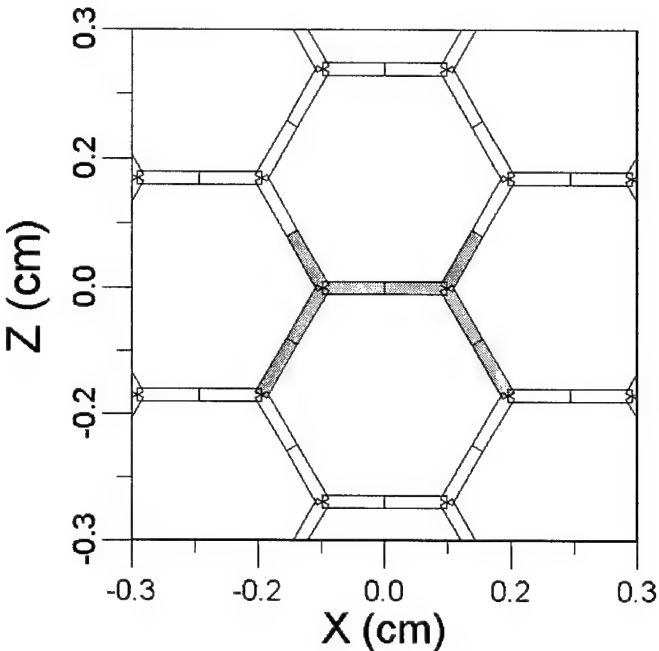
(a)



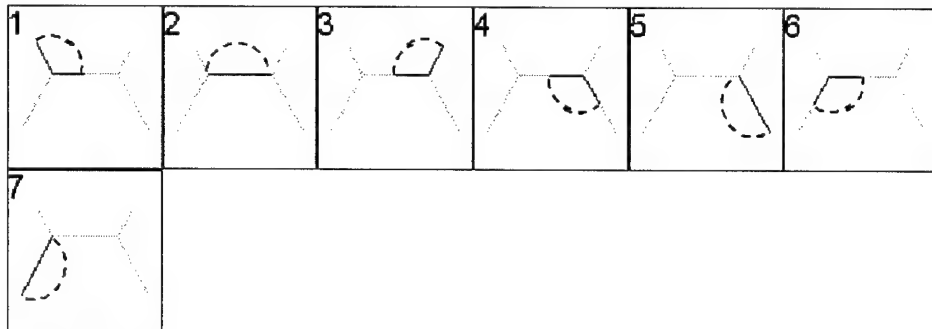
(b)

Figure 15. Square pattern HIGP modeled as thin slots in PMM. (a) Pattern with reference element highlighted, and (b) piece-wise sinusoid current modes on reference element. Piecewise sinusoidal current modes overlap to simulate the infinite slot length.

The two size parameters are the lattice constant and the gap size. The gap was set for 0.15 mm for both the square and hexagon sizes and lattice constants were set to 2.44 mm and 2.54 mm, respectively.



(a)



(b)

Figure 16. Hexagon pattern HIGP modeled as thin slots in PMM. (a) Pattern with reference element highlighted, and (b) piece-wise sinusoid current modes on reference element.

3.3. Design and fabrication of thumbtack HIGP

3.3.1. Choice of patterns.

Since the goal is to determine the effect of adding curvature to a planar HIGP, the best starting point was to use the published, planar square and hexagon designs. They had been reported for various thickness, shapes, and dielectric substrates so it was easy to select two designs of near equal dimensions. The spacing of the gaps was equal for the two layouts and the lattice constants were only different by 0.1 mm. It was important to have each pattern with similar if not equal dimensions so that a comparison of the two patterns could be analyzed.

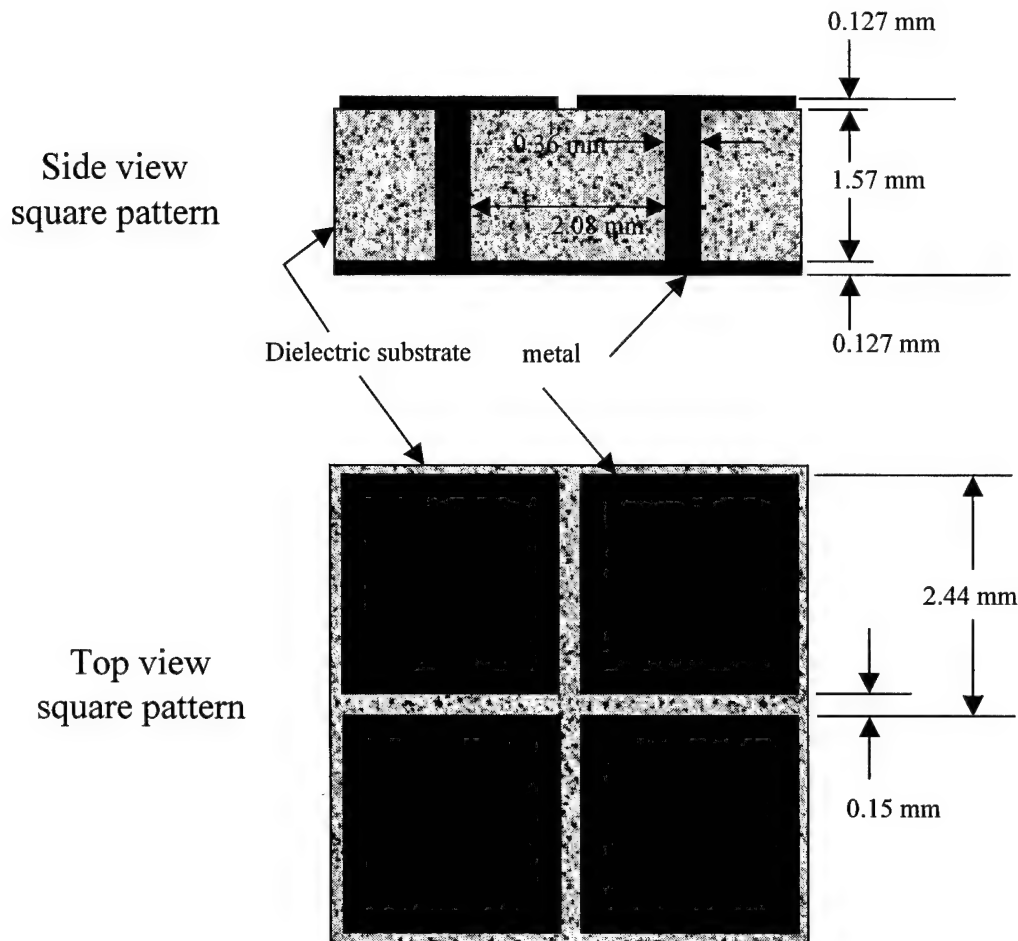
3.3.2. Materials.

The material used by Sievenpiper et. al [18] was duroid 5880 and 6010. These are teflon based fiberglass laminates that have dielectric constants of 2.21 and 10.2 respectively. It so happened that some duroid 5880 from Taconic was available and technical reports from the Rogers Corporation, another manufacturer of microwave materials, stated that, of the duroids, 5880 performed the best during bending tests. This was ideal since Sievenpiper's designs used the same material.

3.3.3. Layout.

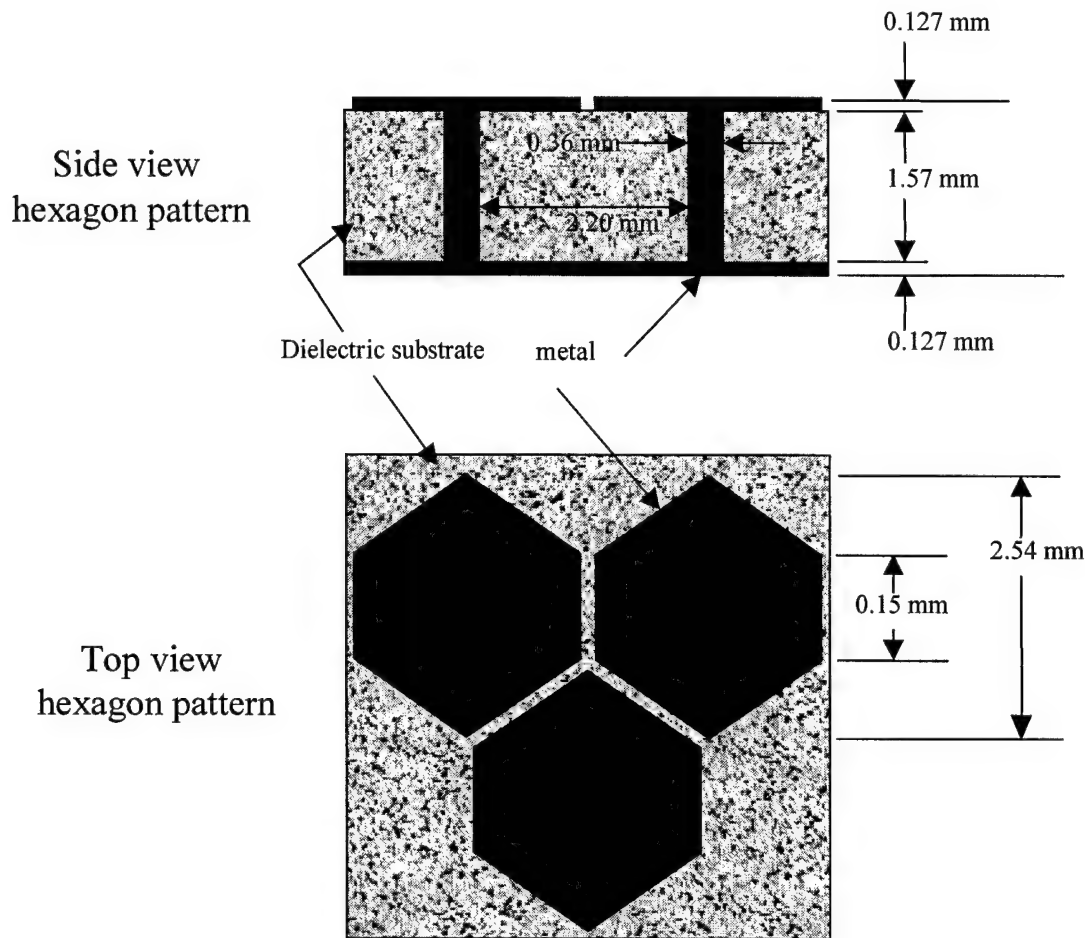
By selecting the same material, there was no need to scale the dimensions of the HIGP. Granted, the Taconic 5880 has a slightly different (0.31 difference from Rogers Corp.) dielectric constant than Rogers Corp. 5880, the small difference is not considered significant to the design layout.

Figure 17 shows the dimensions of the final designs.



Scale: 0.5 inch = 1 mm

(a)



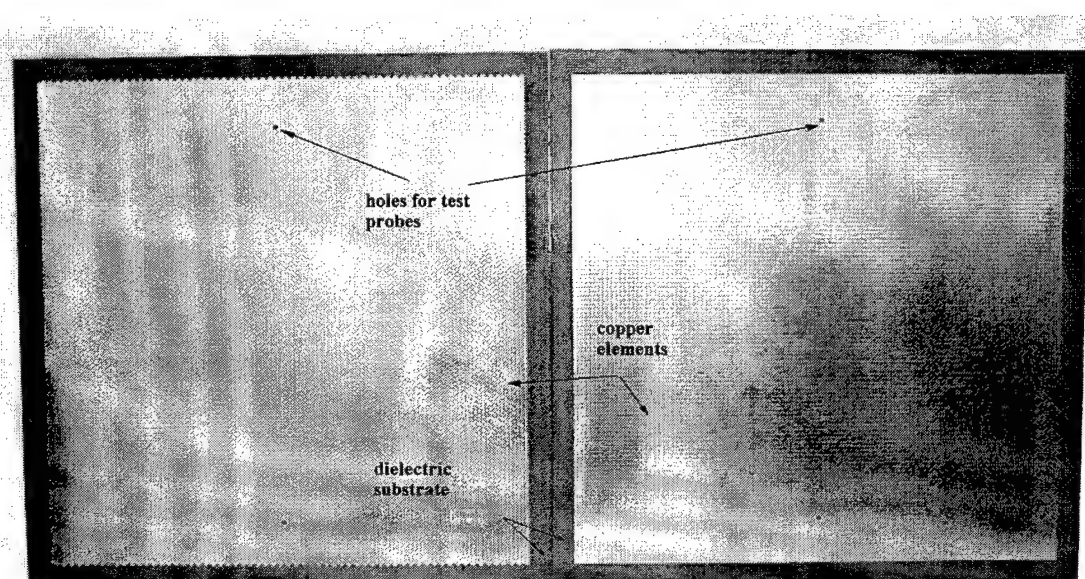
Scale: 0.5 inch = 1 mm

(b)

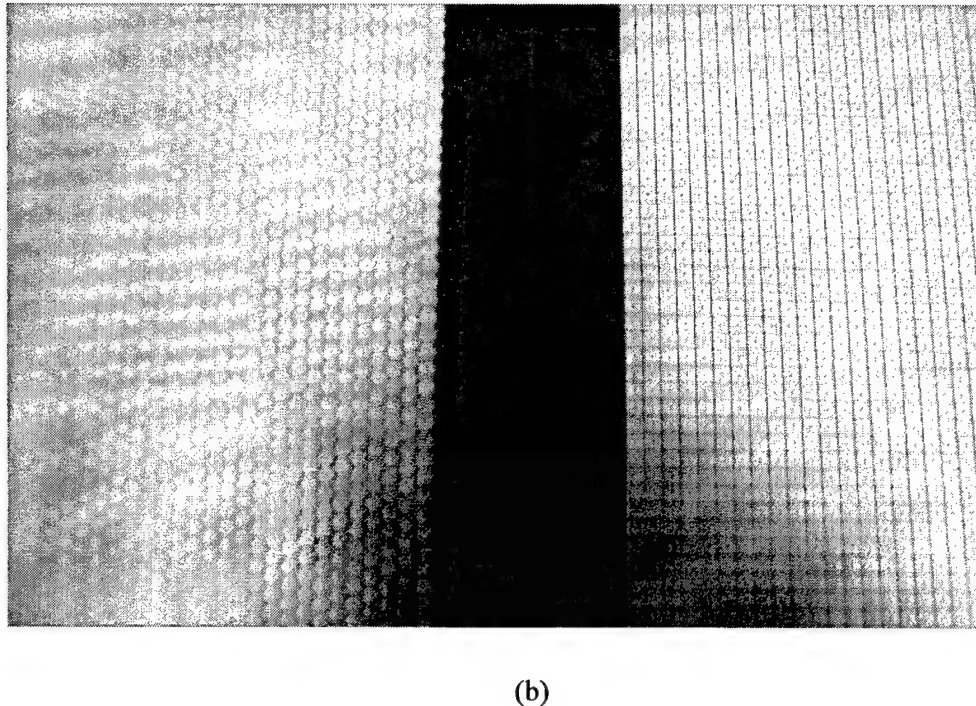
Figure 17. Layouts for fabrication. Dielectric is duroid 5880 ($\epsilon_r=2.51$). (a) Square pattern, and (b) hexagon pattern.

3.3.4. Fabrication.

Circuit Center Inc. of Kettering, Ohio, was chartered to make the HIGP. The patterns filled an 11-inch by 11-inch square, centered on the 12-inch by 12-inch boards. The only change from the original design was to eliminate the last step of tinning the copper pattern. The intention of the tinning was to prevent oxidation, but the small separation of the pattern elements caused unusual amounts of solder wicking, or solder bridges, across adjacent elements. Thus, the copper elements were left bare. The final boards are shown in Figure 18. Small holes for a rigid coax test probe are shown.



(a)



(b)

Figure 18. Planar high-impedance ground plane after production. (a) Test samples side by side, and (b) close up of element patterns.

3.4. Reflection of high-impedance ground planes.

Since the high-impedance ground plane is defined by the phase response of its reflection coefficient, the best way to determine if a test sample is in fact a high-impedance ground plane is to measure the reflection coefficient. Several techniques have been used to measure the reflection coefficient, Γ , of photonic crystals with varying degree of error analysis and reduction.

Measurement of Γ for the planar HIGP is critical for establishing a baseline for the conformal HIGP. The reason is that it is difficult to set up a consistent phase reference for curved surfaces, so only reflection of the planar surfaces will be conducted.

Resources at AFIT and AFRL allow comparison of three different reported methods. They include sophisticated focused beam systems, far field reflection, and simple waveguide probes techniques. Each method is used to identify the band gap (-45 degree to +45 degree phase response) and then compared to determine the benefit of the different methods. Sievenpiper's -90 degree to +90 degree metric is not used here to ensure that the high-impedance region always has in-phase image currents. This is essential for using the HIGP as an antenna ground plane, as discussed in Section 2.1.

3.4.1. Reflection measurements.

The three measurement systems are the Georgia Tech Research Institute focused beam system, a generic far field system, and a waveguide probe system.

3.4.1.1. Georgia Tech Research Institute (GTRI) focused beam.

Figure 19 shows the major system components, two RF lenses and two linearly polarized horn antennas that are all mounted on a pivotal base. The system is controlled via an HP8510 Network Analyzer and desktop computer (not seen). A plane wave is generated by illuminating one lens that serves to focus the beam to approximately a plane wave at the focal point of the lens. Reflected or transmitted power is then measured at the same lens (monostatic reflection), or the second lens (bistatic reflection and transmission), by the network analyzer.

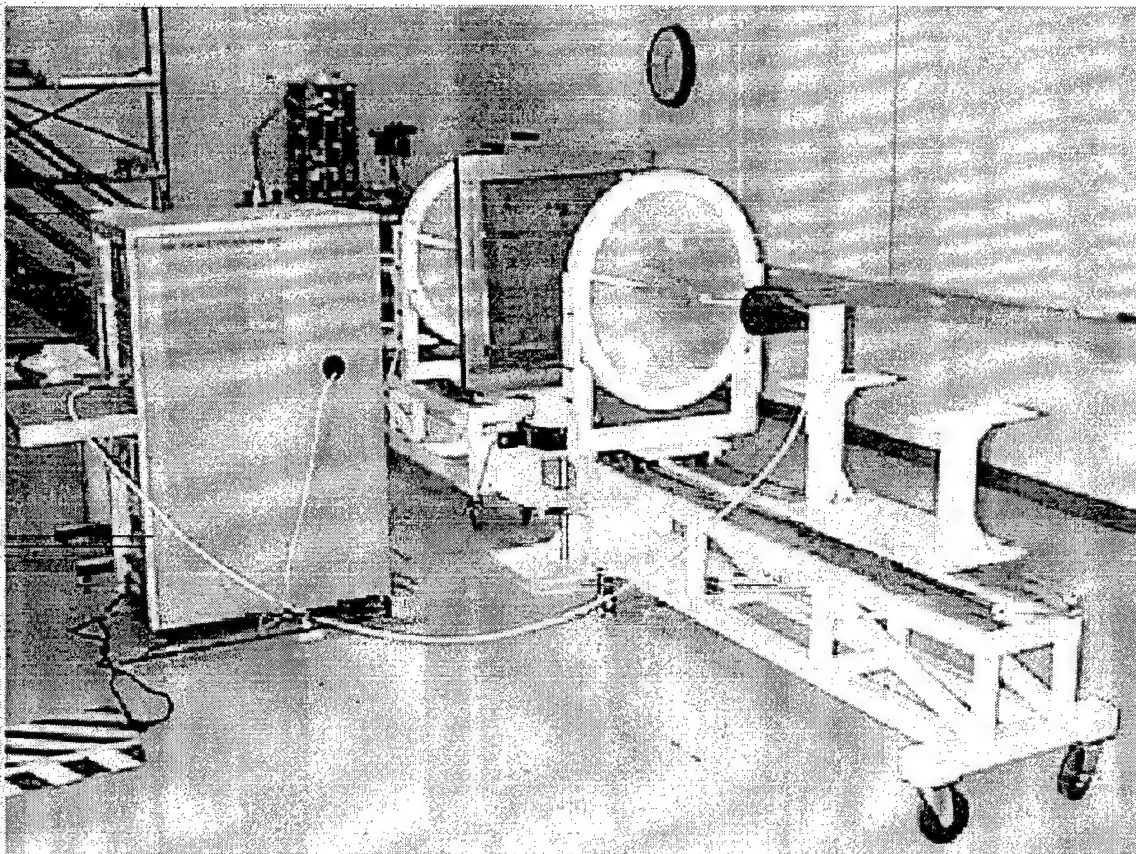


Figure 19. GTRI Focused beam system connected to HP8510 Network Analyzer. As shown, configured for normal incidence reflection and/or transmission. Courtesy of the Signatures Technology Branch, Air Force Research Laboratory.

The system can measure frequencies from 2-18 GHz (expandable to >100GHz) in 20 MHz increments for normal incidence and 35 to 70 degrees off normal for bistatic measurements.

Figure 20 shows various sources of errors for the system. Most of the scattering and multipath errors can be reduced by use of the network analyzer's software gate, because the sample is displaced far enough from the lenses. The horn, boom, and pedestal misalignment may be reduced with careful movement and measurement of the off normal angles. While not a trivial task, the focusing errors can be reduced by reflection and transmission measurements of known samples. The center pedestal is bolted to the floor and leveled, so flat samples are at a precise 90-

degree angle to the floor. The beam size helps reduce errors due to finite sample size provided the sample is large enough. At the focal plane, the beam is 12 inches in diameter at 2 GHz and 4 inches in diameter at 18 GHz. Since the sample sizes are 12 inches square and only Ku-band (12-18 GHz) is of interest, the beam size should not be a significant error.

Besides careful alignment of the hardware, and software gating, the ratio calibration method divides out errors such as phase and amplitude taper and edge scattering due to finite sample size. The procedure is to use a PEC calibration plate of the same size as the sample to normalize the test sample reflection and transmission measurement.

Overall, the focused beam system is well known to be a sturdy, reliable, and very accurate measurement system.

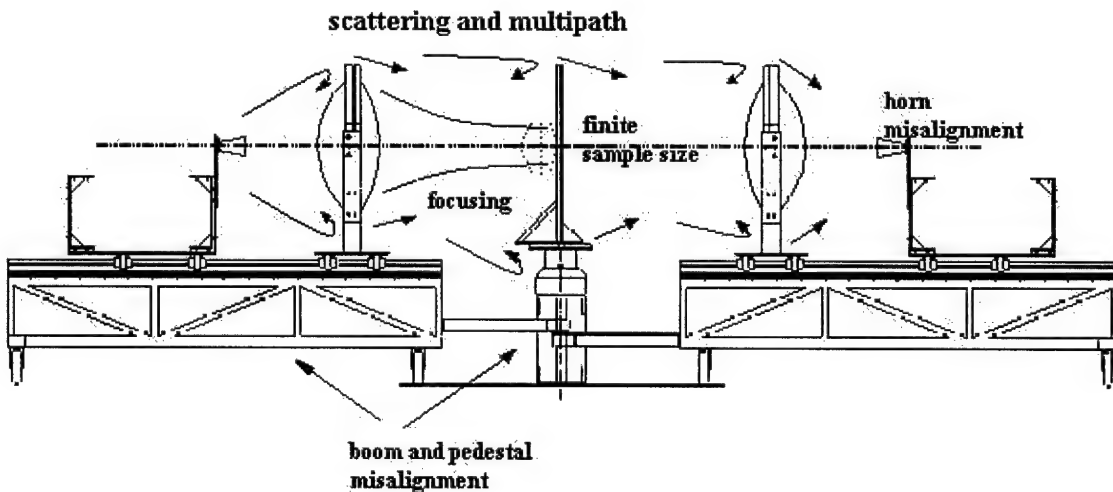


Figure 20. Sources of errors for the GTRI Focused beam system. Courtesy of the Signatures Technology Branch, Air Force Research Laboratory, Wright-Patterson Air Force Base, Ohio.

The test matrix for the experiment is given in Table 4 of Section 3.2.1.4. The polarization is determined by the E-field orientation. When the antenna horns are set for vertical polarization, i.e. the E-field is vertical with respect to the floor, the plane wave is transverse-electric (TE) polarized. When the system horns are set for horizontal polarization, the plane wave is transverse-magnetic (TM) polarized. The angle is with respect to the HIGP surface normal.

Table 4. Test procedure for GTRI reflection measurements.

Step	Task
1.	Set boom for desired angle.
2.	Place PEC calibration plate in test stand.
3.	Measure, apply 2nsec software gate, and store in memory of HP8510C.
4.	Replace PEC calibration plate with test sample.
5.	Measure; apply 2nsec software gate at same time reference as step 3.
6.	On HP8510C, display math(/) to calculate ratio.
7.	Save formatted (magnitude or phase only) or raw (complex vector) data.
8.	Repeat steps 1-7 for each configuration.

The particular system at the Sensors Technology Branch of the Air Force Research Laboratory is mostly automated, but the software gate can effect the results so it should be checked before running the complete test matrix. Normally, the test matrix would be randomized for statistical evaluation; however, due mainly to the repeatability of the system, and time limitations in the test facility, completion of the test matrix is sequential.

3.4.1.2. Far field reflection measurement.

The most common type of reflection measurement is the far field measurement technique. It is very similar to a Navy Research Laboratory Arch system. Essentially two horn antennas, slightly separated, are placed directly above the sample. The bistatic reflection is measured off a PEC reference plate and the test sample. The reflection coefficient is calculated from the ratio of the test sample measurement to the reference measurement.

Figure 21 shows one set-up of the system. The horns are approximately 25 cm above the sample, which places the horns nearly 20 wavelengths at 12 GHz, away from the sample. This distance is enough to satisfy the far field condition for approximating a plane wave. Absorber surrounds the plate to reduce reflection from the floor. Variations of this setup often place the sample on a wall of an anechoic chamber lined with absorbing material. Also, absorber is placed between the horns to reduce spill over and mutual coupling. A software gate can be applied but reflections from the floor are too close to the sample in order to isolate the sample's reflection.

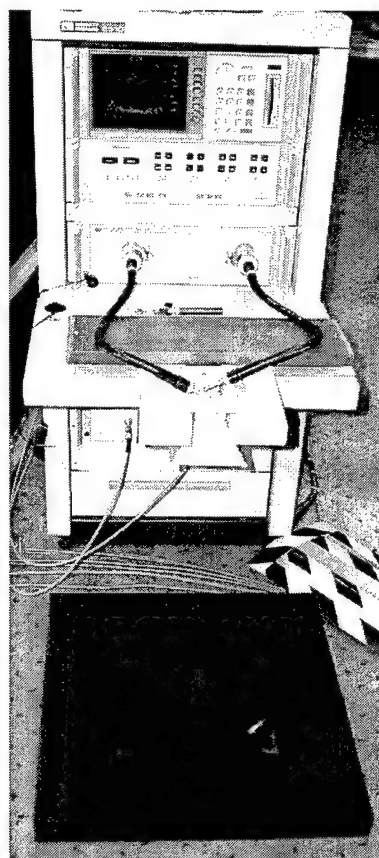


Figure 21. Far field reflection measurement set-up. Shown are the HP8510C Network Analyzer, two standard gain horns, and a copper reference sheet.

Although this set-up has more external influences than the focused beam system, it is very inexpensive compared to the focused beam set-up. The goal of these experiments is to simply determine if the set-up can provide reasonable results compared to the focused beam.

Unlike a true NRL arch that can measure bistatic angles, this set-up can only measure normal incidence, at which the polarization is ambiguous. The test matrix for this system is shown in Table 5.

Table 5. Test matrix for far field reflection measurement.

Sample	Absorber walls
Hex	Yes
Hex	No
Square	Yes
Square	No

A check of the effect of adding absorber walls is included to determine if multipath effects can be reduced. The samples are the same planar HIGP designs as the GTRI measurements and the operation of the HP8510C is manually operated as described in the test procedure for the GTRI system.

3.4.1.3. Waveguide Probe.

The waveguide probe measurement is the simplest of the three, provided the appropriate waveguide (Ku-band for this test) and calibration kit is available. An HP8510 Network analyzer is used to measure the 1-port reflection, S_{11} , of the test sample. Figure 22 shows the test set-up with the network analyzer. Shown are the calibration short, offset (open), and standard broadband load.

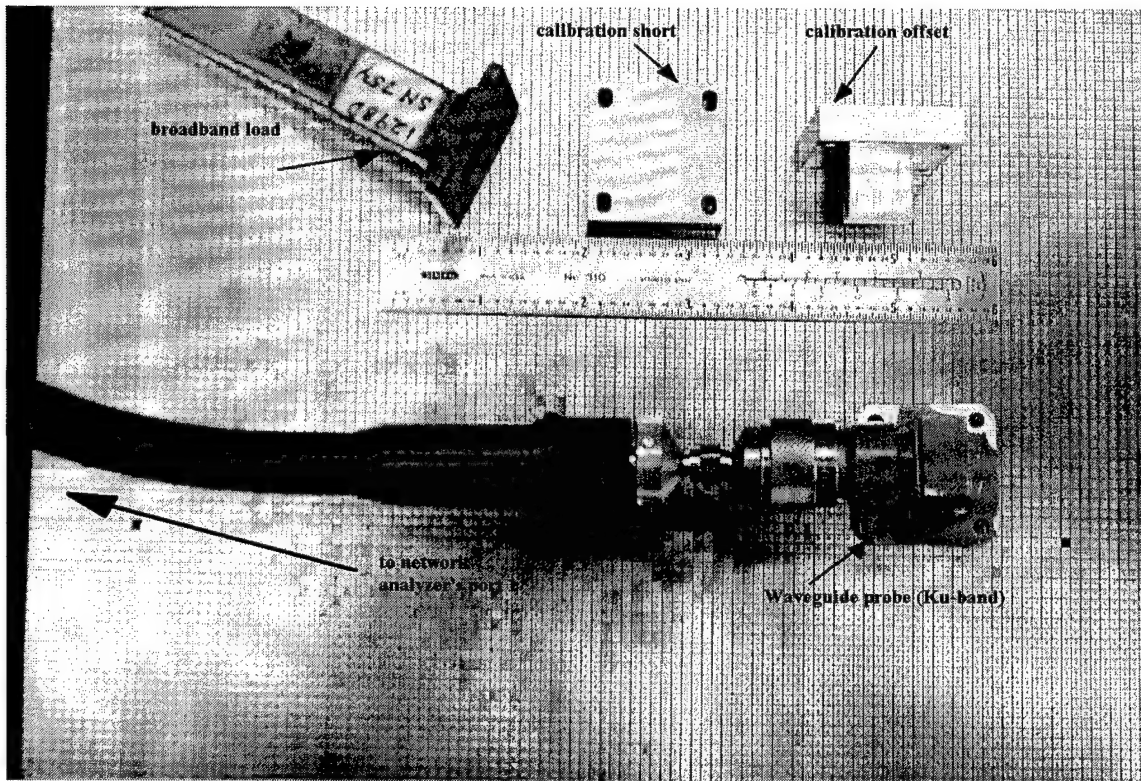


Figure 22. Waveguide probe technique shown with square element HIGP. Also shown are the calibration short, offset, and load with the Ku-band waveguide probe.

No calibration plate is required because a reference short is used with the calibration kit. Unlike the GTRI focused beam and the far field set-up, only a small test sample is needed to cover the waveguide opening. The trade-off is the fact that plane waves do not exit in a waveguide. Therefore, reflection at normal incidence can not be measured, and an equivalent angle of incidence must be calculated based on each waveguide mode, i.e. frequency.

The reason to do this measurement is to determine how far the phase response differs across the large test sample. Ideally, there should not be any measurement differences between different probe positions, but slight manufacturing tolerances may be noticeable with a statistical evaluation.

Two different experiments are conducted. The first is a test of the phase response repeatability across the board. The hexagon HIGP was sectioned into 64 areas; each was just large enough to cover the waveguide. A random order was predetermined and each tested. Then, using the resonant frequency as the yield value, an analysis of variance test was computed. A random test with a metal plate showed that the technique was very repeatable in spite of the probe being handheld.

The second test was simply to compare the hexagon and square patterns. Each was measured twenty times at random locations on the respective test boards. Again, an ANOVA test was conducted to determine the significance of the pattern element.

3.5. Measuring surface wave suppression.

Measurement of surface waves is sometimes difficult because surface waves typically have small magnitudes and often, their existence is only verifiable by their effects. For example, measured antenna patterns are usually rippled when the antenna is placed over a finite ground plane. Surface waves scatter off the edges of the ground plane and interfere with the pattern. For years, radar cross-section measurements have been plagued by surface wave phenomenon. Canonical targets such as spheres and cylinders are smooth and readily support excitation of surface currents by the incident planewave. To reduce the effects, radar-absorbing materials are placed on the backside of a target. For very large targets, hardware gating can be a sufficient means to isolate the main backscattered signal from the interfering surface wave.

However, with careful attention to the associated errors, it is possible to use small probes to measure surface wave coupling. Sievenpiper et al [18] used such an approach to demonstrate the capability of the hexagon thumbtack HIGP to reduce surface wave coupling. They used three types of probes, vertical wire, horizontal wire, and wire loops. They placed a test sample on a

sheet of absorber and placed two probes (normal to test surface) that excited TM mode currents on the surface. Then the S_{21} measurement of a network analyzer was used to measure the coupling. This is the starting point for the surface wave measurement used in this study.

3.5.1. Surface wave coupling on the planar HIGP.

After considering the type of errors that can influence the system, an experiment very similar to that reported was used to verify the surface wave suppression of the HIGP designs. Figure 23 (a) shows the test configuration and the associated influences on the system.

The main source of errors is the test fixture. Figure 23 (b) highlights the dominant contributions. Direct illumination can mask the surface wave and edge diffraction, albeit small in magnitude. It can also alias weakly coupled traveling waves. To overcome these types of errors, a 2-port thru calibration is performed with a metal plate prior to the measurement. The metal plate is placed in the test fixture and the probes extend from the top of the plate. Figure 23 (c) displays the cross-sectional view of the test fixture. The thin HIGP is taped to the metal plate with heavy duty, double-sided tape and the holes for the test probes are aligned in each board. Using this technique, the plate and HIGP are simply turned over for the respective calibration, thus ensuring the same set-up each time. The absorber block was cut with a 10-in x 10-in window and a counter sunken shelf at the thickness of the affixed plate and HIGP. This way the top of the surface is flush with the absorber. Flush mounting the board is intended to attenuate edge scattering and provide a means of ensuring a consistent measurement technique.

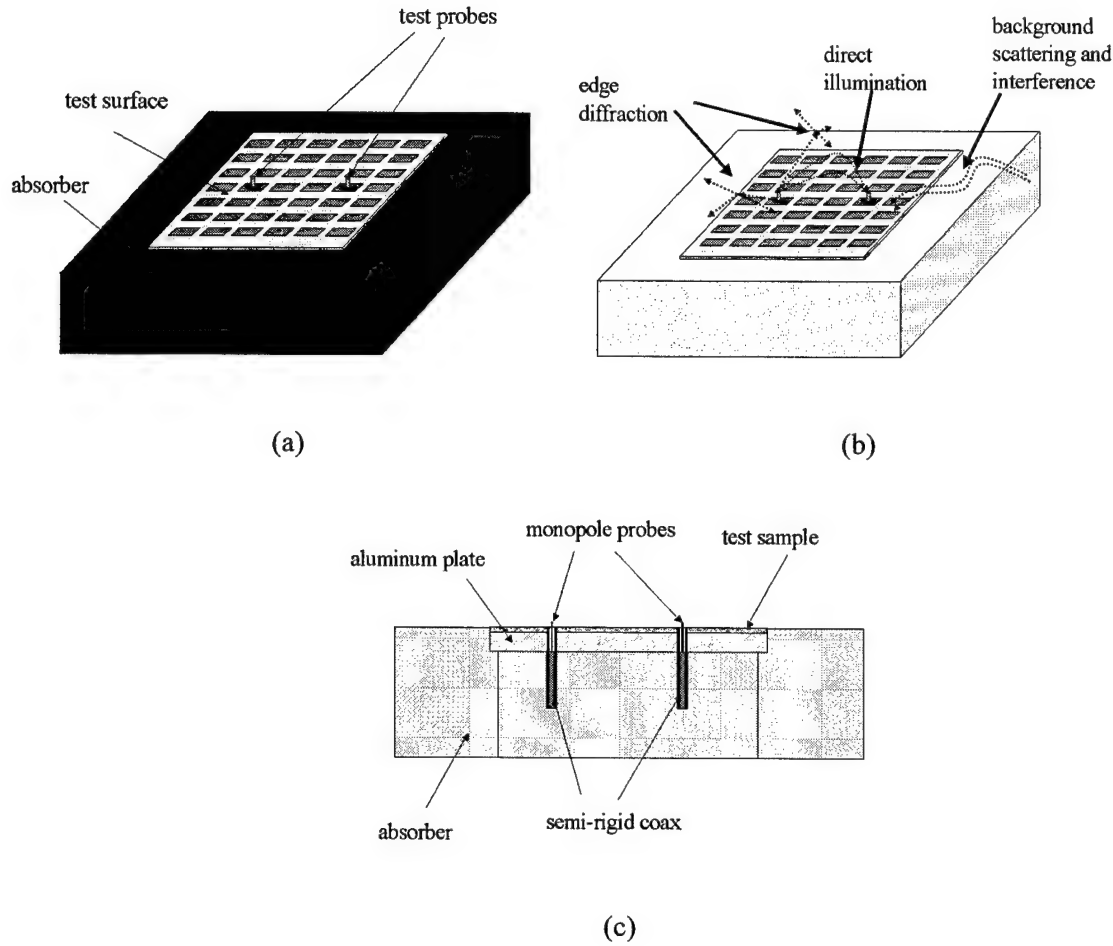


Figure 23. Surface wave experiment configuration. (a) Test fixture, (b) sources of errors, and (c) cross-sectional view of test fixture.

The test matrix is given in Table 6 and the test procedure is given in Table 7. Although TE modes will not produce currents on the PEC reference plate, they will induce currents on the HIGP for the frequencies in the bandgap. As a comparison for TE modes, a PEC backed duroid sheet is included in the test matrix.

Table 6. Test matrix for surface wave measurements.

Polarization	Sample	Polarization	Sample
TM	Hex	TE	Hex
TM	Square	TE	Square
TM	Duroid 5880	TE	Duroid 5880
TM	PEC	TE	PEC

Table 7. Test procedure for planar surface wave measurement.

Step	Task
1.	Place the test sample, reference side up in the test fixture.
2.	Perform response isolation thru calibration.
3.	Turn over the test sample so that the HIGP surface is face up.
4.	Replace PEC calibration plate with test sample.
5.	Measure S_{21} coupling between probes.
7.	Save formatted (magnitude or phase only) or raw data (complex vector).
8.	Repeat steps 1-7 for each configuration of the test matrix in Table 6.

3.5.2. Surface wave coupling of singly curved HIGP.

Similar to the planar measurements, edge diffraction occurs at the edge of the test sample, which is placed in the window. However, scattering at the edge of the test fixture is eliminated in one dimension and reduced in the other because one dimension is nicely curved and guides surface waves into the absorber lined floor. Waves traveling transverse to the curvature scatter further from the receive probe and do not interfere with the measurement. An additional benefit is that the radius of curvature prevents direct illumination of the receive probe.

Figure 24 shows the layout of the *Doghouse* test fixture for the conformal HIGP experiments. A radius of 20-inches was chosen because that has been used for demonstrated conformal antenna arrays and the goal is to determine the ground plane's performance when conformed to a practical radius. The skin of the doghouse is 3003 aluminum at 63 mils thickness. The supporting ribs are made of $\frac{3}{4}$ inch birch plywood. The horseshoe shape allows the test sample to be mounted vertically to a positioner for antenna measurements.

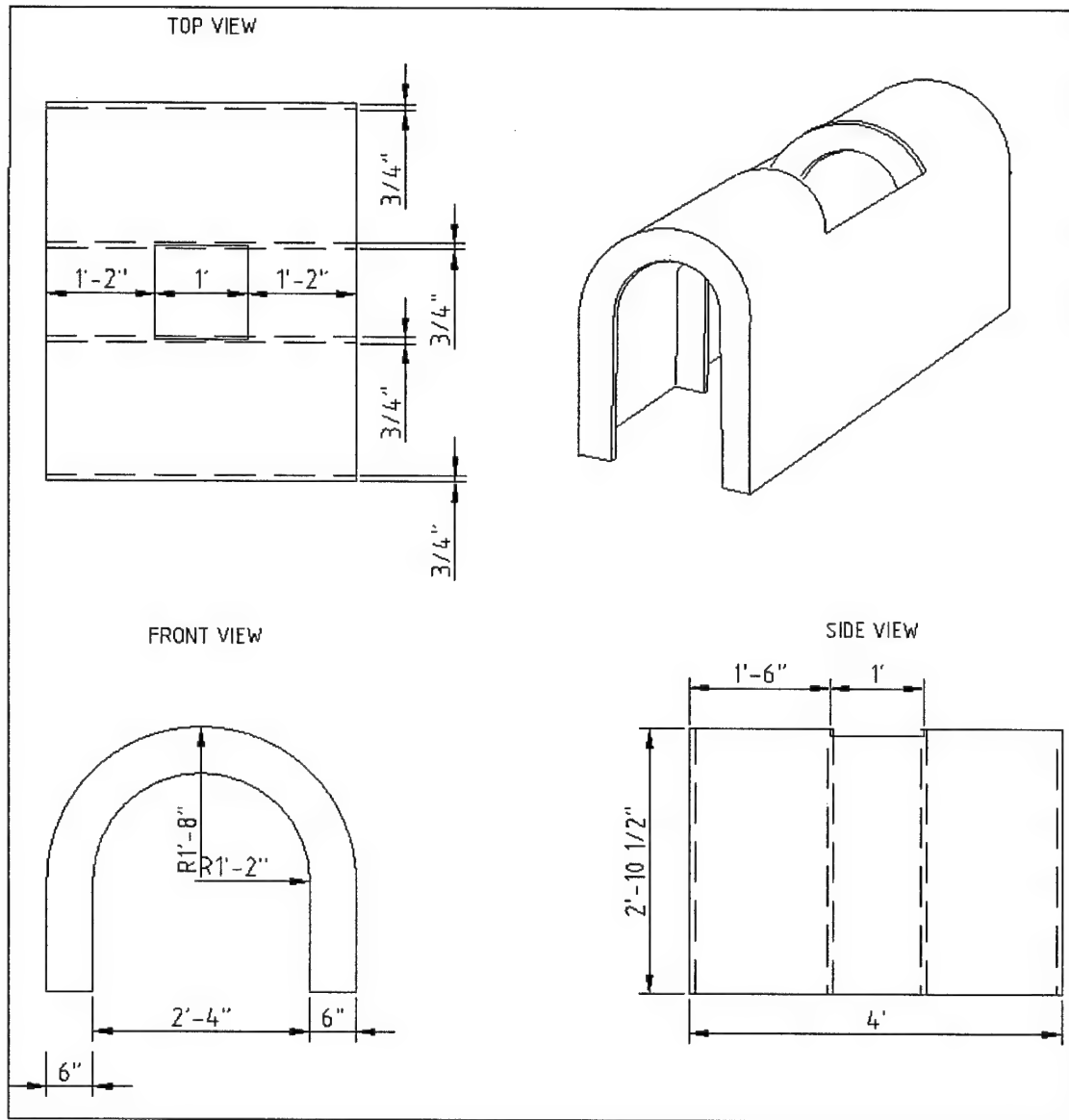


Figure 24. Test body for conformal ground plane surface wave measurement. Can also be used for antenna measurements. Shown is the original drawing of the Top, Front, and Side view.

The procedure for the conformal surface wave measurement is nearly the same as the planar technique discussed in Section 3.5.1. The difference is that the metal reference plate is not affixed to the test sample due to the curved shape.

3.6. Antenna pattern measurements.

With the characteristic surface wave suppression and phase response of the high-impedance ground plane established, the remaining tests were the antenna measurements. This single application of the HIGP has the potential to demonstrate the effects shown by all the other measurements, but not necessarily which cause produces the resulting effect. Standard antenna measurement procedures [1] were used and performed in the Radiation and Scattering Compact Antenna Laboratory (RASCAL) of the Applied Aperture and Receiver Technology Branch, Sensors Directorate, AFRL.

3.6.1.1. Antenna selection and design.

A log-periodic dipole (LPD) antenna was chosen because it has broad frequency band, linearly polarization, capability for endfire or broadside radiation, and a well documented design. Zaren's [22] printed antenna design was scaled for use on a thinner substrate, which made bending the antenna easier. One consideration was the type of feed. With a coaxial feed, a hole had to be drilled through the substrate, i.e. the HIGP. The feed hole perturbs the periodic structure near the resonant teeth and causes unpredictable changes to the radiation pattern. Figure 25 shows the antenna with the original (center) and alternate (outer) feed holes. Instead of feeding the LPD antenna at the center, it was fed at the end. Table 8 lists the antenna dimensions.

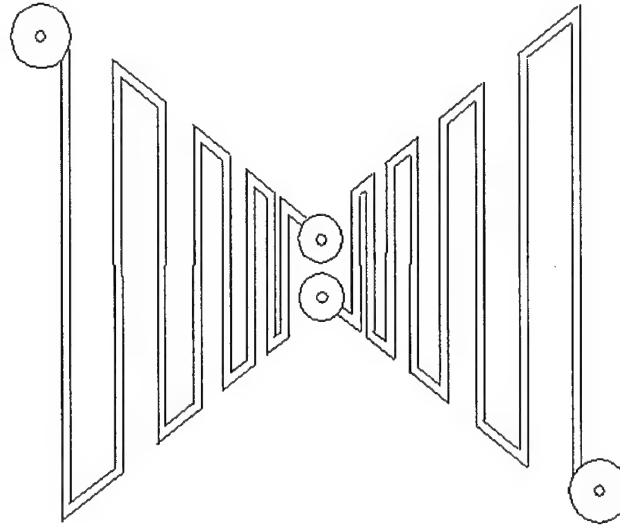


Figure 25. Log-periodic dipole antenna layout. Small inner circles are holes for coaxial feed, larger circles are copper pad for solder connection.

Table 8. Log-periodic antenna design lengths.

f_r of dipole (GHz)	Dipole length, $\lambda_g/2$ (cm)	Distance from center (cm)
19.6	0.5785	0.18
16.2	0.7	0.25
13.33	0.8505	0.35
10.93	1.033	0.4715
9.03	1.2556	0.6191
7.43	1.5255	0.7985
6.12	1.8534	1.0164
5.04	2.252	1.2812

3.6.1.2. Measurement facility.

RASCAL is a mini-compact range with dimensions of 24' x 12' x 9'. Antenna patterns and radar-cross section are measured by an HP8510C Network Analyzer from 2-18 GHz. Figure 26 shows the top view of the range layout. The planar antenna is mounted in a foam block on the

foam column and the curved antenna is mounted in the doghouse, which is then mounted on the positioner via a supporting structure.

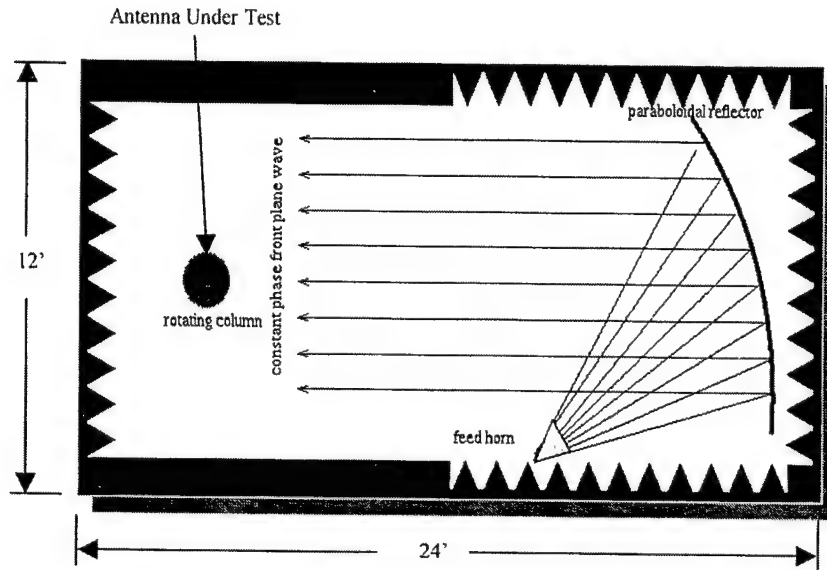


Figure 26. The Radiation and Scattering Compact Antenna Laboratory (RASCAL), Applied Aperture and Receiver Technology Branch, Air Force Research Laboratory, Wright-Patterson Air Force Base, Ohio.

3.6.1.3. Test matrix and procedure.

The planar antenna is measured first to establish its performance both with and without the high-impedance ground plane. Then the curved antenna is measured in the conformal ground plane configuration. The procedure is to simply measure a standard gain horn, followed by the test antenna. Then the test antenna gain is computed by multiplying the standard gain antenna gain times the ratio of the measured test antenna to the standard gain antenna, i.e.

$$G_{AUT} = \frac{G_{REF} P_{AUT}}{P_{REF}}, \quad (15)$$

The test matrix is given in Table 9. Each antenna pattern is measured from -90 to +90 degrees off broadside from 12 - 18 GHz in 1 degree and 0.5 GHz increments, respectively. Both TM and TE polarization are measured for each ground plane/antenna configuration.

Table 9. Test matrix for antenna measurements.

<i>Ground Plane</i>	<i>Curvature</i>	<i>Ground Plane</i>	<i>Curvature</i>
None	None	None	20"
Absorber	None	Absorber	20"
PEC	None	PEC	20"
Square	None	Square	20"
Hex	None	Hex	20"

4. Results and Analysis

4.1. Computational Analysis.

The goal of the computational analysis is twofold. First, a thorough investigation of the design parameters and limitations of the high-impedance ground plane can be conducted with only a cost of time and computing resources. Second, the phase response of the reflection coefficient can be studied under different test conditions without the restrictions of test equipment limitations. Measurements in Section 4.2.1 will be used to validate the accuracy of the computational method.

Ultimately an antenna will be placed directly on the high-impedance ground plane, but before this is done, it is critical to know how the phase response behaves under different test configurations.

4.1.1. Finite difference time domain.

The FDTD model did not predict the measured band gap of Schloer's [10] photonic crystal. To explain why the model did not produce the desired effects, the major model parameters are reviewed. This is not intended to be all inclusive of FDTD modeling techniques, but rather as a guide to isolate the specific modeling errors and *LC* limitations that resulted in the inaccurate model.

The first check is of the computational mesh that FDTD uses to calculate the E and H fields. The rule of thumb for FDTD is to sample at least 20 wavelengths per unit cell [26]. This means that for a cubic mesh, a 0.35 mm spacing is needed to properly model a geometry for a

frequency of 2 GHz. The mesh size used was 0.25 mm which samples 28 wavelengths at 2 GHz (the longest wavelength in the frequency range of interest).

Second is the consideration of the computational boundary. The boundary, shown in Figure 27, should fall on the mesh, and if it does not, then *LC* interpolates the values of the E and H fields. When the E and H fields are interpolated at the absorbing wall boundary modeling error is introduced in the form of smeared field values near the absorbing wall.

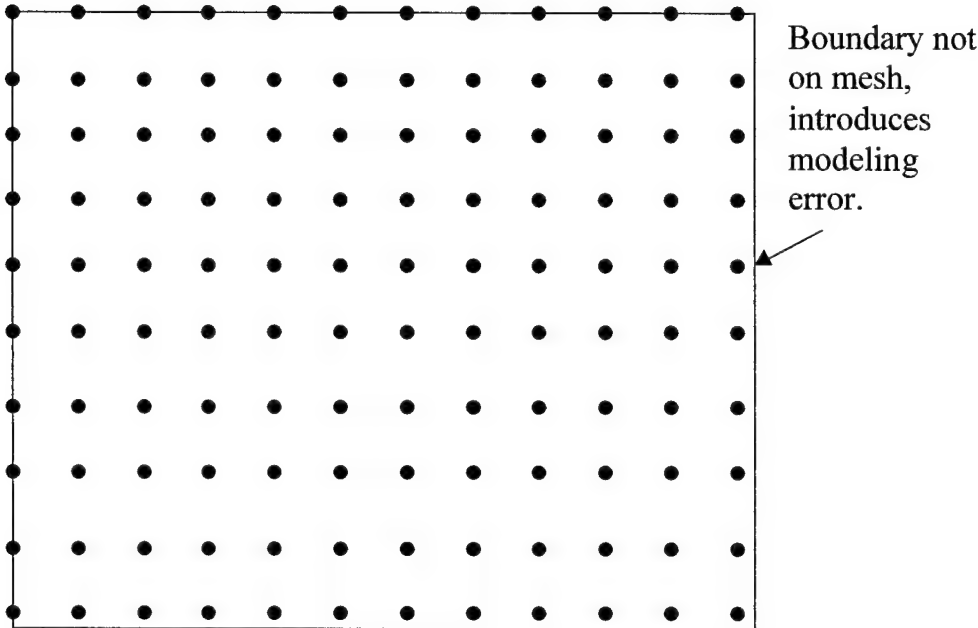


Figure 27. FDTD 2-D grid and boundary.

The third consideration is the use of plane wave excitation. When using a plane wave source, the computational domain is divided into two sections: the total field region, and the scattered field region, which excludes the incident field. Figure 28 shows the two sections. For the same reasons above, the total field boundary should lie on the grid.

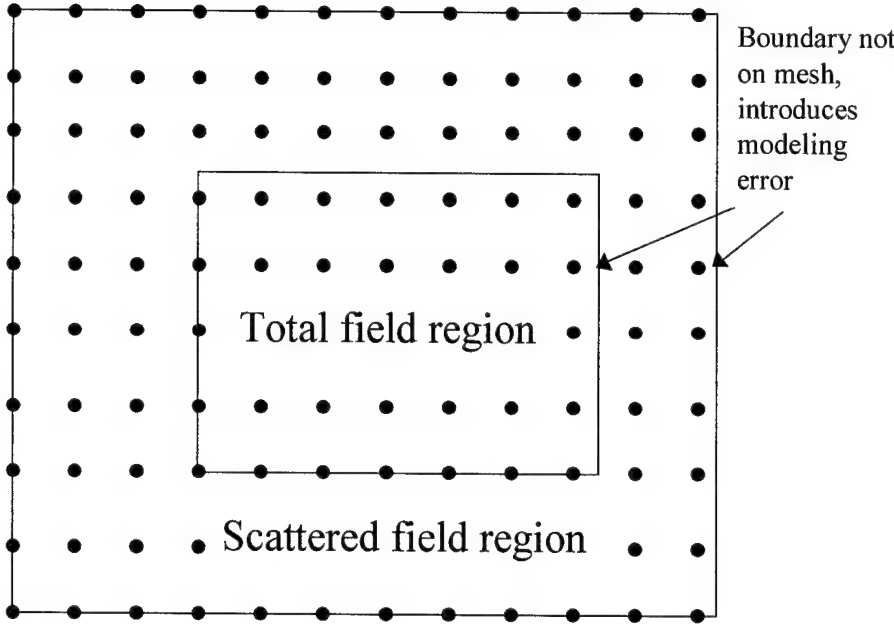
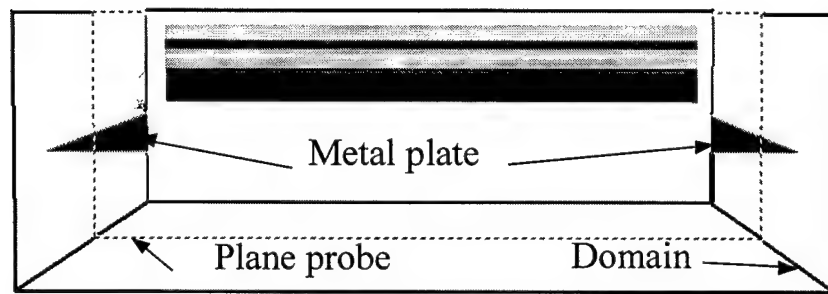
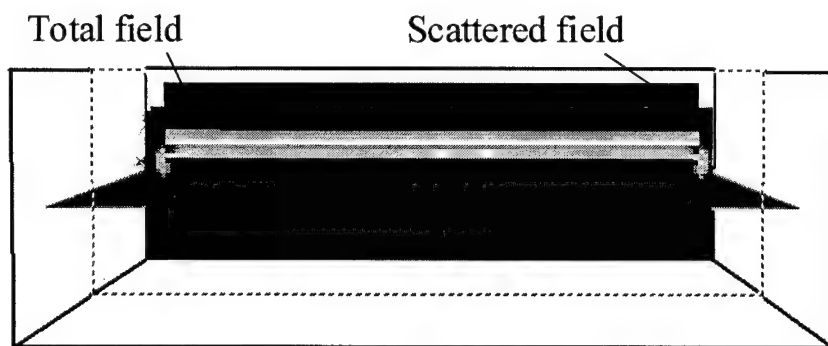


Figure 28. Computational domain for plane wave excitation.

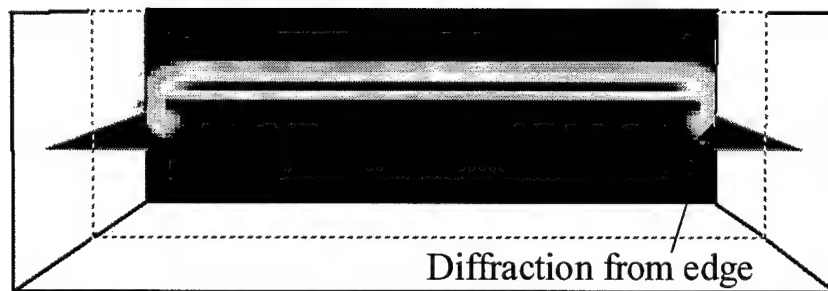
The fourth issue is numerical instability. To control stability, the time step should not exceed the magic time step. *LC* automatically calculates the time step from the user defined mesh size, thus ensuring a stable model. However, the outer boundary of the computational domain is supposed to be a perfectly absorbing boundary that prevents energy from reflecting off the outer boundary. The simulated absorbing boundary is not perfect and some energy does return to the total field region. When a large number of time steps are used in a small domain size, the repeated reflections off the outer boundary create the appearance of an unstable scattered field region which subsequently perturbs the results of the total field region. To minimize this type of modeling error, the scattered field region should be at least the same number of cells thick as the perfectly-matched-layer boundary condition [25]. As a check for these two types of modeling error, a metal plate was illuminated with a plane wave. Figure 29 shows a series of different time steps during the simulation.



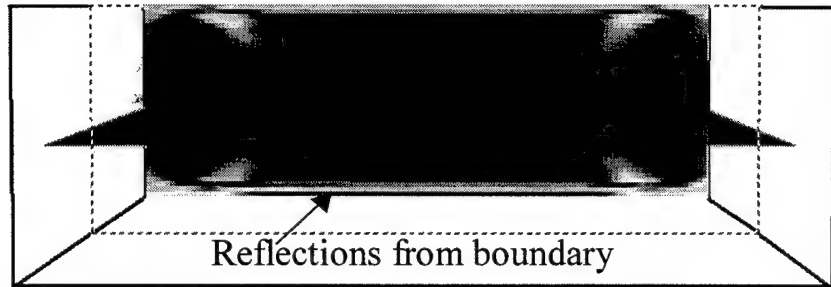
(a)



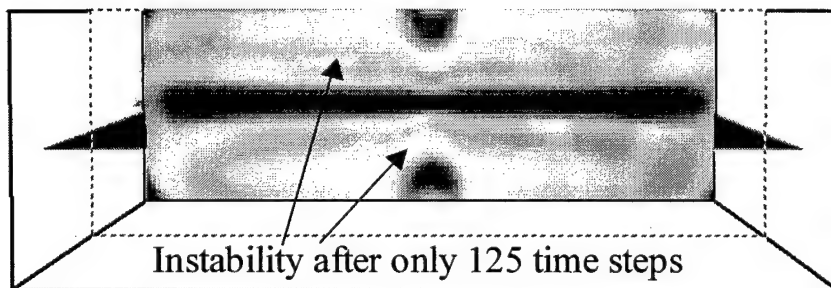
(b)



(c)



(d)



(e)

Figure 29. Plane wave incident on metal plate. (a) Incident wave before striking plate, (b) incident wave as it just strikes the plate, (c) diffraction occurs at the plate edge after reflection of the wave, (d) numerical dispersion and instability effects begin at the bottom of the grid, (e) and instability overcomes the two regions.

The heavy dark line outlines the computational domain and the dashed line is the boundary of the probe. Although the metal plate is completely enclosed in the total field region, it is only partially visible (Figure 29 (a)) by the front two corners. The magnitude of the E-field, as measured by the probe, is projected onto the back wall of the grid and overlays the metal plate. The dashed line shows the extent of the plane probe. The total field and scattered field are clearly identifiable in Figure 29 (b) by the disjointed edge of the probe plot. The black region is where

the probe value has magnitude less than 10^{-5} , the blue to red colors represent the range of the magnitude with red being the largest.

The fifth element to creating an accurate model is the probe type. *LC* allows different types of probes that can measure several types of values. To model the Focused Beam system, plane wave excitation was used and planar probes positioned at the surface of the metal plate measured the total E-field. A separate model was used for the incident field. Two models are necessary in order to separate the incident field from the total field and still preserve the proper phase information. The difference of the total field and the incident field is the reflected field.

Midcourse through the model creation, the published results of the square HIGP became available so the model of the square HIGP was explored instead of trying to properly model the Schloer crystal. The same geometry shown in Figure 17 of Section 3.3.4 was used to create the model.

The final modeling consideration was the time domain waveform of the incident field. Only the 2-18 GHz frequency range was of interest. Thus, a sinc pulse with magnitude of one was used because its Fourier Transform is a rectangular pulse. This ensured a frequency content of 2-20 GHz. Figure 30 shows the time domain signal.

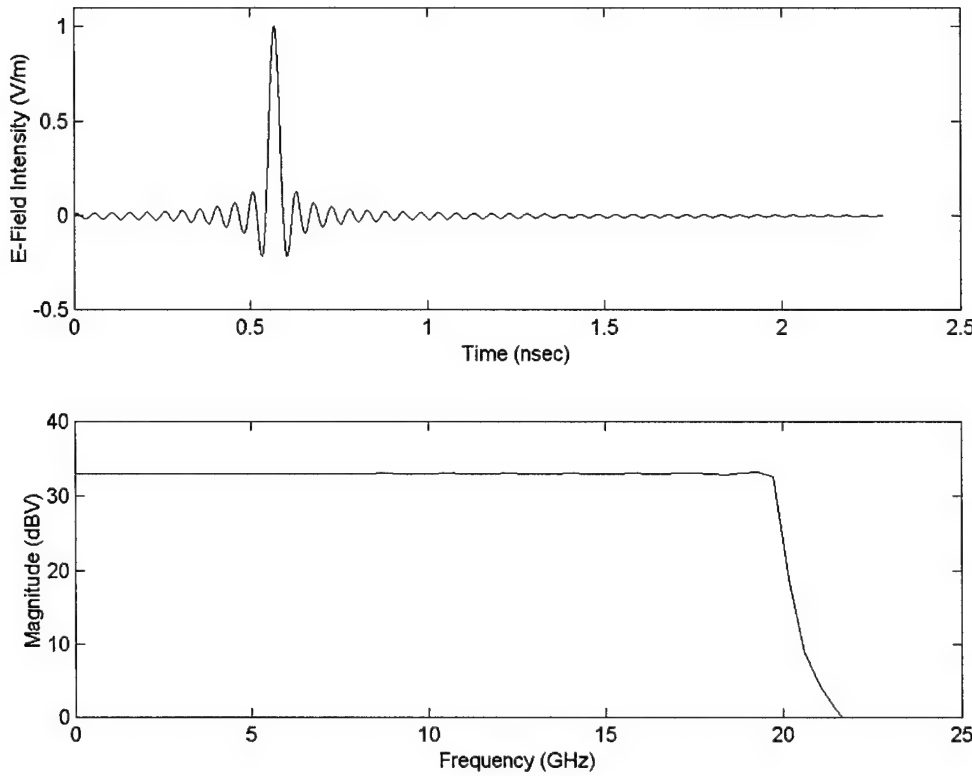


Figure 30. Time domain signal (top) of incident plane wave and corresponding frequency domain signal (bottom).

Figure 31 shows the model with a planar point probe that is set to measure the average E-field across the probe. The average was measured because the surface was non-homogeneous but still periodic. The square planar point probe extended over 42 elements. With a mesh size of 0.04 mm, the grid sufficiently sampled the geometry to include the narrow 0.15-mm dielectric spacing between metallic elements. The total number of cells was 353220, which required 132.7 MBytes of RAM and at least 3600 time steps in order to allow the reflected waveform to sufficiently decay. Γ was calculated from Equation (14) and resulted in a constant magnitude of one and a constant phase of 180 degrees. This was the same result as the metal plate. Most likely, the mesh was not fine enough to accurately represent the narrow dielectric gap of the

HIGP surface. Thus, the averaging technique did not correctly measure the E-fields in the dielectric sections and instead mostly measured the metal areas resulting in the phase response of a metal plate. Halving the mesh size would require ~256 hours to complete the test matrix. Also, the memory requirements would exceed 2 Gbytes for a four processor machine (559.4 Mbytes each). Due to the immense memory and extensive run time, it was deemed impractical to change the mesh size or continue the FDTD model.

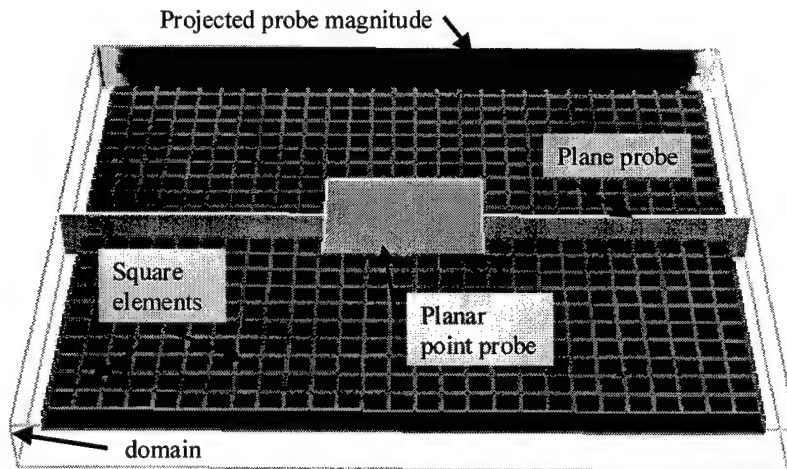


Figure 31. FDTD model of square high-impedance ground plane. Shown are the measurement probes, the domain size, the ground plane, and the projection of the E-field magnitude at one time step.

In order to reduce the computational mesh size, thereby reducing memory and simulation time requirements, periodic boundary conditions such as those discussed in Section 2.2.4 are needed to appropriately model the periodic structure's domain. Use of periodic boundary conditions would make a single cell of the HIGP appear to be infinite. This would allow a very

fine mesh and the model to run quickly with low memory needs. At this time *LC* does not support periodic boundary conditions.

An alternative method of reducing the mesh size is to use lossy materials. Lossy materials could be used to line the edge of the plate. This way edge scattered energy would be absorbed and not perturb the probe value. Then, the model could be made smaller thereby reducing the grid size. Conductive materials could be used to simulate absorbing materials, but at this time absorbing materials are not readily available in *LC*. Therefore alternative methods to model plane wave excitation of periodic structures needs to be explored in order to use the FDTD code *LC*.

4.1.2. Periodic moment method.

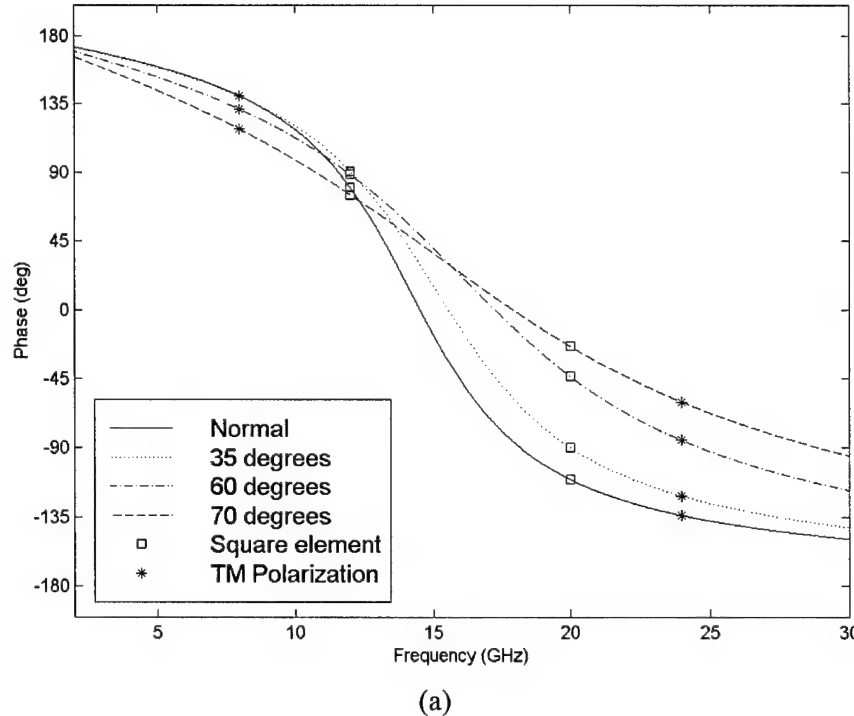
PMM results clearly show the phase response reported for both the square and hexagon high-impedance ground planes. Each frequency sweep from 2-30 GHz in 20 MHz increments was completed in 25-30 minutes on a 350 MHz desktop computer with 128 MB RAM. The increment of the simulation frequency was chosen to match the frequency resolution of the test equipment. The test matrix was completed in approximately six hours.

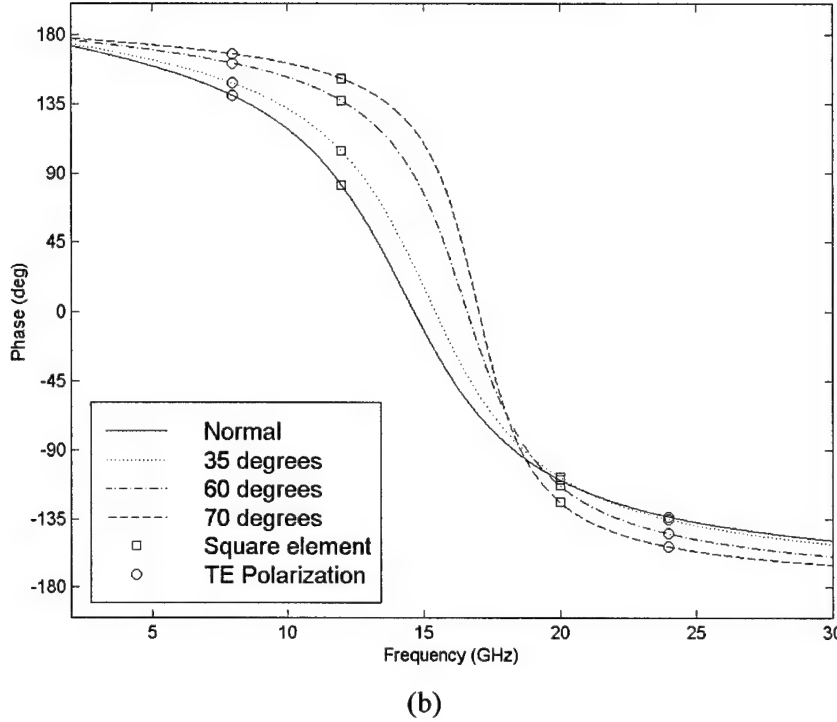
There are three variables in the test matrix given in Table 3 of Section 3.2.2 and in order to make the graphs of the results easy to read and consistent throughout this chapter the following symbols are assigned to the variable levels. The line types signify the angle of incidence, the square symbol identifies data for the square pattern, the hexagram symbol identifies data for the hexagon pattern, the star designates TM polarization and the circle designates TE polarization. These notations are summarized in Table 10. Some measurements have additional variables and they are explained in the appropriate sections.

Table 10. Symbol definitions for plotted results.

Sample	Polarization	Angle
Square: \square	TM: *	Normal: solid line
Hex: *	TE: \circ	35 degrees: dotted line 60 degrees: dash-dot line 70 degrees: dashed line

The magnitude response for all the data is a flat line with magnitude of one because the HIGP reflects all the impinging energy. For this reason only graphs of the phase response are shown. The first set of plotted data is the phase response of Γ for the square pattern at varying angles. Figure 32 shows the PMM phase response of the four illumination angles.





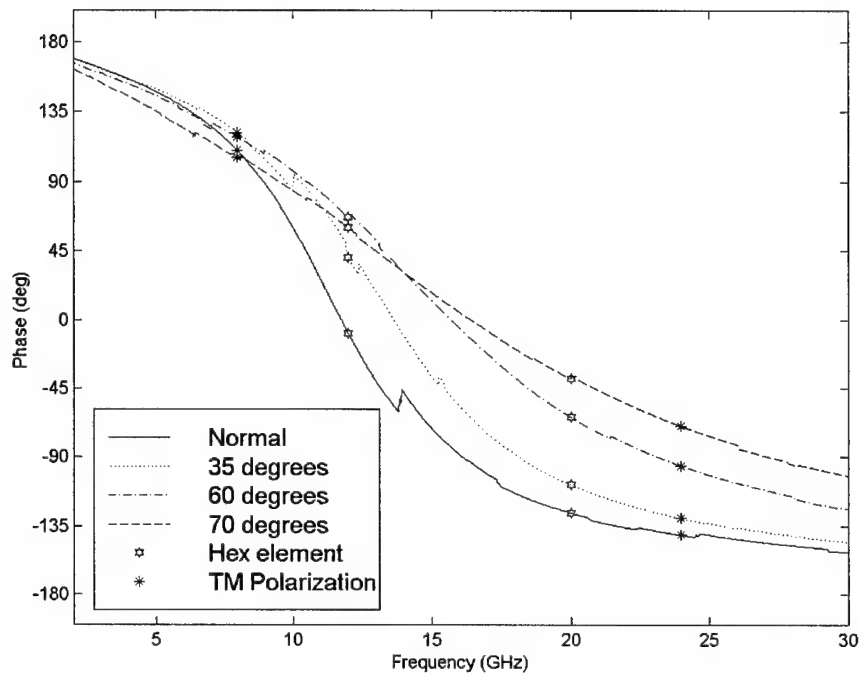
(b)

Figure 32. PMM phase response of Γ for square pattern. (a) TM polarization, and (b) TE polarization.

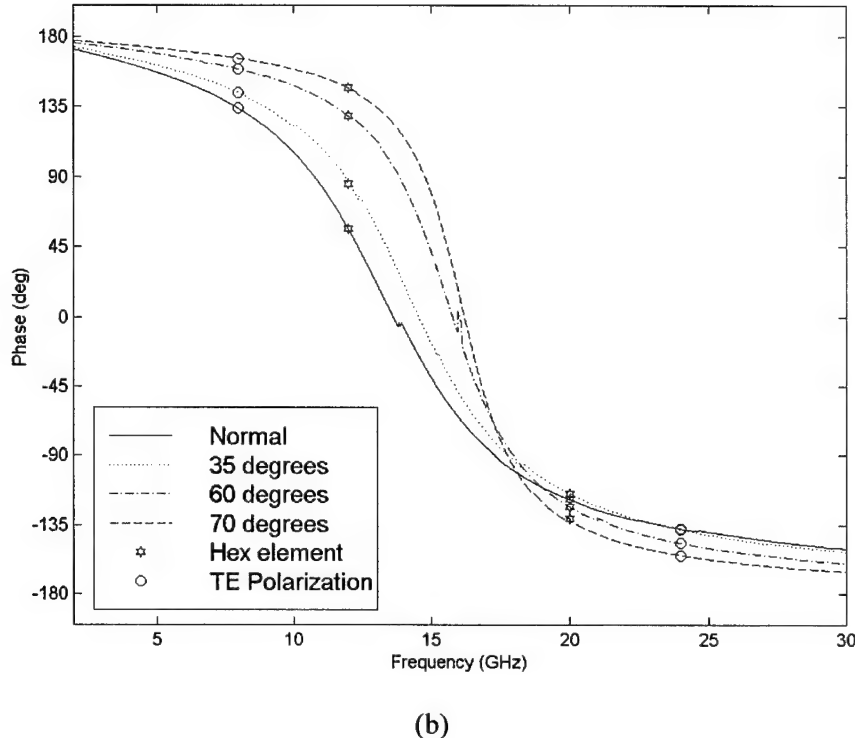
In each case there is a linear region from approximately -45 degrees to +45 degrees. The slope of the region appears to be angle dependent. For TM polarization, the slope of the phase response decreases with increasing illumination angle. However, the response becomes steeper for TE polarization.

In the case of the hexagon pattern, Figure 33 shows the phase response for TM and TE polarization. The overall response is the same as the square pattern. This suggests that the pattern shape is not important to the behavior of the phase for changing direction of incidence. It is important to note that the resonant frequency, the frequency at which the phase is equal to zero, does change with the angle and polarization. The amount of change is studied with an analysis of variance test, but first the square and hexagon phase responses are compared.

There is a small discontinuity in some of the plots shown. This can be caused by a large PMM accuracy (convergence tolerance of the double summation), trapped or grating lobes (plane waves that remain in the dielectric layer), and/or by the current modes of the modeled slots not accurately capturing the current behavior.



(a)



(b)

Figure 33. PMM phase response of Γ for hexagon pattern. (a) TM polarization, and (b) TE polarization.

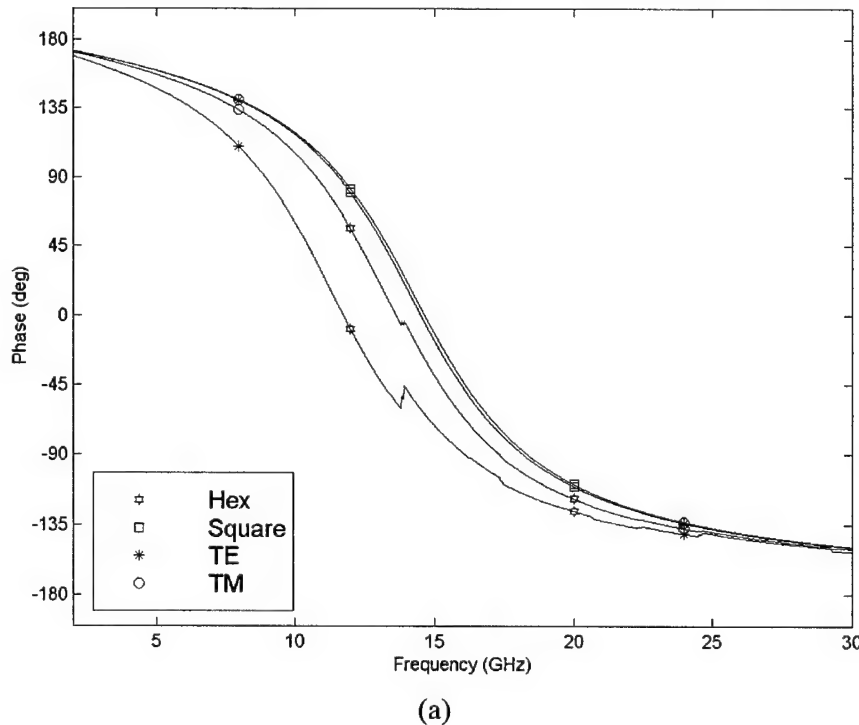
The PMM accuracy was eliminated as the cause after additional simulations at higher accuracy continued to produce the discontinuity. The accuracy was changed from 10^4 to 10^6 , but there was not a noticeable difference. The output file from PMM was checked for grating and trapped lobes but PMM did not identify any trapped or grating lobes. Most likely, the current modes are the cause of the discontinuity. Only some of the results for the hexagon pattern had this discontinuity and the square data agreed with the published results, so the current modes were unchanged.

Comparison plots of the square and hexagon elements at normal incidence are displayed in Figure 34. The graphs display both TM and TE polarization and clarify how the phase

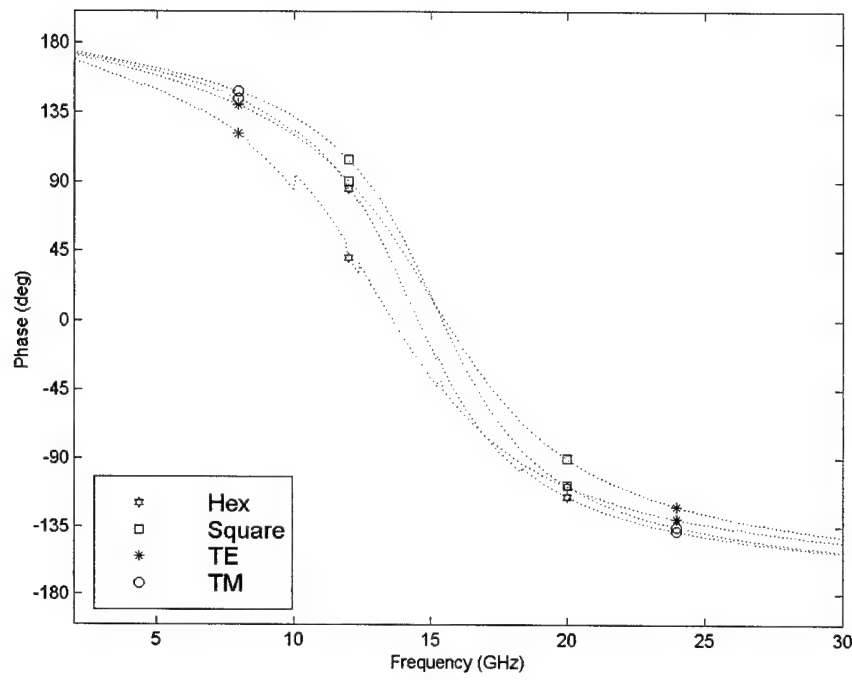
response changes differently for the TM and TE modes. The pattern of the textured surface seems to have little effect on the behavior of the response.

At normal incidence, Figure 34 (a), the square pattern has the same response for the TM and TE modes while the response of the hexagon pattern diverges between the different modes. This makes sense because the square element is seen the same for each polarization from normal incidence. However, the hexagon island has either a flat edge or a jagged edge depending on which polarization is incident.

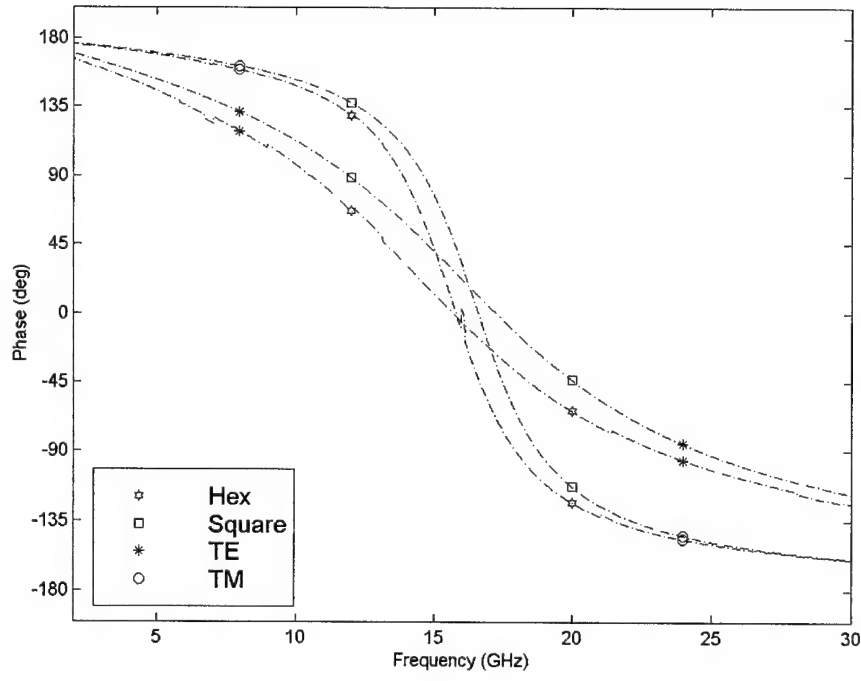
For increasing angles of incidence, the TM and TE modes illuminate the flat plate differently. TE modes are always parallel to the plate, while the TM modes become more normal to the plate as the angle increases. The pattern shapes, however, have similar trends and nearly equal phase response for corresponding polarization.



(a)



(b)



(c)

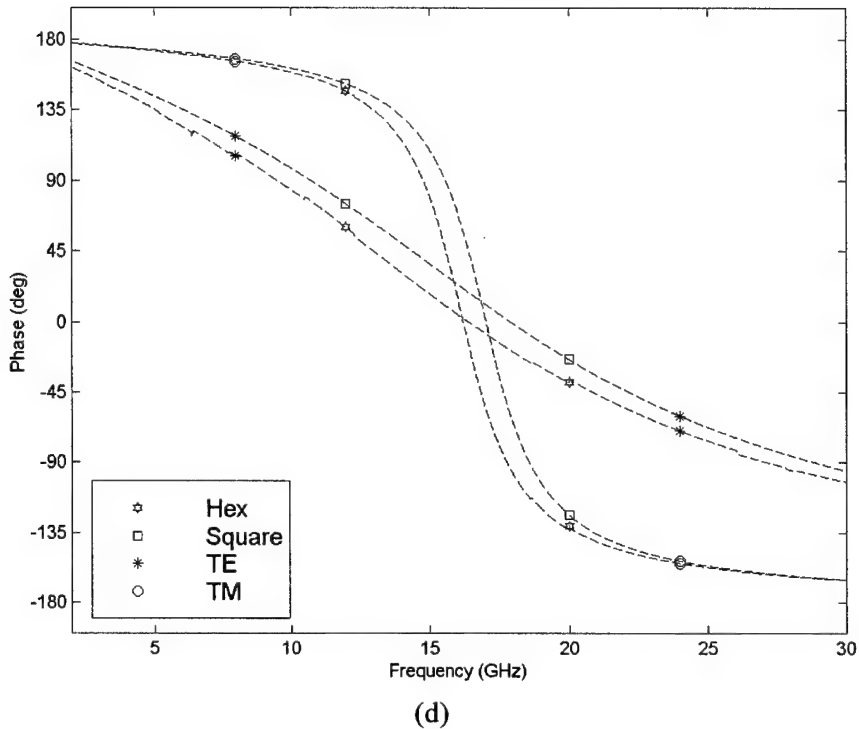


Figure 34. PMM comparisons of Hex and Square phase response for TM and TE polarization. (a) Normal incidence, (b) 35 degrees incidence, (c) 60 degrees incidence, and (d) 70 degrees incidence.

4.1.2.1. ANOVA test of PMM reflection data.

Up to now the resonant frequency, f_r , and bandwidth, BW, have not been discussed because they change given different element shapes and directions of incident E-fields. An analysis of variance (ANOVA) is used to study the way f_r and BW change.

A linear statistical model using full factorial permutations of the main effects and their interactions was used to perform an ANOVA F-test. The model is not a prediction model but rather a model to explain which effects are significant. The linear model is given by

$$y = \hat{\beta}_0 + \hat{\beta}_1(Sample) + \hat{\beta}_2(Polarization) + \dots \quad (16)$$

$$\hat{\beta}_3(Sample * Polarization) + \hat{\beta}_4(Angle) + \hat{\beta}_5(Sample * Angle) + \dots$$

$$\hat{\beta}_6(Polarization * Angle) + \hat{\beta}_7(Sample * Polarization * Angle),$$

where y is the yield (resonant frequency in GHz), β_0 through β_7 are the coefficients, and the labels in parenthesis are the main effects and interactions. Note that the interactions are treated as a single variable, thus this model is linear. An error term could be added if repeated factorials are used.

In order to compute the F-test, f_r and BW were determined from the graphs in Figure 34. f_r is determined by identifying the frequency where the phase equals zero degrees. Instead of using a -90 to +90 phase variation for calculating bandwidth, like Sievenpiper et al [18], -45 and +45 degree phase points were used because the data is linear through this region.

The results of the test matrix are shown in Table 11. The 16 values of f_r from Table 11 were linearly regressed with a least squares fit to determine the eight coefficients of Equation (16). Then a statistical F-test was calculated to determine the significance of the individual effects. At a standard alpha level of 0.05 (corresponding 95% confidence interval), significance is indicated when the F-test p-value was less than 0.05. The ANOVA model is a hierarchical model, so when an interaction had a p-value greater than 0.05, it was removed from the model, and the remaining coefficients and F-tests were recomputed. However, if a two-way interaction was not significant but the three-way interaction was significant, then the two-way interaction remained in the model.

Table 11. Results of PMM test matrix.

Sample	Polarization	Angle (deg)	f_{upper} (GHz)	f_r (GHz)	f_{lower} (GHz)	BW (GHz)
Hex	TM	0	13.138	11.729	10.462	2.676
Hex	TM	35	15.438	13.599	11.913	3.525
Hex	TM	60	18.454	15.664	13.221	5.233
Hex	TM	75	20.856	16.380	12.978	7.878
Hex	TE	0	15.187	13.602	12.325	2.861
Hex	TE	35	15.848	14.536	13.358	2.489
Hex	TE	60	16.640	15.768	14.925	1.714
Hex	TE	75	16.818	16.191	15.572	1.245
Square	TM	0	15.935	14.493	13.181	2.753
Square	TM	35	17.265	15.515	13.939	3.326
Square	TM	60	20.091	17.226	14.723	5.367
Square	TM	75	22.132	17.880	14.373	7.758
Square	TE	0	16.080	14.631	13.304	2.775
Square	TE	35	16.706	15.410	14.2060	2.500
Square	TE	60	17.469	16.581	15.732	1.737
Square	TE	75	17.631	17.004	16.388	1.242

The ANOVA results of the significant effects are listed in Table 12. The F-ratio is the ratio of the sum of squares (equal to mean sum of squares in this case) to the mean square error (not listed). The p-value (Probability > F-ratio) is calculated from an F-distribution with 1 parameter and 1 degree of freedom. The F-distribution has numerator degrees of freedom equal to $a-1$, where a equals the number of levels of the factor (Sample has two, Polarization has 2, and Angle has 4). It has denominator degrees of freedom equal to the number of degrees of freedom of the error term (Sums of Squares Error). Devore [29] gives a good description of the analysis of variance. It turns out that only the two-way interaction (Sample*Angle) and three-way interaction (Sample*Polarization*Angle) are not significant at the alpha level of 0.05.

Table 12. F-tests for PMM resonant frequency model.

Source	Sum of Squares	F Ratio	Prob>F
Sample	7.938447	78.3642	<.0001
Polarization	1.358970	13.4150	0.0044
Sample*Polarization	1.110145	10.9588	0.0079
Angle	25.780330	254.4900	<.0001
Polarization*Angle	1.428722	14.1036	0.0037

The two significant interactions (*Sample*Polarization*) and (*Polarization*Angle*) agree with theory. The interaction (*Polarization*Angle*) is directly related to the incident E-field alignment. When the E-field is TE polarized the angle of incidence has little effect, but the TM polarized E-field illuminates the ground plane differently for each angle.

The two designs differ by the lattice constant spacing (2.54 mm for the hexagon, and 2.44 mm for the square), but the main difference is due to the different interelemental capacitance of the different shapes. The hexagon is packed more densely than the square pattern and has a higher capacitance. Since capacitance is inversely proportional to frequency, f_r is lower for the hexagon than the square pattern. When the sample is combined with polarization (*Sample*Polarization*), the E-field builds up a capacitance between the plates differently for each polarization because of the way the E-field aligns with the gap. Table 13 lists the least square mean frequencies for the TE and TM modes. The standard error (the standard deviation of the data / square root of the number of replications) is the same for each because each had the same number of *Sample* replications and the error term is assumed to have constant variance.

Table 13. Least square mean resonant frequencies and standard error of PMM model.

Level	Least Square Mean	Standard Error
Hex,TE	15.024	0.1375
Hex,TM	14.343	0.1375
Square,TE	15.906	0.1375
Square,TM	16.278	0.1375

The linear bandwidth model is the same as Equation (16) except that the yield values are the calculated bandwidth values given in column 7 of Table 11.

Table 14. F-tests for PMM bandwidth model.

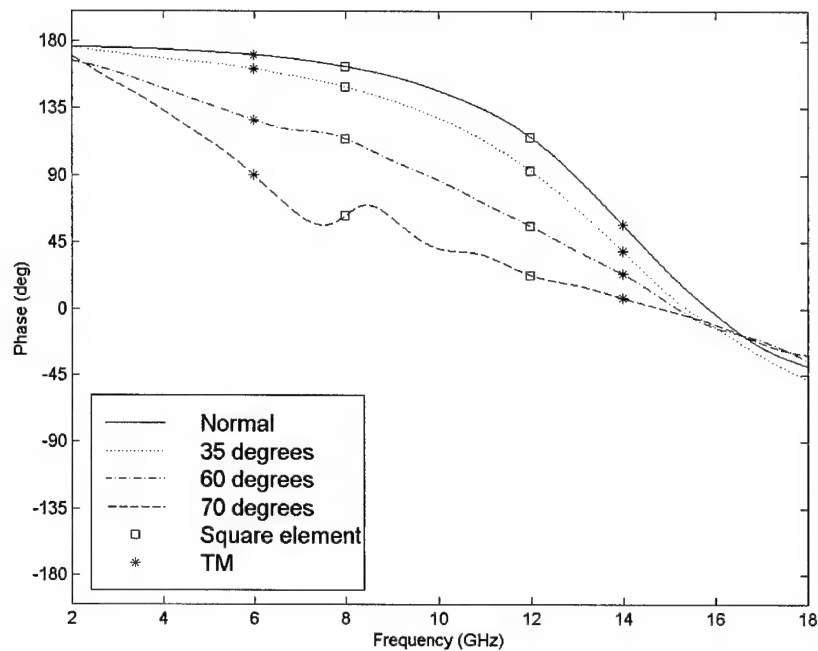
Source	Sum of Squares	F Ratio	Prob>F
Sample	0.001653	0.0035	0.9539
Polarization	0.916695	1.9390	0.1913
Angle	5.896822	12.4729	0.0047
Polarization*Angle	23.215105	49.1044	<.0001

From Table 14 it is seen that only two-way interaction (Polarization*Angle) is significant at the 0.05 level (recall that an ANOVA model is a hierarchical model as discussed earlier in this section). Although the effect *Sample* is not significant, it remained in the model because it is a main effect and removing it did not change the F-test results. Although significant, the two-way interaction (*Polarization*Angle*) does not provide any new information because the PMM model does not accurately model the TM polarization test configuration. However, the fact that the main effect (*Sample*) is not significant suggests that the bandwidth is invariant to pattern shape.

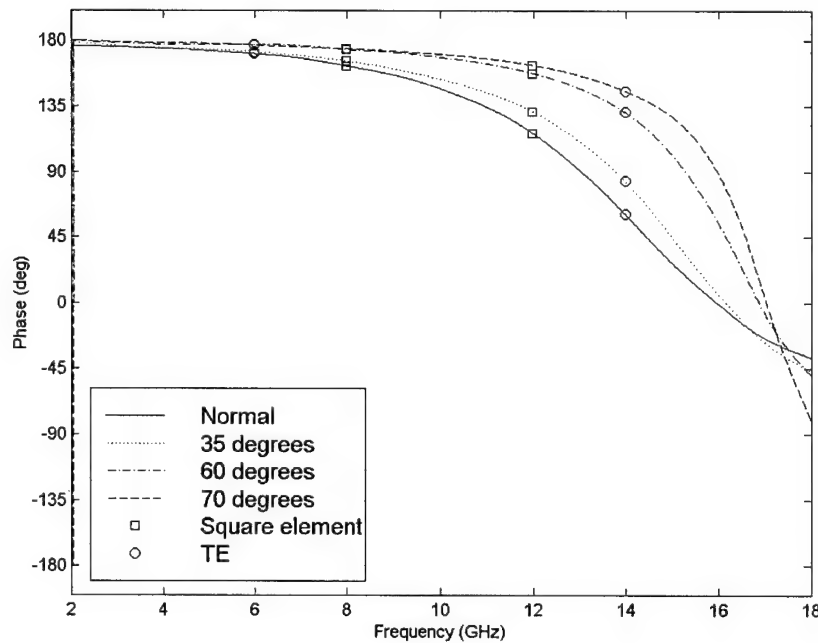
4.2. Reflection measurements.

4.2.1. Georgia Tech Research Institute (GTRI) Focused Beam.

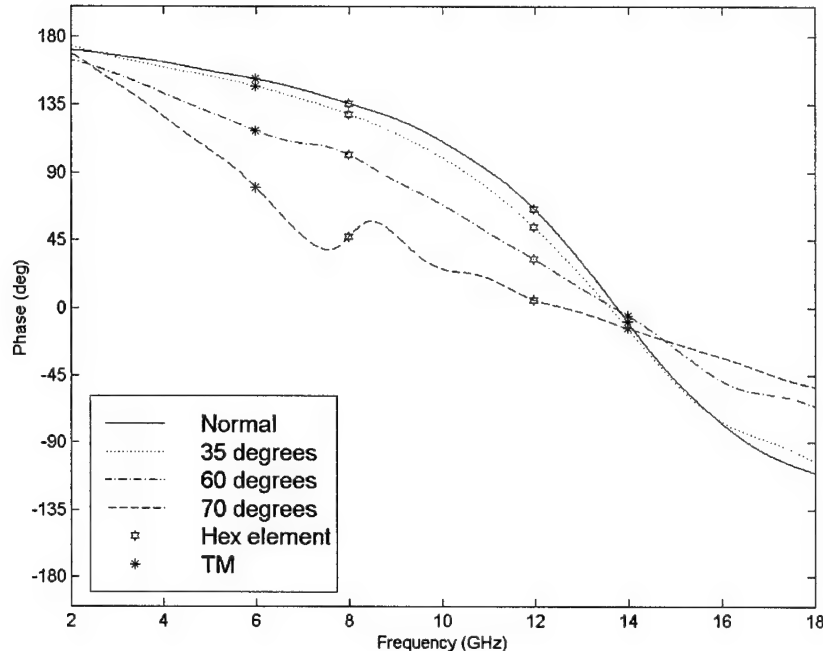
The measurement test matrix was the same as the PMM test matrix. However, the frequency range was limited to the test equipment's range of 2-18 GHz. Figure 35 shows the angle dependent phase response of the square and hexagon patterns for TM and TE polarization.



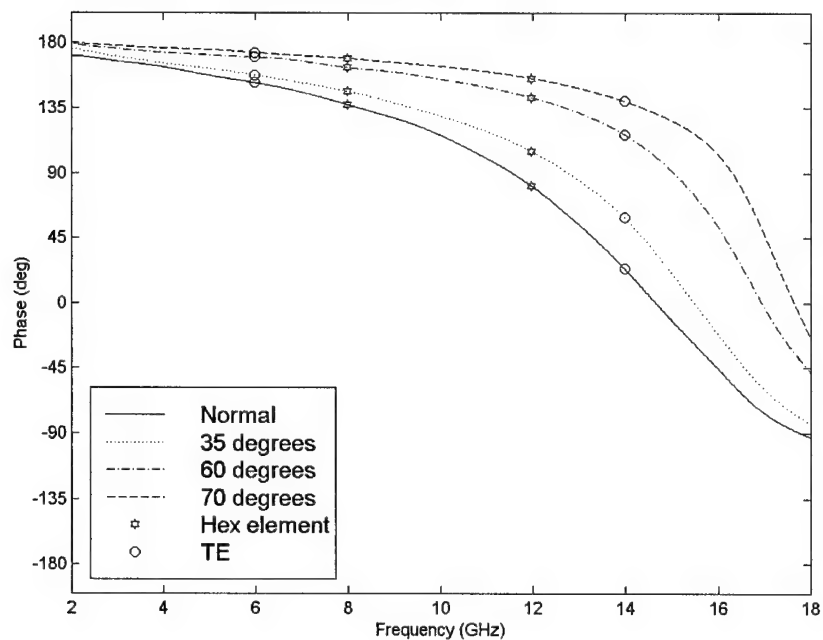
(a)



(b)



(c)



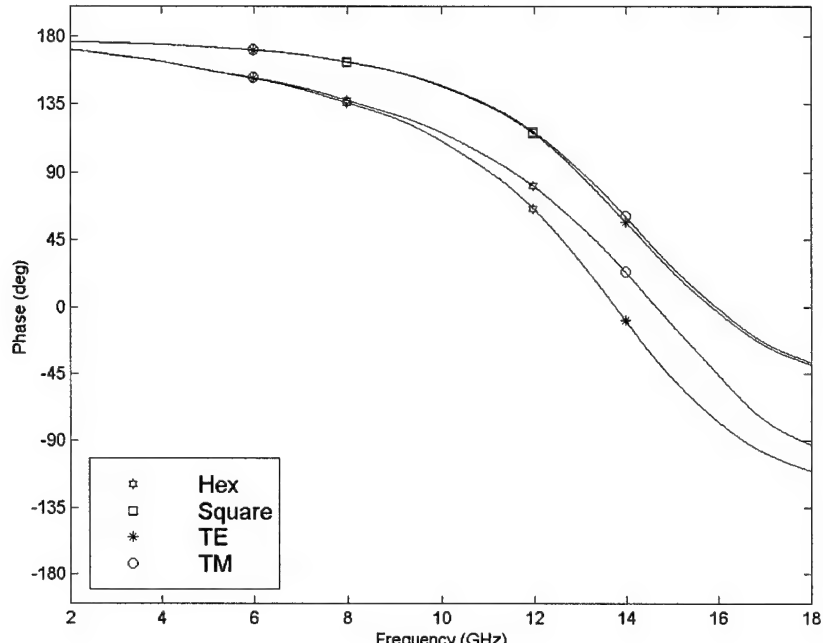
(d)

Figure 35. Measured phase response of Γ for square and hexagon using the GTRI focused beam system. (a) TM/square element, (b) TE/square element, (c) TM/hexagon element, and (d) TE/hexagon element.

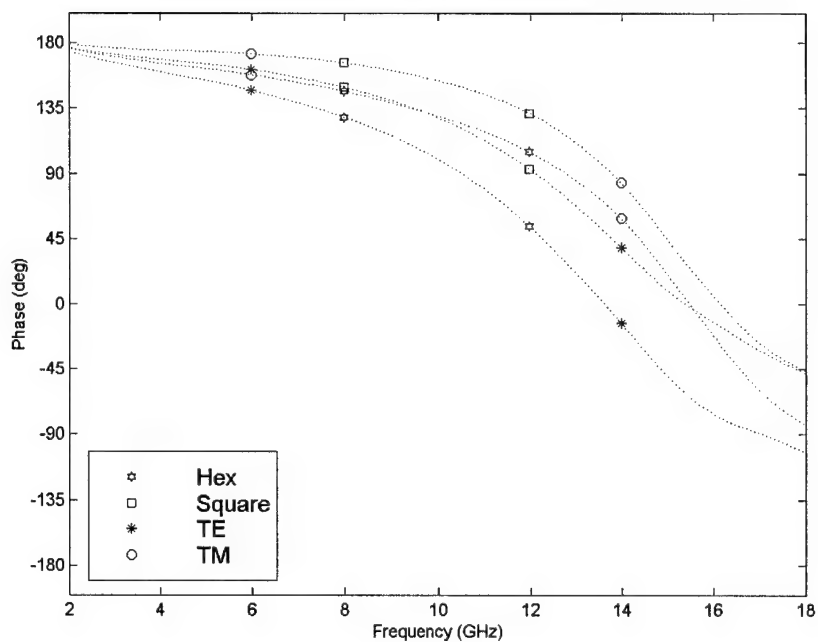
The TE mode phase response, shown in Figure 35 (b), (d) has a similar trend as the PMM prediction. This is expected because the TE polarized E-field is never aligned with the metal posts of the HIGP, so currents are not excited on the posts and the measured HIGP appears just as the PMM model, which has no metal posts.

On the other hand, the results of the phase response of TM excited wave shows a decreasing resonant frequency for increasing angle of incidence as opposed to the increasing response given by PMM (Figure 32 and Figure 33).

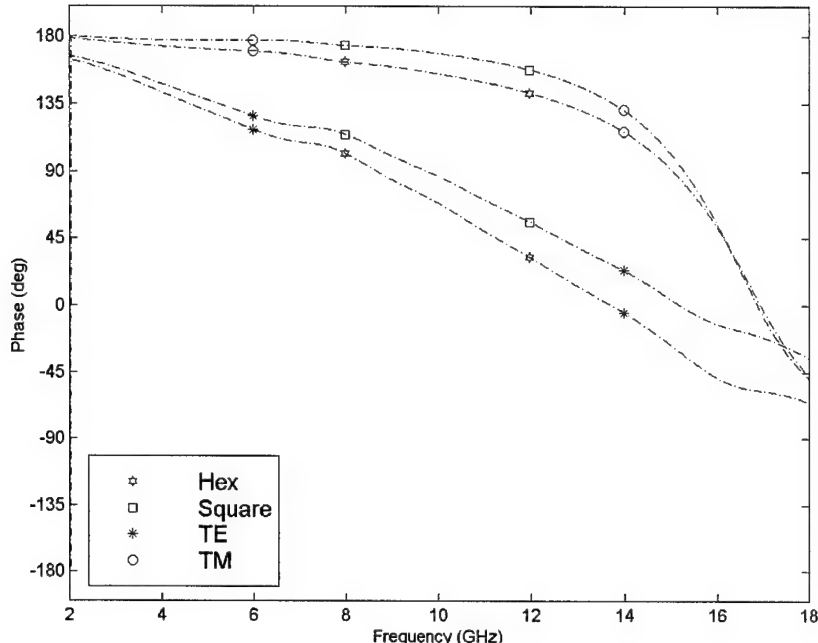
Figure 36 shows the comparison of the square and hexagon phase response. The trend is the same as PMM where the square and hexagon patterns do not appear to have a large difference, while the separation between TE and TM modes becomes more prominent at larger angles of incidence. Also, at normal incidence, the hexagon shows different TE and TM responses (Figure 36 (a)) in the high-impedance region. The phase response is sensitive to the small differences in the textured surface because the E-field is either aligned with the flat sides of the hexagon or the jagged sides. Thus, the TE and TM modes produce different fringing fields on the hexagon patch resulting in a slightly different phase response between TE and TM modes at normal incidence. Outside the high-impedance region, the phase response is similar to that for a PEC plate and the TE and TM modes are the same at normal incidence.



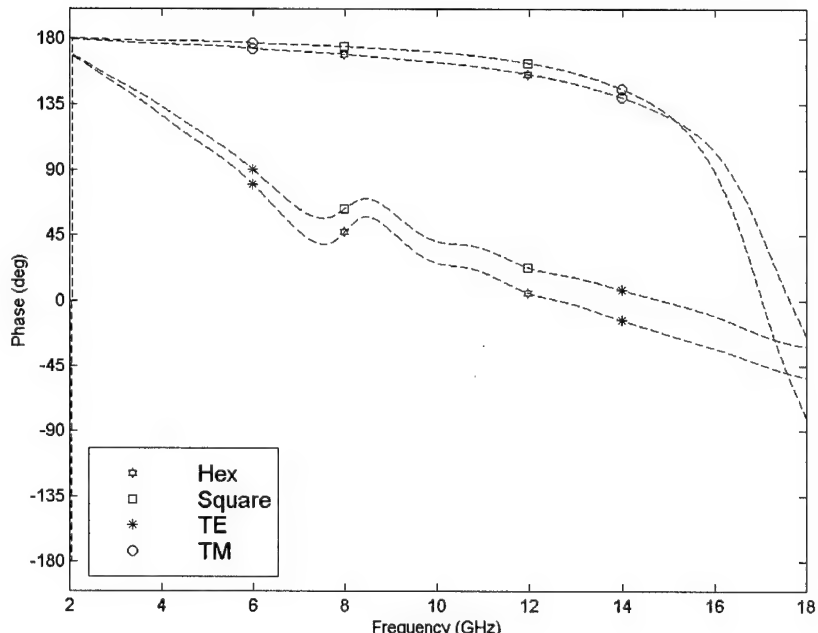
(a)



(b)



(c)



(d)

Figure 36. Focused beam comparisons of Hex and Square phase response for TM and TE polarization. (a) Normal incidence, (b) 35 degrees incidence, (c) 60 degrees incidence, and (d) 70 degrees incidence.

4.2.1.1. ANOVA test of measured reflection data.

Just like the analysis of the PMM results, an ANOVA test was used to calculate the mean resonant frequency and bandwidth. Table 15 shows the results of the focused beam reflection measurements. The last two columns are coefficients of a regressed line ($\text{phase} = \beta_0 + \beta_1 \cdot \text{frequency}$) through the high-impedance region of the phase response. The measurement equipment was limited to a maximum frequency of 18 GHz, but the upper band frequency (frequency where phase equals -45 degrees) was greater than 18 GHz for some of the configurations. A linear least squares fit of the phase was used to estimate the values identified with an asterisk.

As a check of the estimates, the linear fit of the PMM values was compared to the linear fit of the measured values by a paired t-test of the β_1 coefficients. Essentially, the slopes of the PMM data were compared, case by case, to the measured data. If the trend of the PMM data is the same as the measured data, then a ratio of the PMM slope to the measured slope should equal one. The paired t-test is the best way to show that the slopes are equal across all the test configurations [29]. The paired t-test resulted in a mean ratio of one, which gives some confidence that the estimates are good.

Table 15. Results of focused beam test matrix.

Sample	Polarization	Angle	f_{45} (GHz)	f_0 (GHz)	f_{45} (GHz)	BW (GHz)	B_0	B_1
Hex	TM	0	14.914	13.763	12.605	2.308	544.3	-39.5
Hex	TM	35	14.854	13.608	12.263	2.591	474.6	-34.9
Hex	TM	60	15.799	13.711	11.262	4.537	268.0	-19.6
Hex	TM	70	17.114	12.633	9.099	8.014	120.9	-9.5
Hex	TE	0	15.975	14.655	13.317	2.657	500.2	-34.1
Hex	TE	35	16.574	15.484	14.389	2.185	643.2	-41.5
Hex	TE	60	17.918	16.946	16.149	1.768	893.6	-52.6
Hex	TE	70	*18.272	17.640	17.027	1.244	1268.0	-71.8
Square	TM	0	*18.970	15.857	14.350	4.620	382.0	-22.5
Square	TM	35	17.793	15.384	13.785	4.008	350.0	-27.6
Square	TM	60	*18.396	15.186	12.642	5.754	236.0	-15.2
Square	TM	70	*19.567	14.854	9.682	9.884	135.0	-9.2
Square	TE	0	*17.772	15.958	14.444	3.327	447.1	-27.6
Square	TE	35	17.884	16.152	14.987	2.897	522.5	-32.1
Square	TE	60	17.860	16.879	16.162	1.698	929.2	-54.8
Square	TE	70	17.523	17.034	16.581	0.941	1662.1	-97.5

The results of the measured resonant frequency ANOVA test are shown in Table 16.

Upon comparing Table 12 to Table 16 it is seen that the significant interactions of the ANOVA tests are the same for the PMM and measured results. However the ANOVA test of the measured data does not explain why the TM modes have opposite behavior for the PMM and measured data.

Table 16. F-tests for focused beam resonant frequency results.

Source	Sum of Squares	F Ratio	Prob>F
Sample	4.9125764	25.7608	0.0005
Polz	0.0825912	0.4331	0.5253
Sample*Polz	2.4557609	12.8776	0.0049
Angle	0.8506433	4.4606	0.0608
Polz*Angle	4.9971912	26.2045	0.0005

The measured mean resonant frequencies, given in Table 17 shows that the mean PMM generated TM frequencies (Table 13) are higher than the measured mean TM frequencies.

Table 17. Least square mean resonant frequencies and standard error of measured data.

Level	Least Square Mean	Std Error
Hex,TE	16.181	0.2183
Hex,TM	13.428	0.2183
Square,TE	16.506	0.2183
Square,TM	15.320	0.2183

In terms of Sievenpiper's surface impedance model where the inductance is invariant to scan angle, the difference could be explained with an examination of how charge is generated on the metal islands and posts. Figure 37 (a) shows the square pattern HIGP that does not have metal posts and the incident TM field. By breaking the electric field vector into normal and parallel vector components, \mathbf{E}_\perp and \mathbf{E}_\parallel , it is more easily seen how \mathbf{E} builds up charge across the plates. At normal incidence ($\theta = 0 \text{ deg}$) \mathbf{E}_\parallel is the only component that builds charge across the islands. As the angle θ becomes larger, \mathbf{E}_\parallel becomes smaller, builds less charge, less capacitance, and results in a higher resonant frequency.

In the case of the measured HIGP, which has the metal posts, shown in Figure 37 (b), as θ increases, \mathbf{E}_\perp increases and excites current on the metal posts. The current generates charges on the metal islands and capacitance across the plates. The excited current generates stronger charges than the fringing capacitance generated by \mathbf{E}_\parallel , so a larger capacitance builds and results in a decreased resonant frequency. However, Sievenpiper's model is invariant to frequency and scan angle, so his model does not truly represent the physics involved.

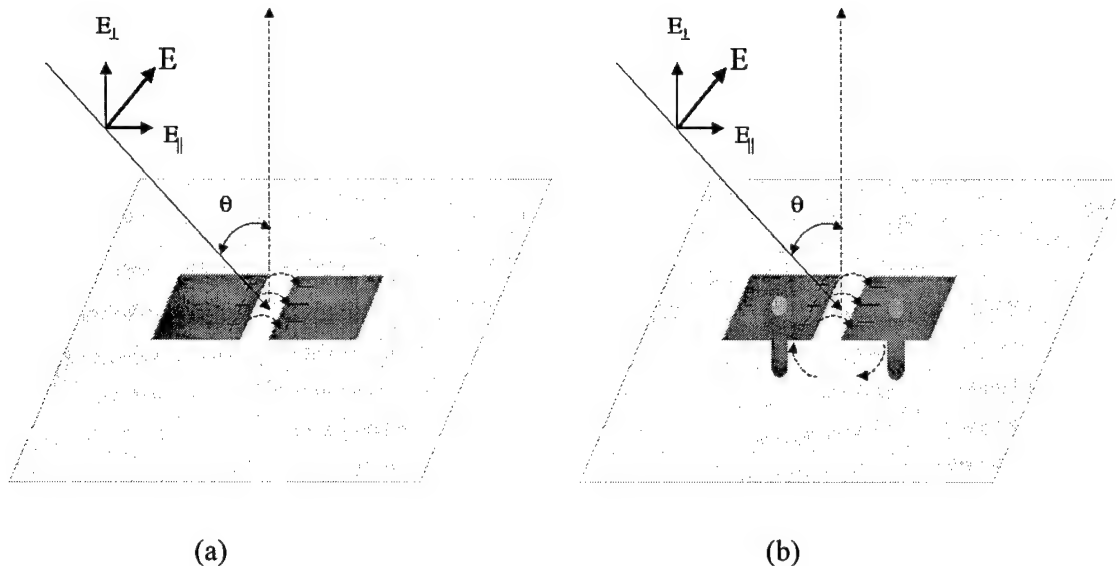


Figure 37. Electric field excitation of charge on HIGP elements.

Perhaps a more rigorous model would be to treat the metal post-filled dielectric substrate as an anisotropic media where the dielectric constant, ϵ_r , is a function of scan angle, θ . One could start with a transmission line model often used for infinitely planar periodic surfaces. This would account for the frequency dependent behavior; also, a tensor could be used in place of the constant ϵ_r , thus accounting for the interaction of the metal posts for varying scan angle.

The F-test results for the bandwidth, shown in Table 18 also agree with the PMM results. Essentially the bandwidth is invariant to the pattern, polarization, and direction of incident field, however, when *Polarization* and *Angle* are combined, the bandwidth changes. The bandwidth is primarily determined from the slope of the linear portion of the phase response and as seen from Figure 36, the slope increases with increasing angle. Therefore, the bandwidth becomes smaller. Bandwidth is polarization dependent because of the way the TM modes excite the charges on the HIGP.

Table 18. F-tests for focused beam BW results.

Source	Sum of Squares	F Ratio	Prob>F
Sample	3.825286	2.1235	0.1730
Polz	0.476142	0.2643	0.6173
Angle	4.519188	2.5087	0.1415
Polarization*Angle	24.178875	13.4221	0.0037

To show the overall difference between the PMM results and the measured results a little more clearly, Figure 38 shows the PMM and measured phase responses for normal incidence and TE polarization. The symbols are the same as previously used with the addition of the + symbol identifying PMM and the x-symbol identifying measured data. Additional comparisons are given in Appendix A. The overall trend of the curves agree with each other and show how well PMM can predict the phase response at normal incidence.

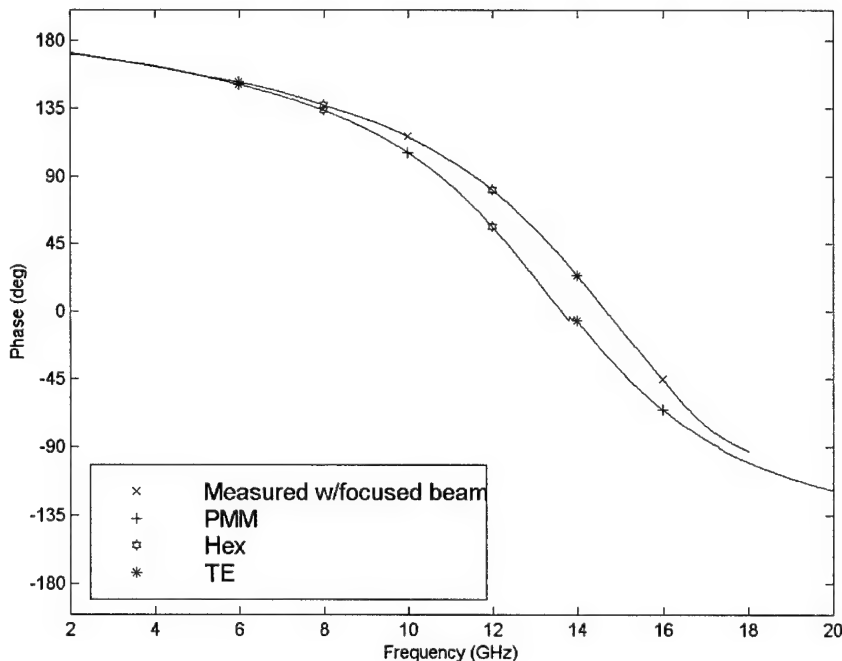


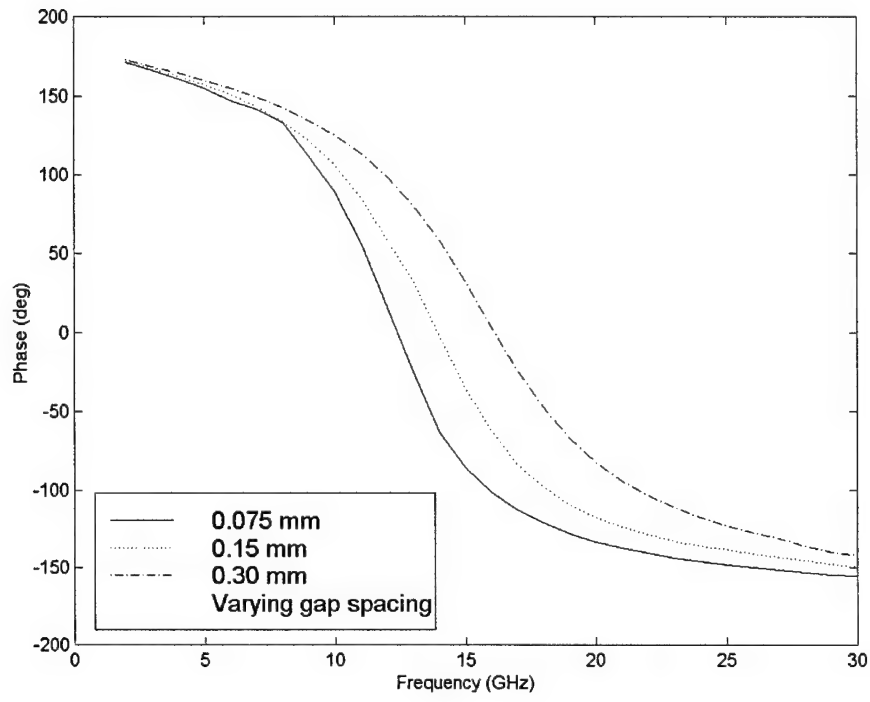
Figure 38. Comparison of PMM and measured phase of Γ at normal incidence.

Table 19 lists the actual differences between the PMM and measured results for normal incidence. The difference is on the order of 1-3 GHz, which is large for narrowband applications. Highly resonant structures such as the HIGP are sensitive to small deviations in physical size, which may account for some of the difference between the PMM and measured results. To check the sensitivity of f_r , a comparison of f_r versus varying gap sizes and varying lattice spacing are shown in Figure 39. For convenience, only TE modes at normal incidence of the square pattern are used. The large differences seen with TM modes were already explained.

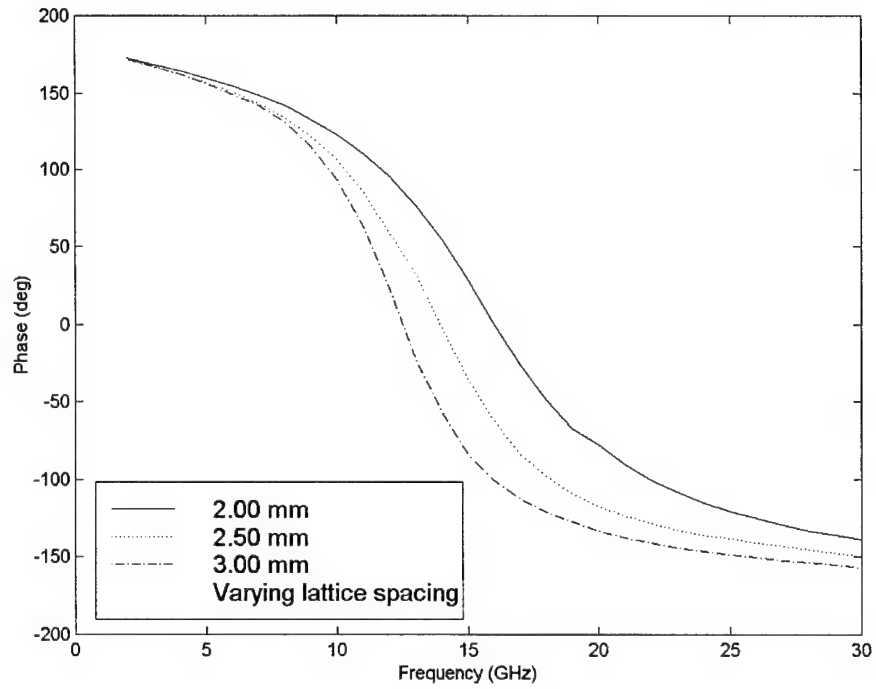
For a 0.15-mm (6 mils) increase to the gap spacing, f_r increases by nearly 1 GHz. However, an increase to the lattice spacing by 0.5-mm decreases f_r by 1.5 GHz. Although the percent change is not the same for each (100% change in gap spacing and 20% change in lattice spacing), it is obvious that the two parameters have opposite effects, but f_r is more sensitive to deviations of the lattice than the gap. Most likely, the differences between PMM TE and measured TE data result from small measurement errors. The differences between the TM data sets are the metal posts and associated effects.

Table 19. Table of comparisons of f_r for PMM and measured data.

Sample	Mode	Angle	f_r PMM (GHz)	f_r GTRI (GHz)	Difference (GHz)	%diff
Hex	TM	0	11.729	13.763	2.033	-17.340
Hex	TM	35	13.599	13.608	0.008	-0.061
Hex	TM	60	15.664	13.711	1.953	12.470
Hex	TM	75	16.380	12.633	3.746	22.872
Hex	TE	0	13.602	14.655	1.053	-7.742
Hex	TE	35	14.536	15.484	0.947	-6.519
Hex	TE	60	15.768	16.946	1.177	-7.465
Hex	TE	75	16.191	17.640	1.449	-8.949
Square	TM	0	14.493	15.857	1.364	-9.412
Square	TM	35	15.515	15.384	0.131	0.847
Square	TM	60	17.226	15.186	2.040	11.842
Square	TM	75	17.880	14.854	3.025	16.920
Square	TE	0	14.631	15.958	1.326	-9.068
Square	TE	35	15.410	16.152	0.742	-4.817
Square	TE	60	16.581	16.879	0.298	-1.802
Square	TE	75	17.004	17.034	0.029	-0.176



(a)



(b)

Figure 39. Sensitivity of f_r for varying gap and lattice spacing. (a) f_r increasing with increasing gap size, and (b) f_r decreasing with increasing lattice constant.

4.2.2. AFIT arch.

The AFIT arch technique was a check of less expensive ways to measure the phase response of the HIGP. Figure 40 shows the measured phase response of the hex and square patterns with out the absorber walls. The plot is rippled with multipath interference from the floor and nearby walls in addition to edge scattering from the ground planes. Mutual coupling between the transmit and receive antennas may be the cause of the large dip at about 6 GHz.

The plots for the absorbing wall test configuration are in Appendix A along with plots of the comparison between the two measurement techniques and PMM. Figure 41 shows one of the comparison plots and shows very good agreement. The simple far field set up can be used in a bistatic reflection configuration like the focused beam, but it requires very careful alignment.

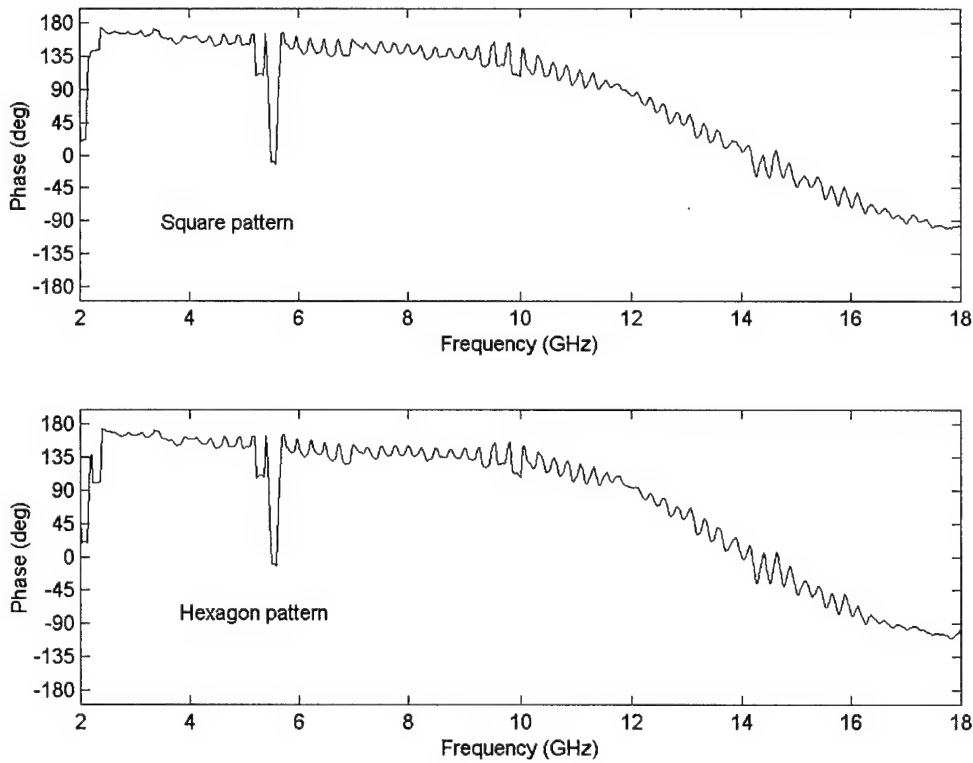


Figure 40. Far field reflection measurement results at normal incidence. (a) Square pattern, and (b) hexagon pattern.

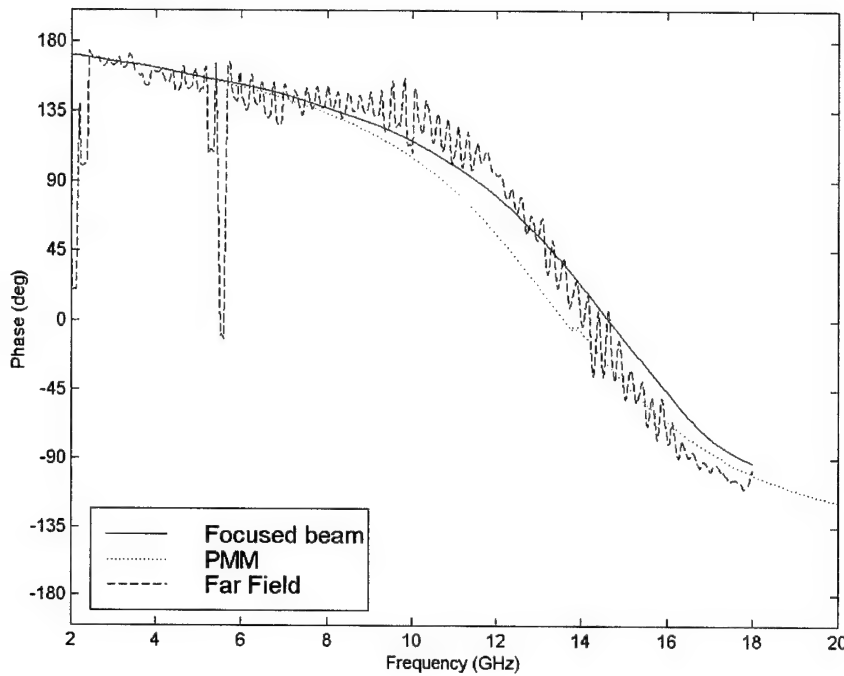


Figure 41. Comparison of PMM, focused beam, and far field reflection data. Data shown is for the square pattern at normal incidence.

Table 20 summarizes the estimated (the plots were too rippled to apply accurate smoothing techniques) resonant frequency and bandwidth. They are in close agreement with the more sophisticated focused beam results, so this technique is still a viable technique for normal incidence reflection measurements.

Table 20. Results of far field reflection measurement.

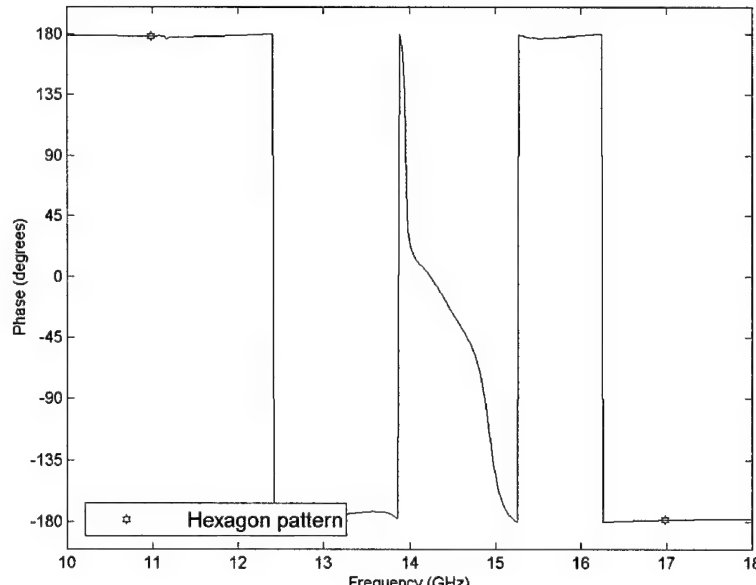
Sample	Absorber walls	f_r (GHz)	± 45 degree Bandwidth (GHz)
Hex	Yes	14.35	13.25-15.2
Hex	No	14.45	13.15-15.25
Square	Yes	13.675	12.9-14.6
Square	No	14.45	12.9-15.7

4.2.3. Waveguide Probe.

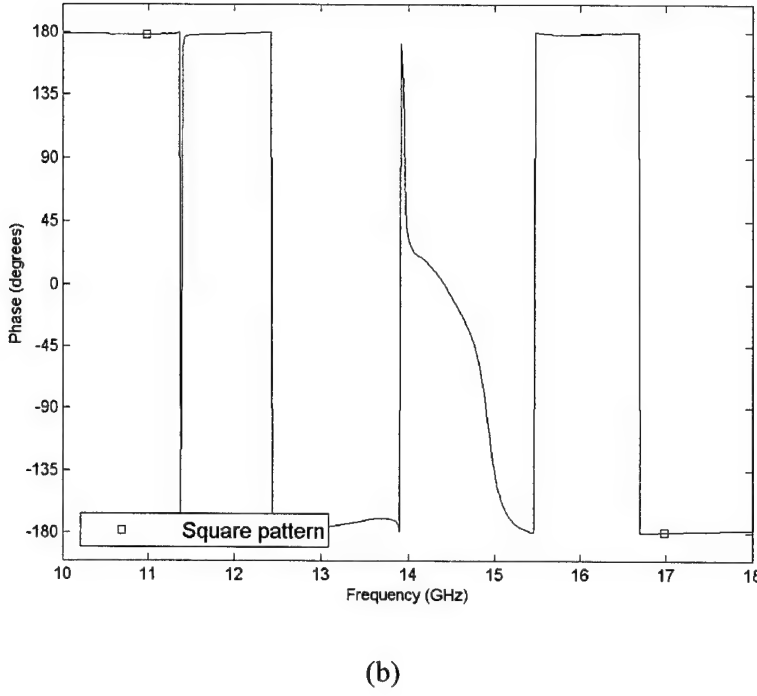
Manufacturing of the HIGP proved to be difficult because the plated through holes were not uniformly plated on the first two attempts. With over 13,000 holes, it was quicker to probe the board in a random sequence (64 probe values) and statistically check the variance than to measure the continuity. The results of the waveguide probe technique are listed in Table 21 where f_r is still the frequency where the reflection phase is 0 degrees. Typical plots of the phase are shown in Figure 42. It is important to note that waves do not exit the waveguide normal to the aperture so the resonant frequency does not correspond to the same angle of incidence as the focused beam and far field measurements at normal incidence.

Table 21. Mean resonant frequency of waveguide probe measurement.

Sample	Mean f_r (GHz)	Standard deviation f_r (GHz)
Hex	14.181	0.057
Square	14.379	0.055



(a)



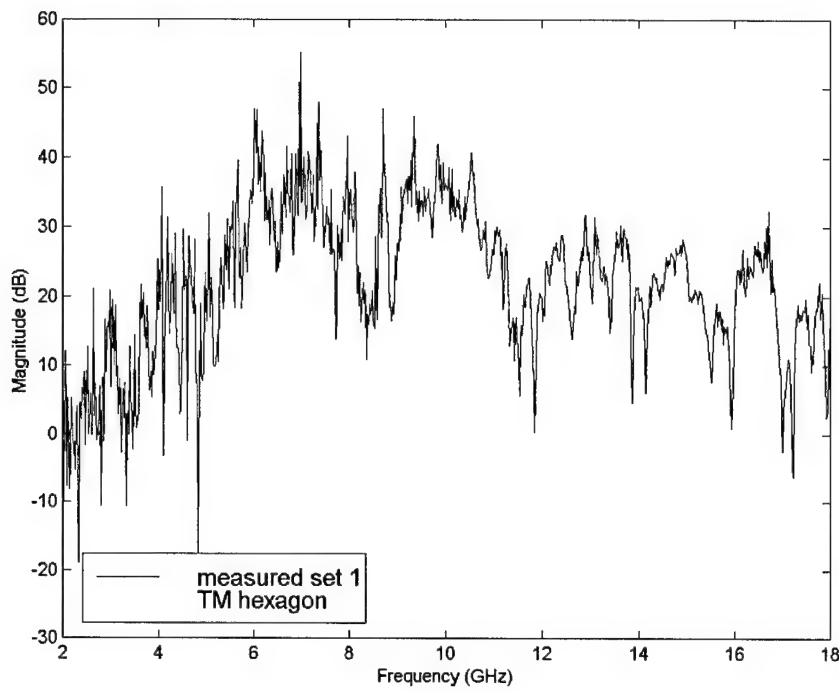
(b)

Figure 42. Typical waveguide probe measurement of Γ . (a) Hexagon pattern, and (b) square pattern.

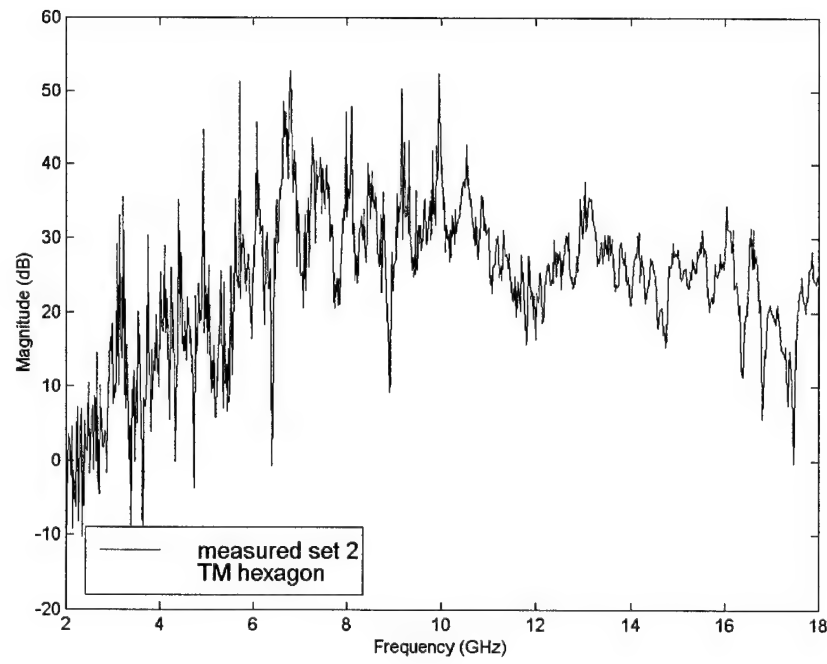
4.3. Surface wave measurements.

4.3.1. Planar HIGP surface wave coupling.

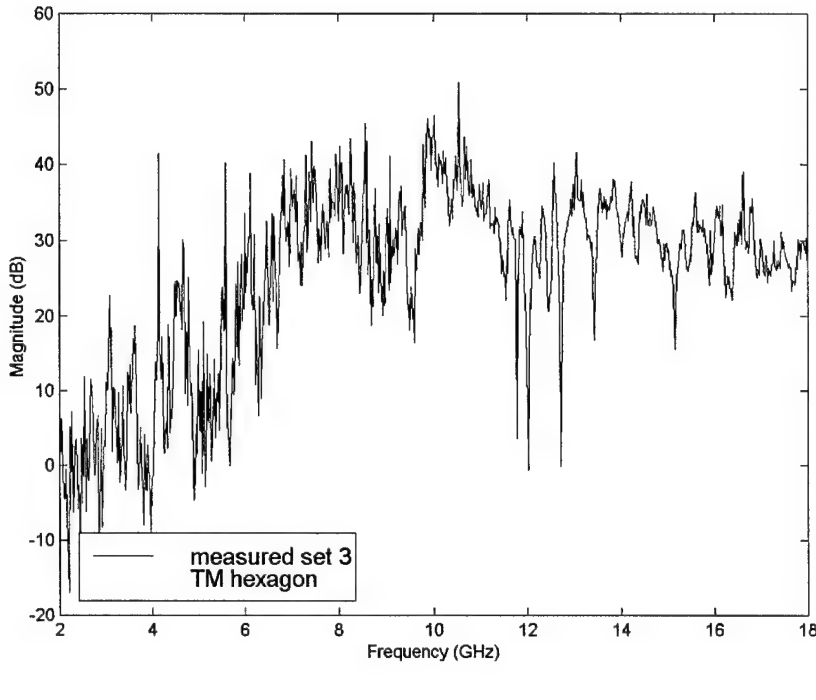
Except for the PEC plate, the planar TM surface wave coupling measurements did not produce the published results of [18]. They were in fact highly unrepeatable. Figure 43 shows a comparison of three different measurements of the hexagon HIGP. The results are normalized to a PEC plate via the thru response calibration of the HP8510. However, the results are inconclusive because of the non-repeatable nature of the measurement. The unnormalized data was of very small signal strength near the noise floor. Since the noise is random, the data fluctuates and normalizing the data only worsens the effect. Thus, the TM coupled measurements were not performed for the planar ground planes.



(a)



(b)

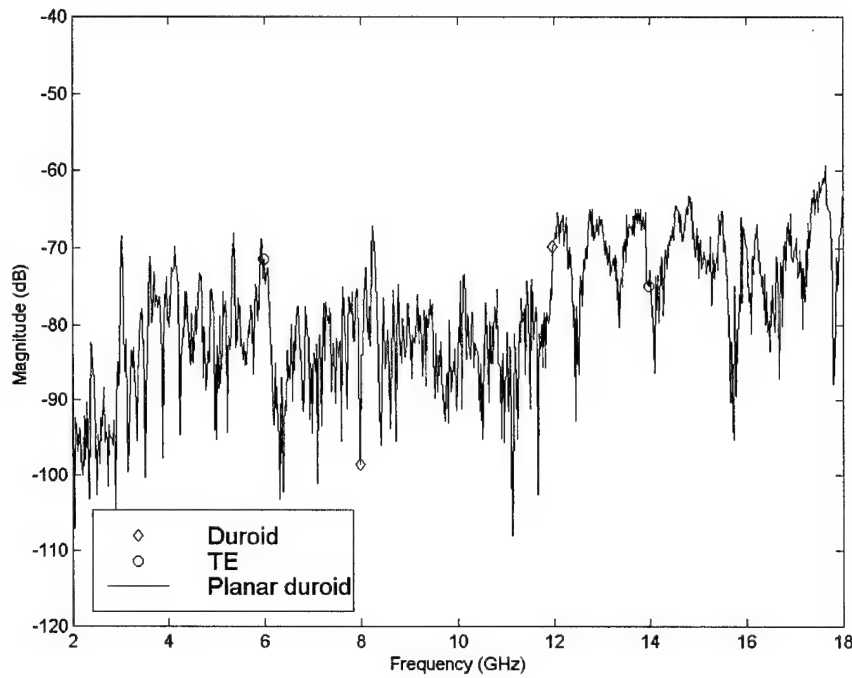


(c)

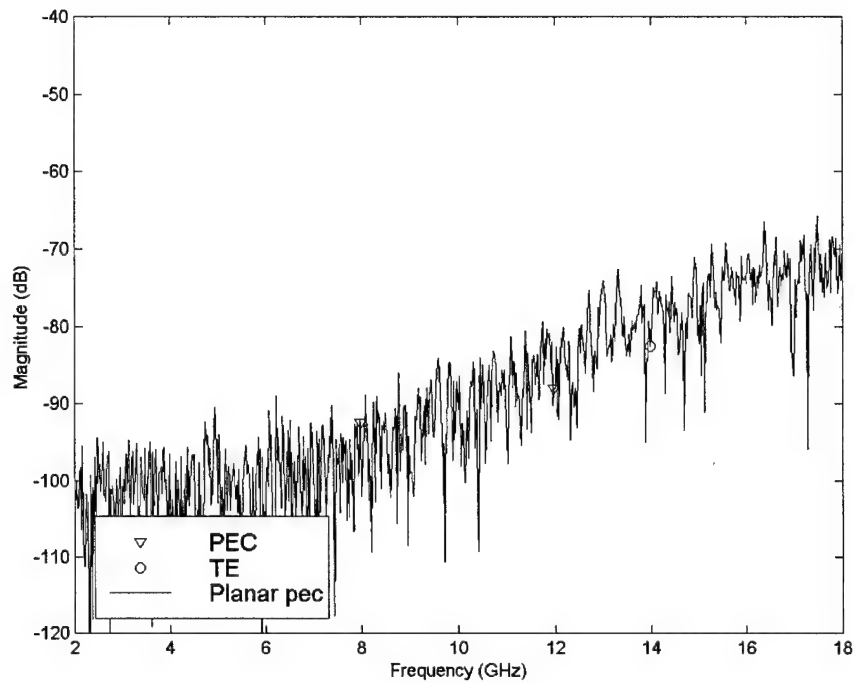
Figure 43. TM coupled surface waves on planar hexagon HIGP. (a) measurement 1, (b) measurement 2, and (c) measurement 3.

TE surface wave coupling on the planar ground planes was measured from 2-18 GHz with the probes separated by 6 inches. The response calibration discussed in Section 3.5.1 was not used because the signal strengths were so small that the calibration could not segregate the surface wave component from the noise level. Instead, the raw magnitude data plots are shown in Figure 44. The PEC plate shows the expected results of nearly complete cancellation of the E-field because the signal strength is at the noise floor over the entire measured frequency spectrum. Figures (b), (c), and (d) agree with Sievenpiper's [19] results but they include contributions from the direct signal, reflected and multipath signals, surface waves, and noise. The highly rippled values at -70dB and less were highly varying between successive measurements and are most likely due to noise. Increased averaging and use of an RF amplifier to increase the signal did not

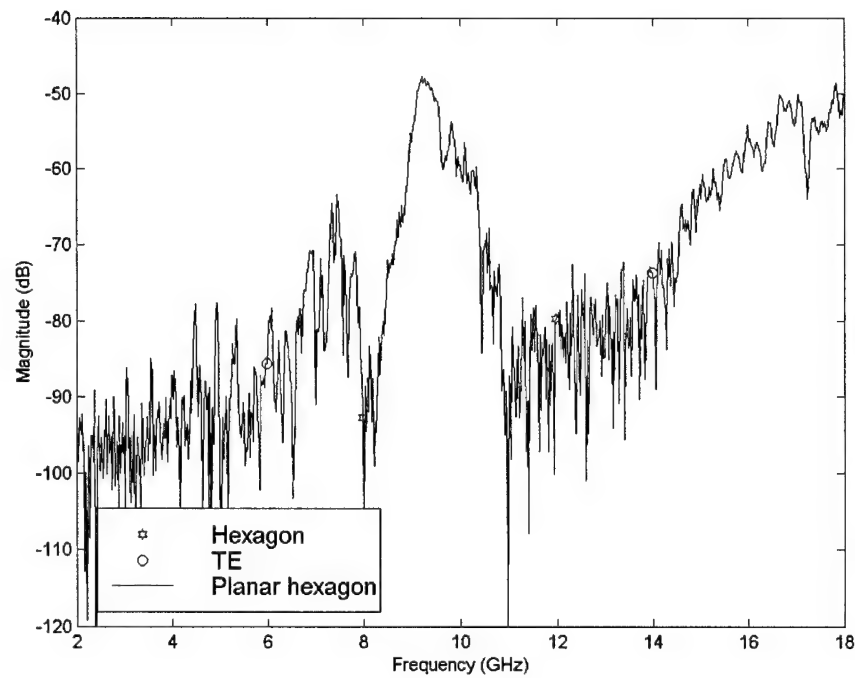
change the results. The stronger values (between 8-10 GHz in Figure 44 (a), (d)), due mainly to the direct and reflected signals, were repeatable but can not be discerned from the surface wave component without the benefit of the conformal measurement, which does not include them.



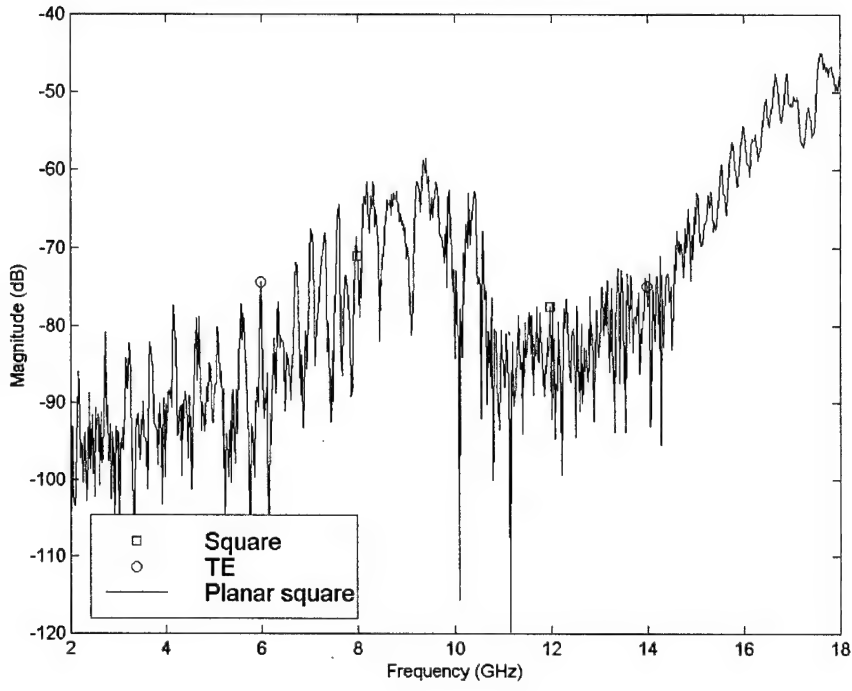
(a)



(b)



(c)



(d)

Figure 44. TE surface wave coupling. On planar (a) duroid 5880, (b) PEC, (c) hexagon HIGP, and (d) square HIGP.

The large increase in signal strength from 8-11 GHz, and above 14 GHz, is possibly due to guided waves in the dielectric substrate. This could imply that the region from 11-14.5 GHz is a photonic band gap, but the results for the 11-14.5 GHz region are the same as those of the PEC plate. Based on these measurements, it is uncertain if photonic band behavior was measured in spite of what Sievenpiper et al reported.

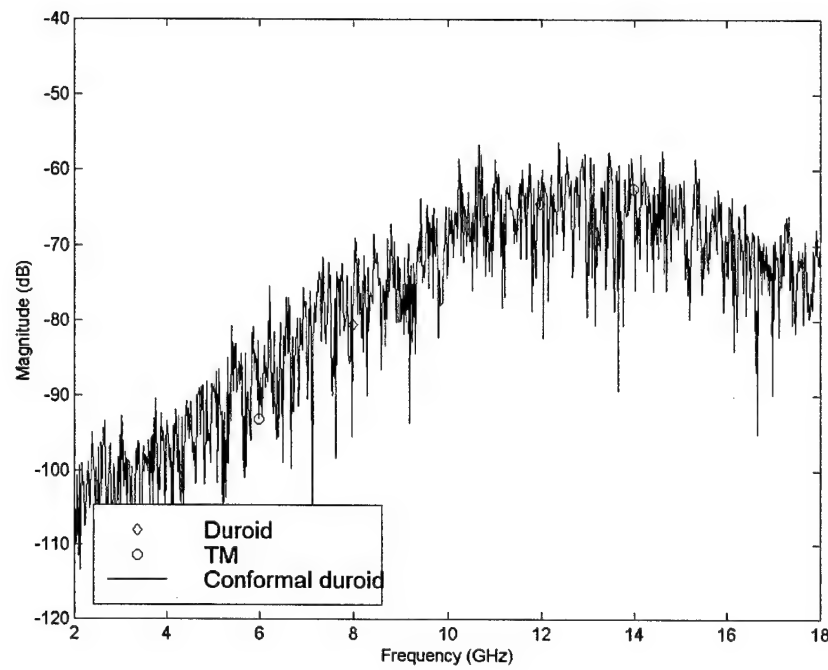
4.3.2. Singly curved HIGP surface wave coupling.

The conformal TM coupling measurements were made with the doghouse test fixture, shown in Figure 45, using probes separated by 28 inches and the signal amplified by 20 dB.

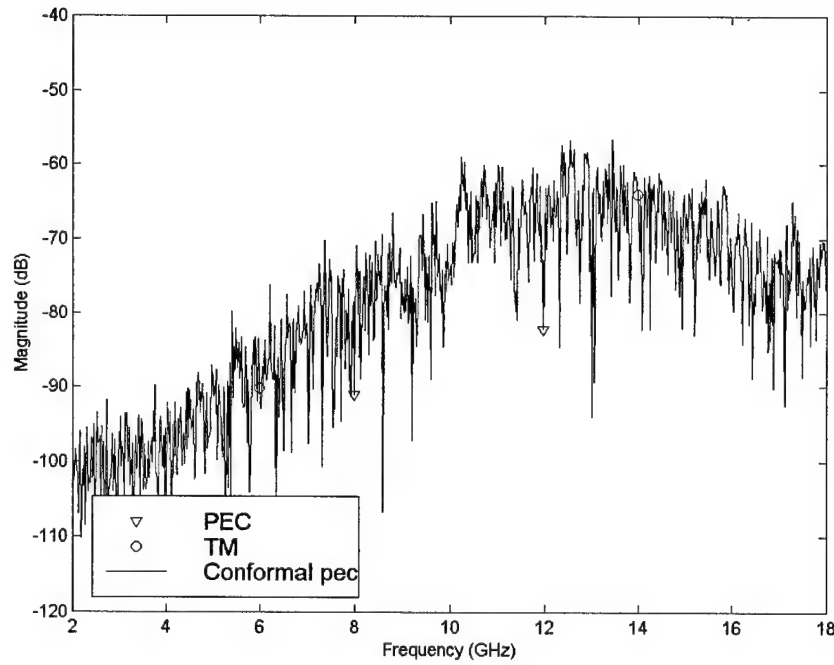


Figure 45. Doghouse test body for surface wave measurements. Shown with high-impedance ground plane in window, and reference plate.

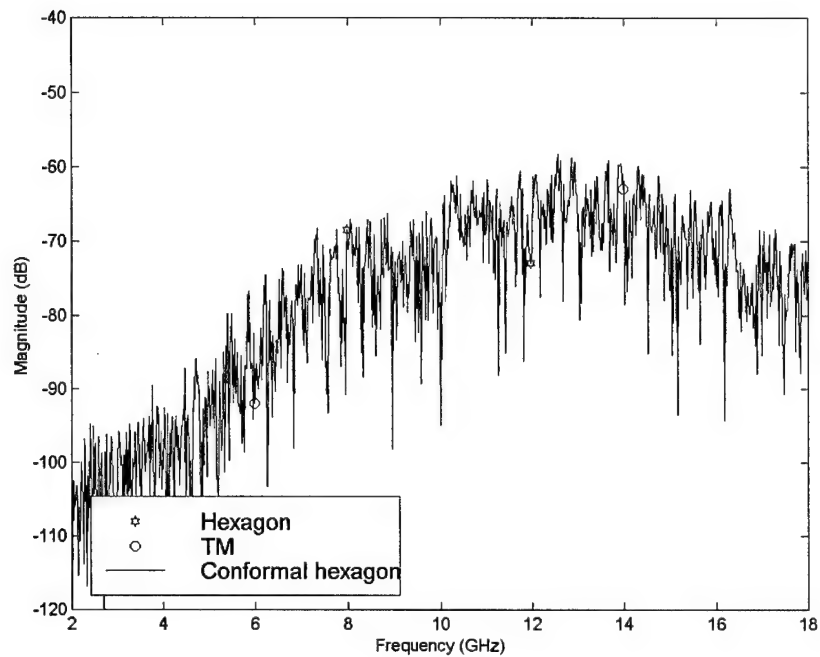
However, the curved set was no more successful than the planar TM measurements. Figure 46 shows how each ground plane has the same response. This suggests that either the surface waves are of such small magnitude that they can not be discerned from the noise or that this technique is not accurate for measuring surface wave coupling. Measurement of the coupling with the probes separated by 6 inches, shown in Figure 47, showed that the signal is still very weak even at a small probe separation.



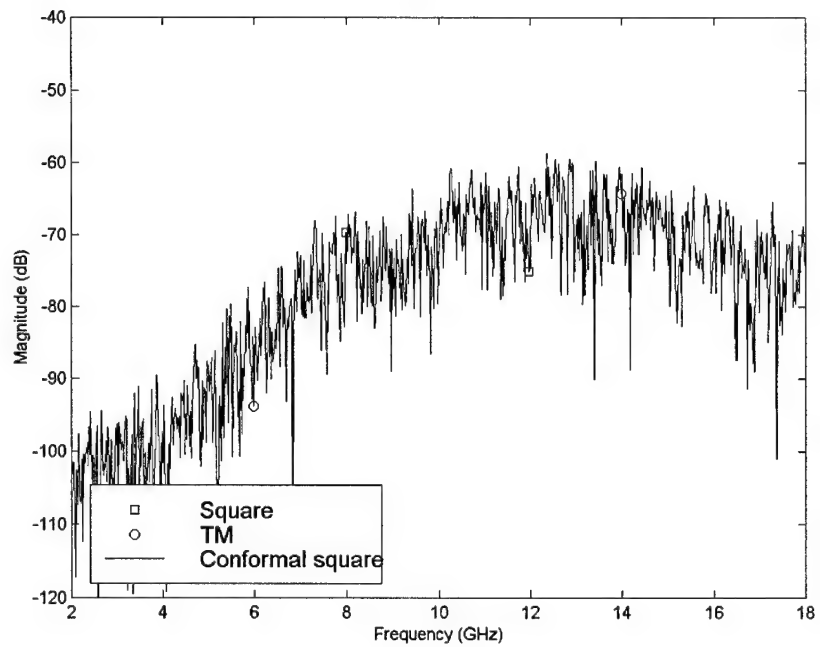
(a)



(b)



(c)



(d)

Figure 46. TM surface wave coupling on conformal ground planes. (a) Duriod 5880, (b) PEC, (c) hexagon HIGP, and (d) square HIGP.

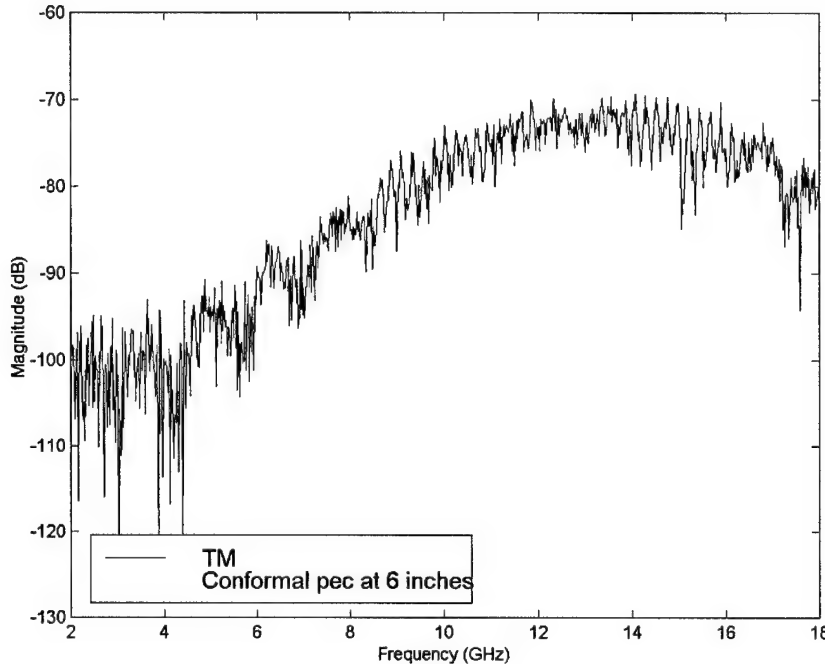
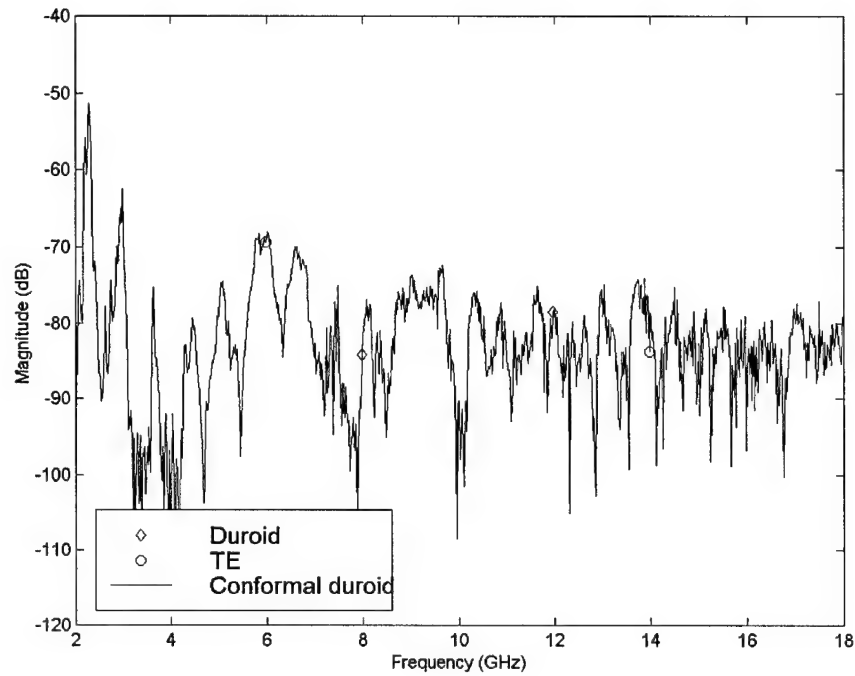


Figure 47. TM surface wave coupling on pec plate with 6 inch probe separation.

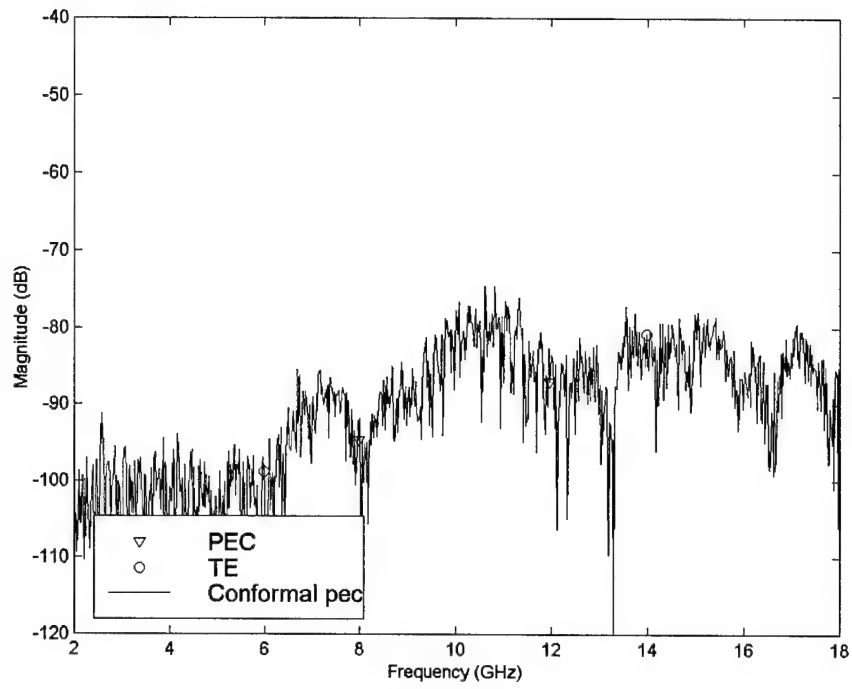
Figure 48 shows the surface wave coupling results of the singly curved ground planes. The measurement data is raw magnitude for comparison to the planar measurement. The conformal measurements are also of 6 inch separated horizontal probes, but the direct and reflected components are removed because there is no direct path between the probes except along the surface. Upon comparing these to the plots of Figure 44, it is clear that the large signal strength from 8-11 GHz and above 14.5 GHz is principally due to direct and reflected components. Without these contributions in the conformal measurements, Figure 48 shows the surface wave coupled data.

The duroid sheet, Figure 48 (a) shows fairly constant coupling. A few spikes occur below 6 GHz which are possibly due to the surface waves, and Figure 44 (a) did not show them because they were cancelled by the direct and reflected E-field components. The PEC plate,

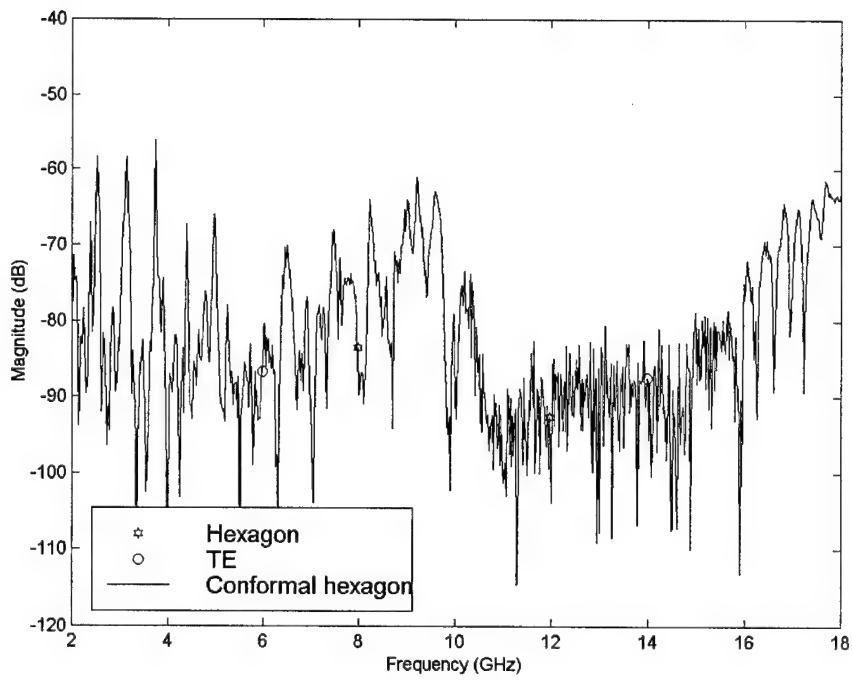
shown in Figure 48 (b) shows less coupling all across the spectrum, but it is still at the noise level. Since the region above 14 GHz is lower than that shown in Figure 44 (b), it is most likely that there was in fact some direct coupling across the pec.



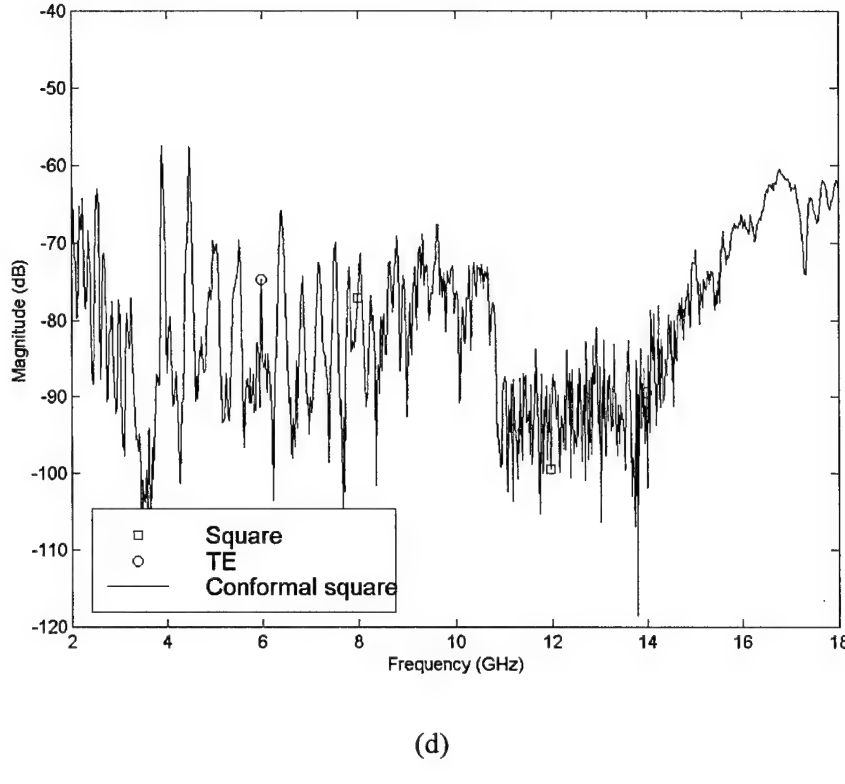
(a)



(b)



(c)



(d)

Figure 48. TE surface wave coupling. On conformal (a) duroid 5880, (b) pec, (c) hexagon HIGP, and (d) square HIGP.

Figure 48 (c), (d) show similar response to Figure 44 (c), (d). Frequencies below 6 GHz have similar response as the duroid sheet which suggest that guided waves exist in the substrate, but the region between 11-14.5 GHz still behaves like a pec plate. For frequencies outside the high-impedance region, the response should be the same as the pec, but instead there is more coupling for the HIGP. Therefore it is most likely that guided waves are coupling through the substrate. The conformal TE measurements are also inconclusive of the band gap behavior because the response is inconsistent with the proposed response for a HIGP, where the high-impedance ground plane should behave as an ordinary pec ground plane outside the band gap.

An alternative method for measuring the TE coupled wave must be developed before the band gap can be conclusively defined.

4.4. Antenna pattern measurements.

4.4.1. Antenna selection and design.

Figure 49 shows the frequency response of the center and outer fed LPD antenna in free space. The frequency sweeps are at horizontal polarization and broadside incidence. The center fed scan has a drop of signal strength below 4 GHz because the lowest resonant dipole (furthest from center) is 5.04 GHz. It is fairly constant over the rest of the band, which is expected for pairs of dipoles. However, below 4 GHz, the outer fed antenna has unexpected gain and a large drop in gain from 10-12 GHz. This dropout occurs in the same region as the surface wave drop out. A possible reason is that the images cancel the pattern. For 11 GHz, the wavelength, λ_g , is 2.04 cm and the substrate thickness is 62 mils (0.4 cm). The antenna was placed 1 mm above the ground plane. Therefore, the total separation between the dipole and its negative image is $\lambda_g/4$ at 11 GHz. Balanis [1:255] shows that this two-element hertzian dipole array has a null at broadside. However, if this were the only reason, then the duroid sample should show the same response, yet it does not.

An additional possibility is that the currents are not exciting the dipoles for those frequencies, but may in fact be resonating the interconnecting lines before reaching the dipoles. Measuring the canted antenna (aligning the interconnect lines with the E-field) provided no insight because the signal was too weak to conclude that to be the cause.

4.4.2. Folded monopole over PEC, Duroid substrate, and HIGP.

As an alternative approach, the monopole technique used by Sievenpiper [19] was duplicated. A one cm horizontal monopole was placed over the absorber, pec, and both HIGP's.

Figure 50 shows the frequency scans for the different configurations while standing wave ratio (SWR) and radiation plots for each are given in Appendix B.

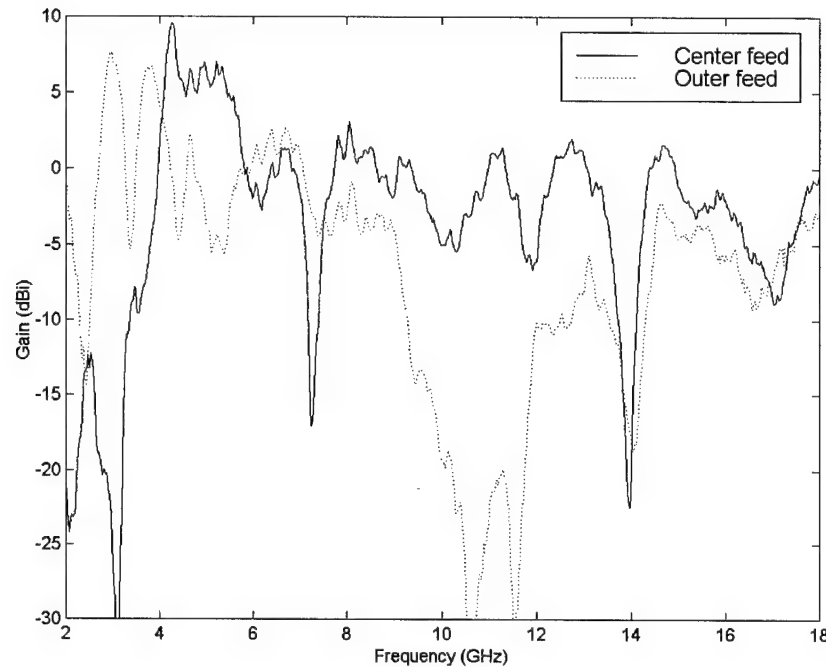
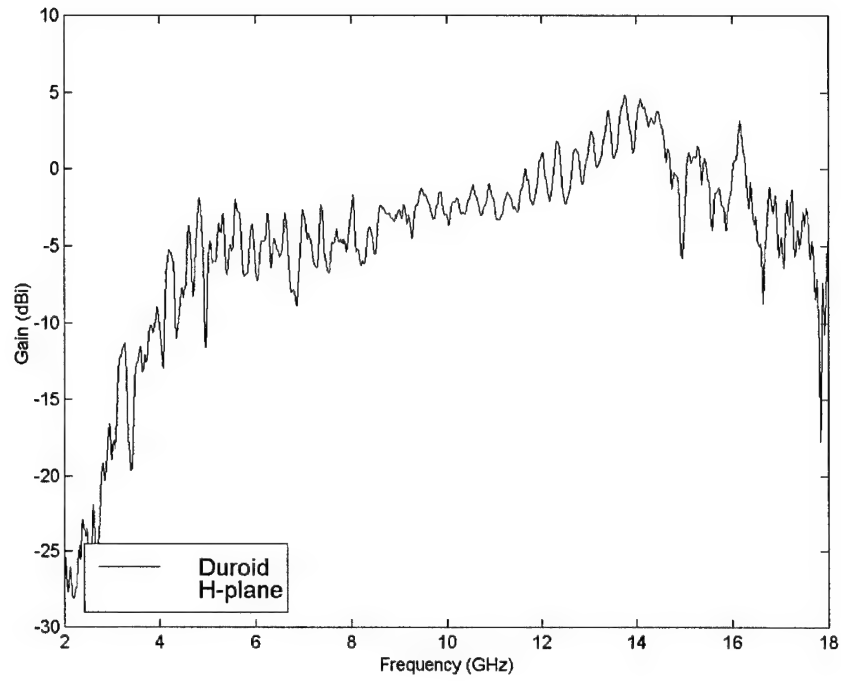
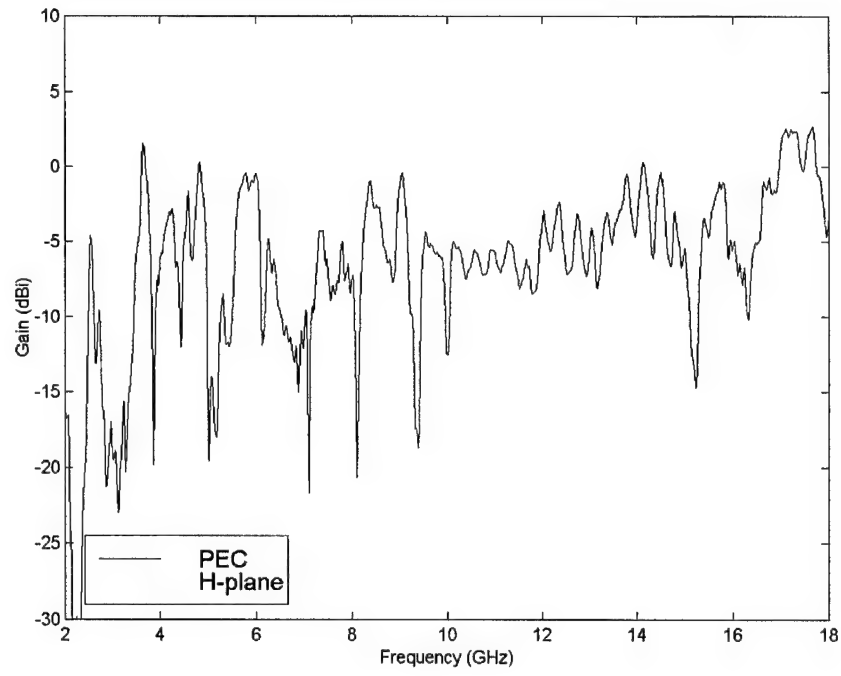


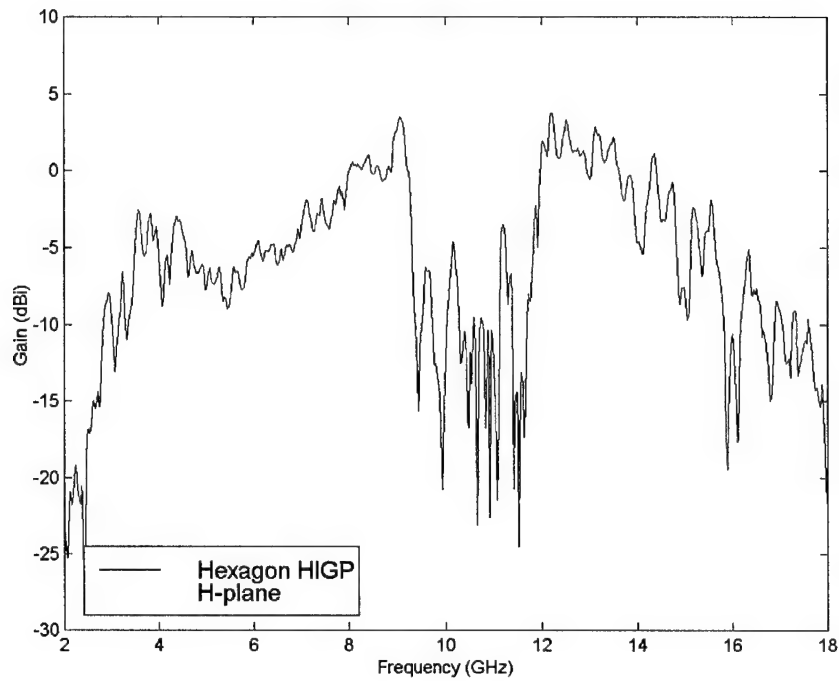
Figure 49. Frequency scan of LPD antenna with different feed locations.



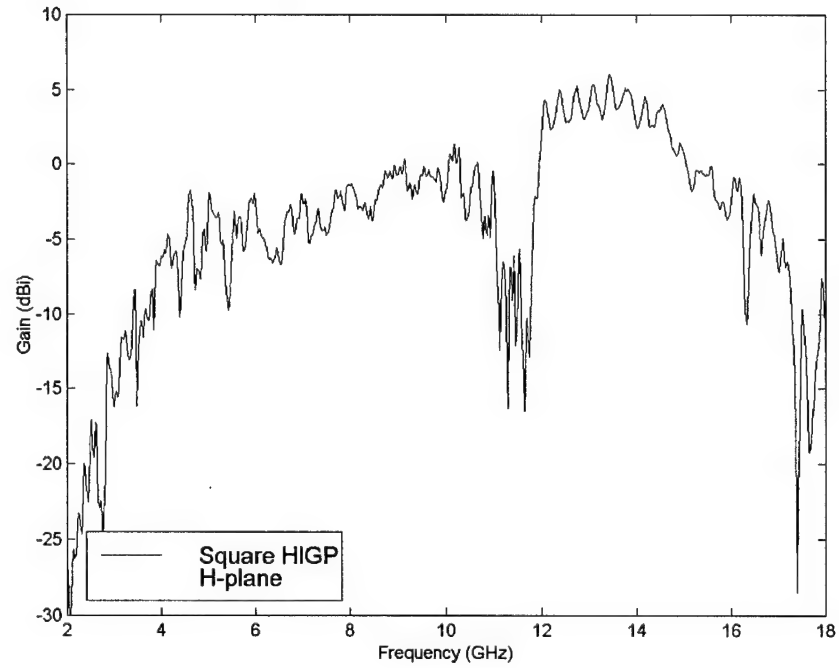
(a)



(b)



(c)



(d)

Figure 50. Frequency scan of monopole antenna above different ground planes. (a) Duroid, (b) PEC, (c) hexagon HIGP, and (d) square HIGP.

The duroid results in a peak value of about 5 dBi at 14 GHz and the pec results are less than 0 dBi across most of the spectrum. The image currents from the PEC cancel the electric current on the monopole, but near 18 GHz, the 1-mm spacing is enough to allow the image to add to the pattern. The HIGP's have an unusual response. Again, there is large drop in signal around 11 GHz. If this is due to image currents, then the duroid sample should show a similar response, yet it does not. A more rigorous analysis could be to use image theory to reduce the HIGP to an array of filamentary magnetic currents (where the monopole is above the slots). Perhaps this would show the measured response. With these unexplained results, the conformal antenna measurements were not completed. Before applying an antenna to this ground plane, more research needs to be accomplished to better understand what other types of antennas could be used with the thumbtack high-impedance ground plane.

5. Conclusions and Suggestions for Further Work

5.1. Review of objectives.

The ultimate antenna goal was to place a conformal printed antenna directly on a conformal high-impedance ground plane and to measure an improved antenna gain and smoother radiation pattern. However, before that goal could be achieved the phase response and surface wave suppression phenomenon of the planar high-impedance ground plane were investigated for establishing a baseline for the conformal surface wave suppression and conformal antenna measurements.

5.2. Conclusions.

The list of conclusions begins with the FDTD code *LC*. Without periodic boundary conditions or lossy materials, *LC* does not accurately model plane wave illumination of periodic structures for workstation use. If plane wave excitation is used, a finer mesh must be defined, which requires vast memory and super computer processing capabilities.

PMM, while not able to model the metal posts, did predict the overall behavior of the HIGP for TE modes. Thus, the TE modes are not influenced by the metal posts.

The reflection coefficient of the high-impedance ground plane does differ for varying polarization and angle of incidence. Therefore, if it is used as an antenna reflector, the antenna should be designed for the mean resonant frequency.

The measured surface wave measurements were not conclusive. Reported results were not duplicated for TM modes and although agreement with TE modes was achieved, the

measurement technique is questionable. At this time, it is unclear if the surface probe measurement technique is a suitable method for measuring surface waves.

Regarding the antenna, careful consideration of the feed structure is required before the thumbtack high-impedance ground plane can be used as an antenna reflector.

The final conclusion is that the surface impedance and effective medium models reported by Sievenpiper are only first order approximations. A more rigorous model is needed before any serious application to broadband or conformal antennas can be performed.

5.3. Recommendations.

5.3.1. Computational electromagnetics.

Recommend exploration of frequency domain techniques such as finite-element method for modeling the high-impedance ground planes. These structures are highly resonant requiring lengthy simulation times in time domain, so a frequency domain technique may be more robust.

5.3.2. Effective medium model.

Recommend investigating the use of PMM and INDIAN (a PMM type code for out of the plane elements). INDIAN may allow a means to model the effective dielectric constant of the metal-posts and substrate. Then, PMM could be run with the effective dielectric constant.

5.3.3. Broadband designs.

Before exploring broadband designs for high-impedance ground planes, recommend a further research into an accurate model of the ground planes. Possible designs may not necessarily include the metal posts.

5.3.4. Antenna applications.

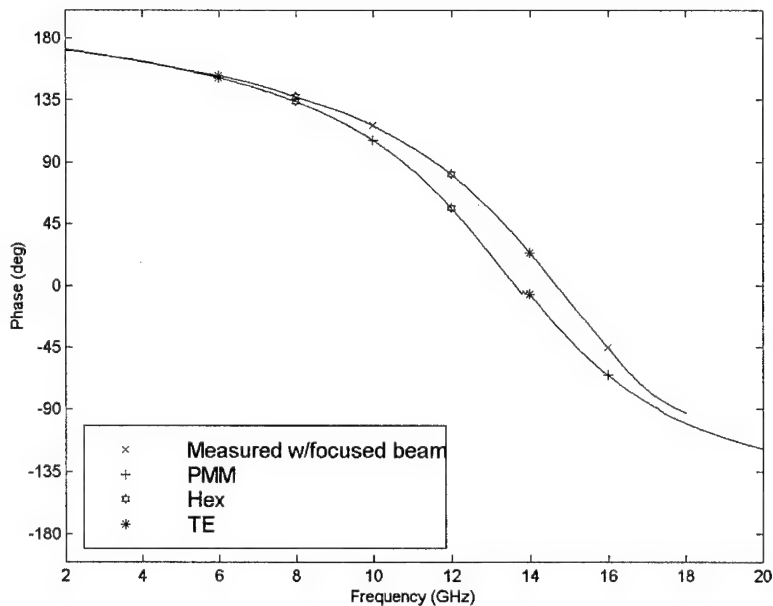
Recommend that a specific antenna application be defined before beginning a broadband or conformal antenna design. The issues of the feed and conformal nature are typically tailored for unique applications, and the ground plane should be as well.

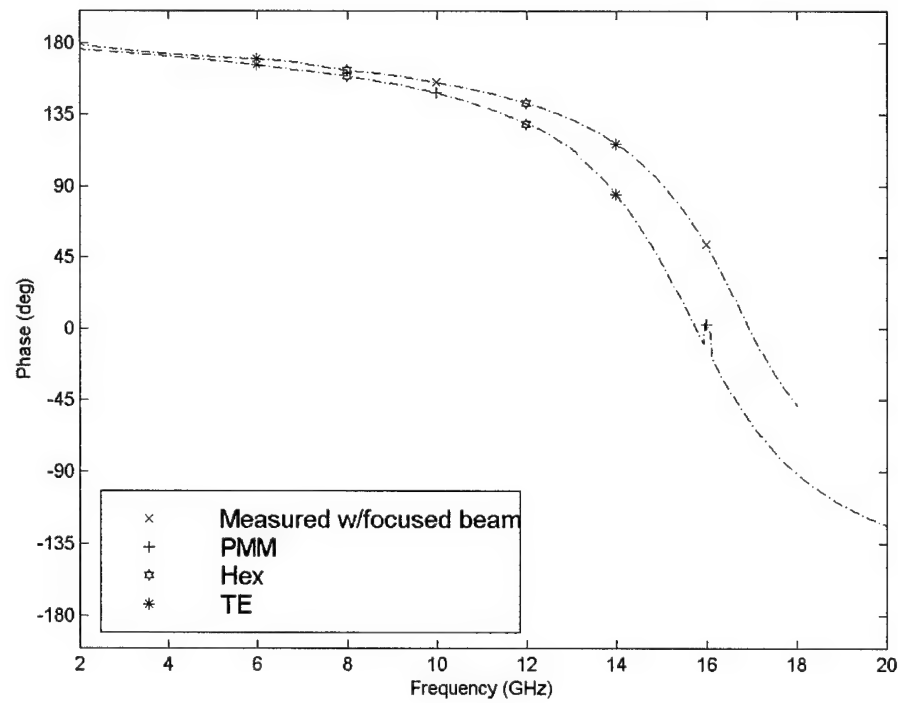
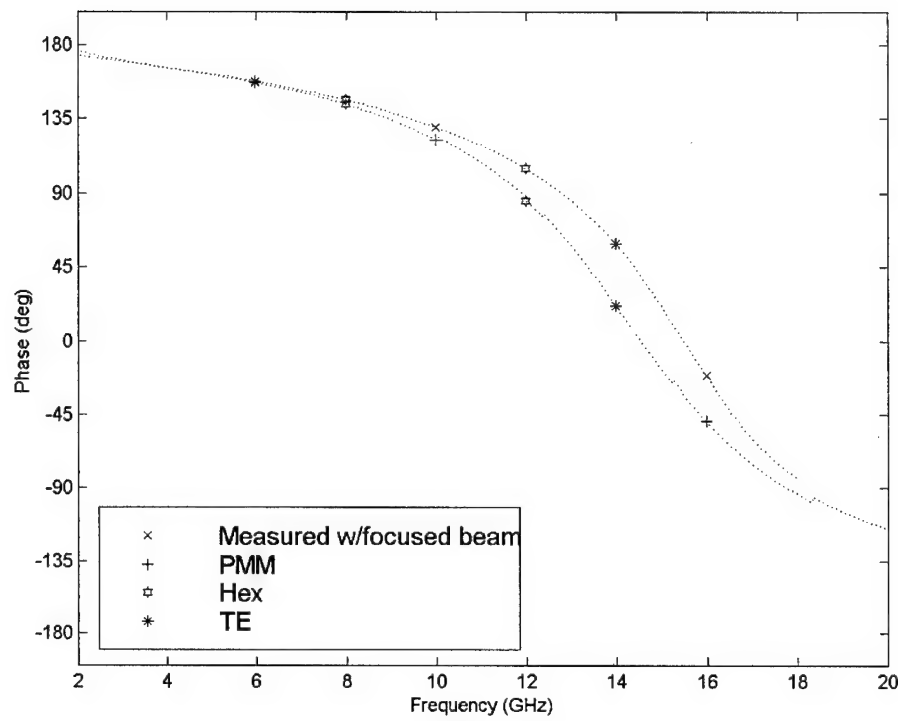
Appendix A. Reflection Measurement Data

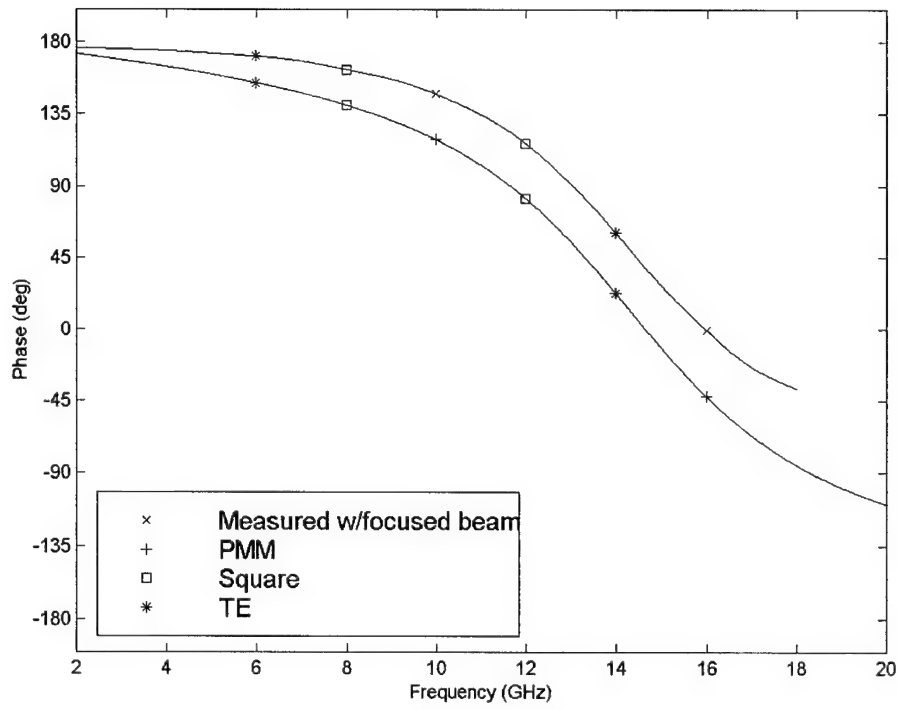
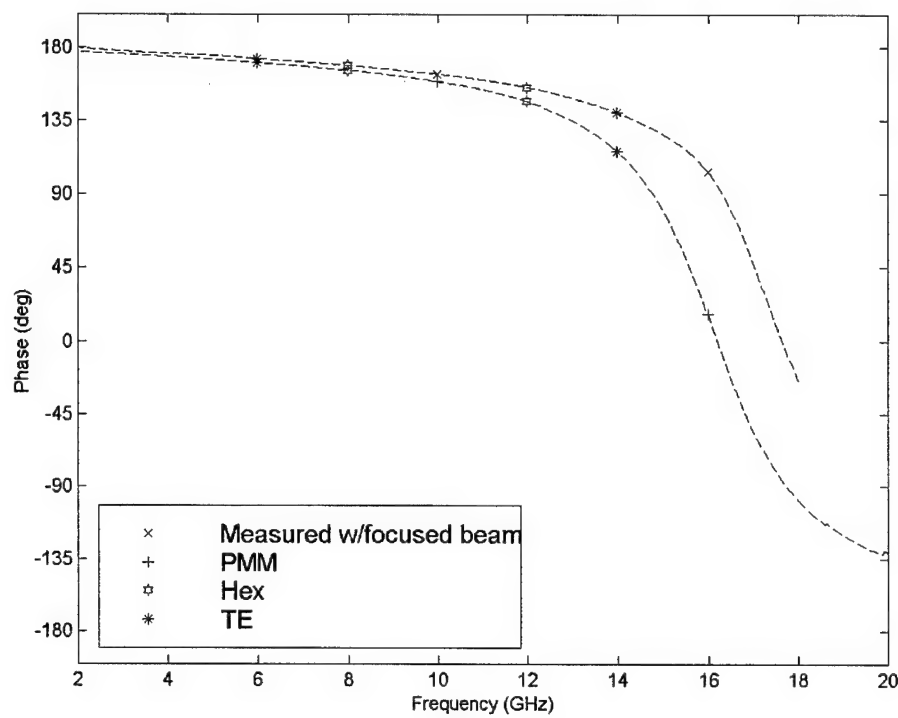
The symbols used in Chapter 4, Section 4.1.2, are repeated here for convenience. The +- and x-symbols are added to denote PMM and measured data, respectively.

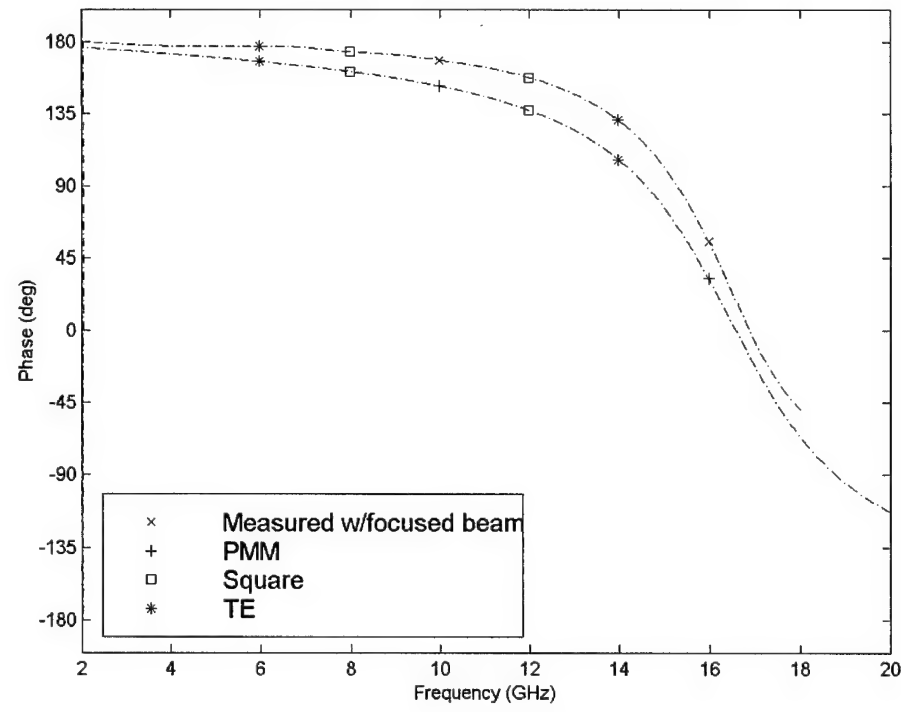
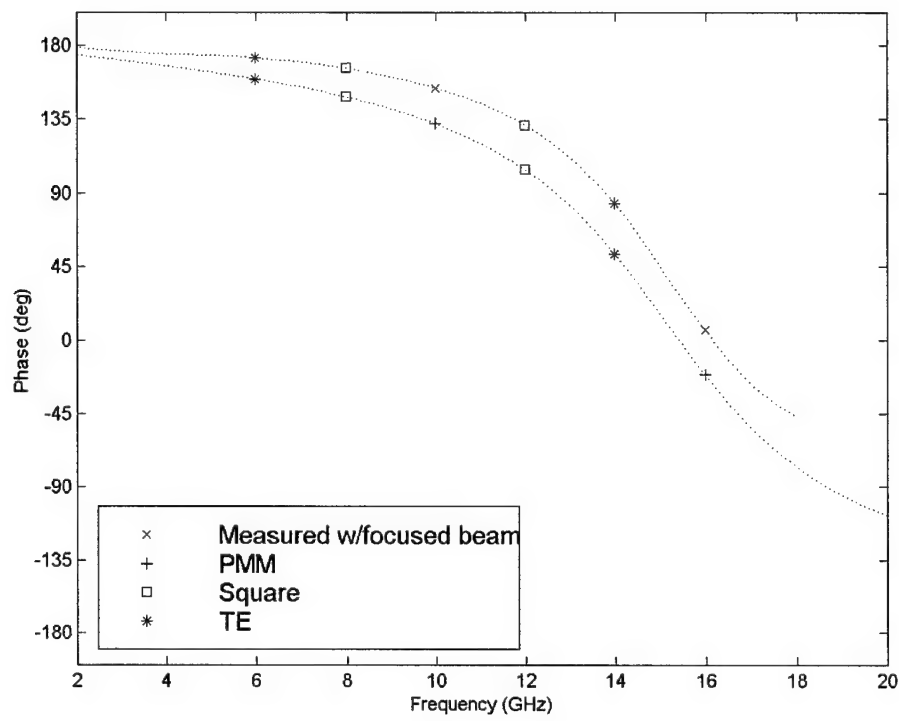
Method	Sample	Polarization	Angle
PMM +	Square: □	TM: *	Normal: solid line
Measured x	Hex: *	TE: ○	35 degrees: dotted line 60 degrees: dash-dot line 70 degrees: dashed line

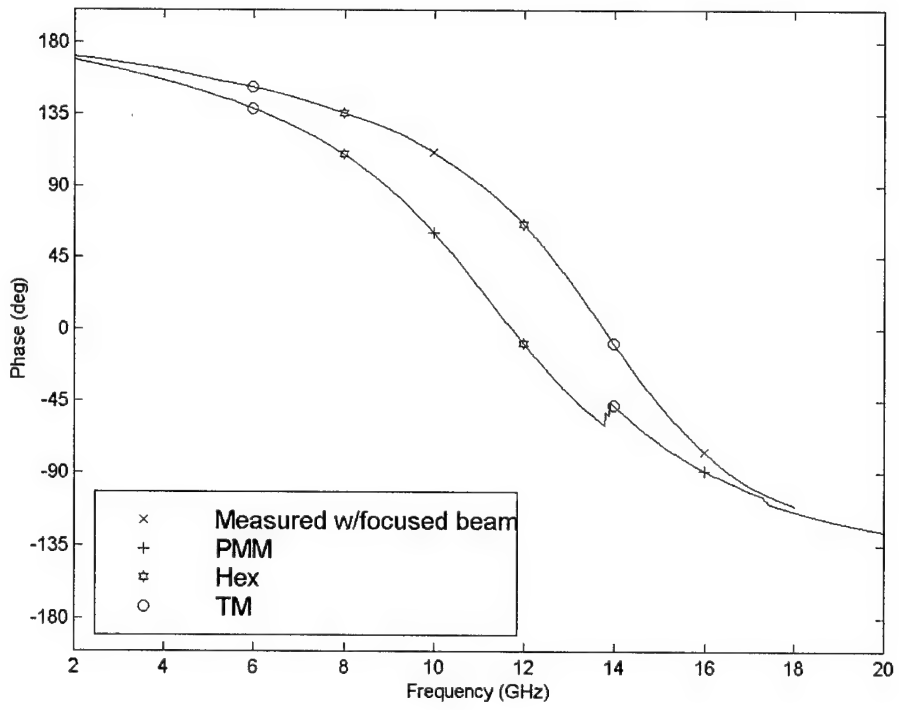
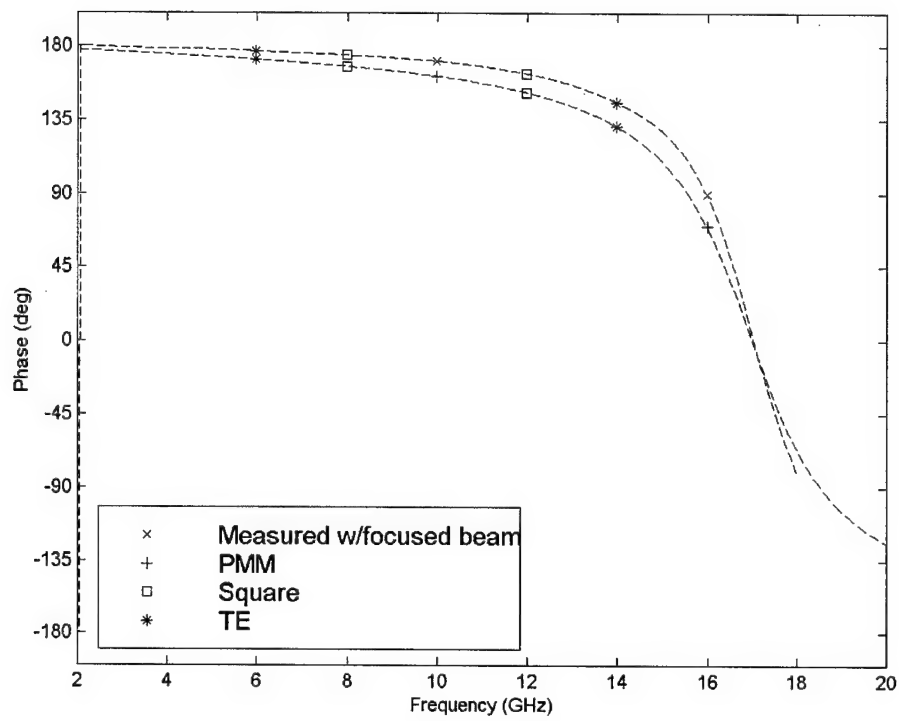
a. Comparison of PMM and GTRI focused beam measurement data.

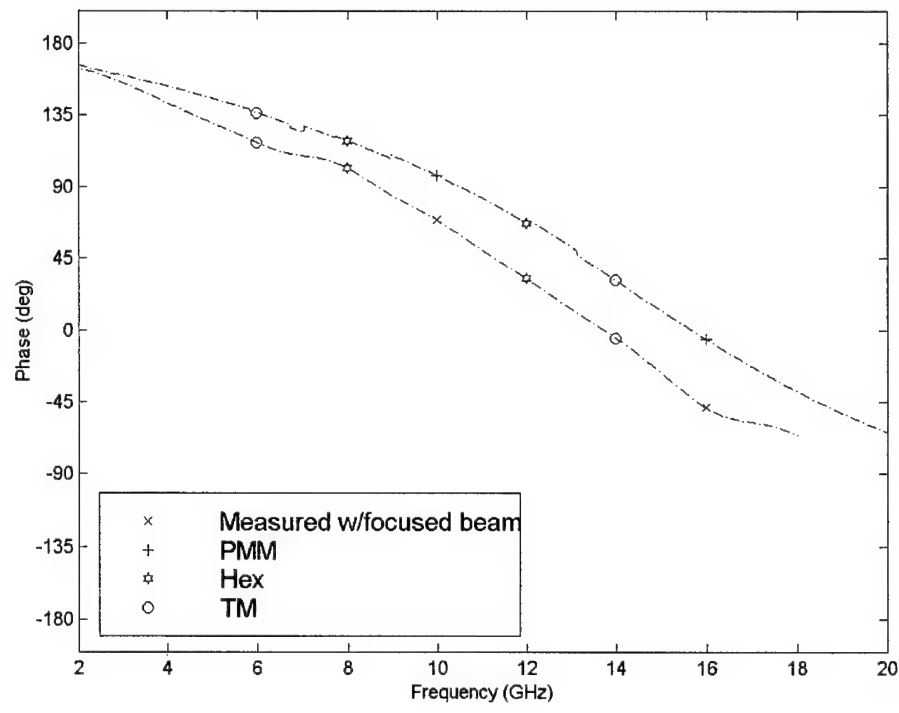
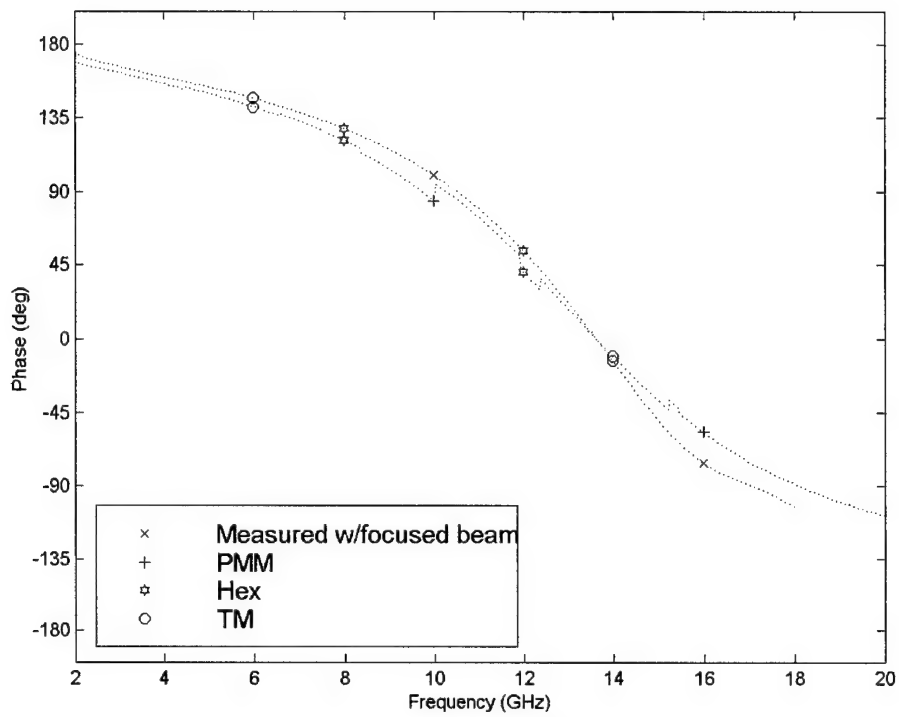


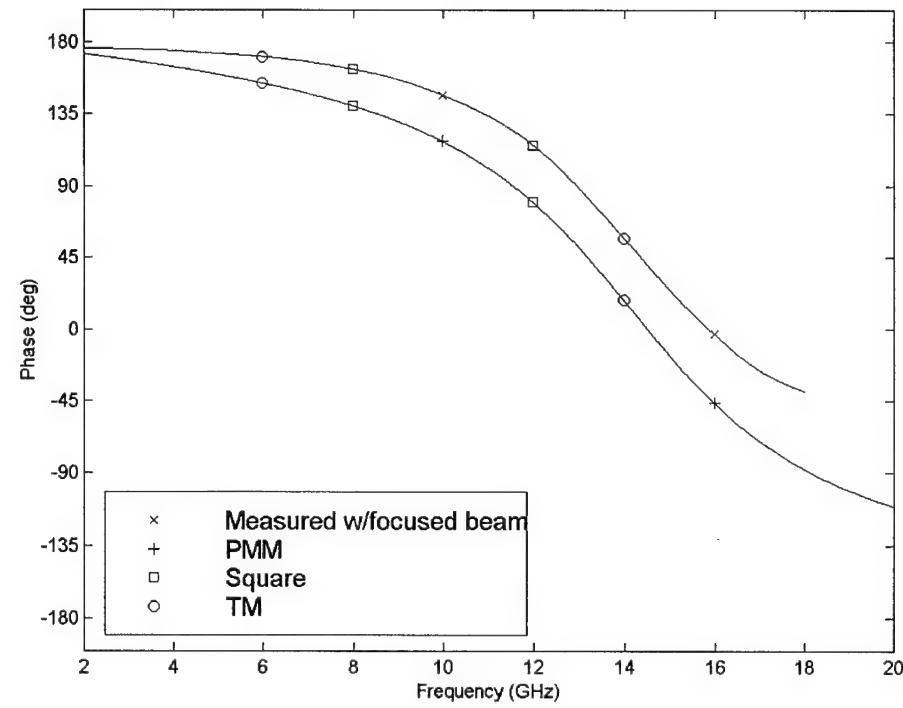
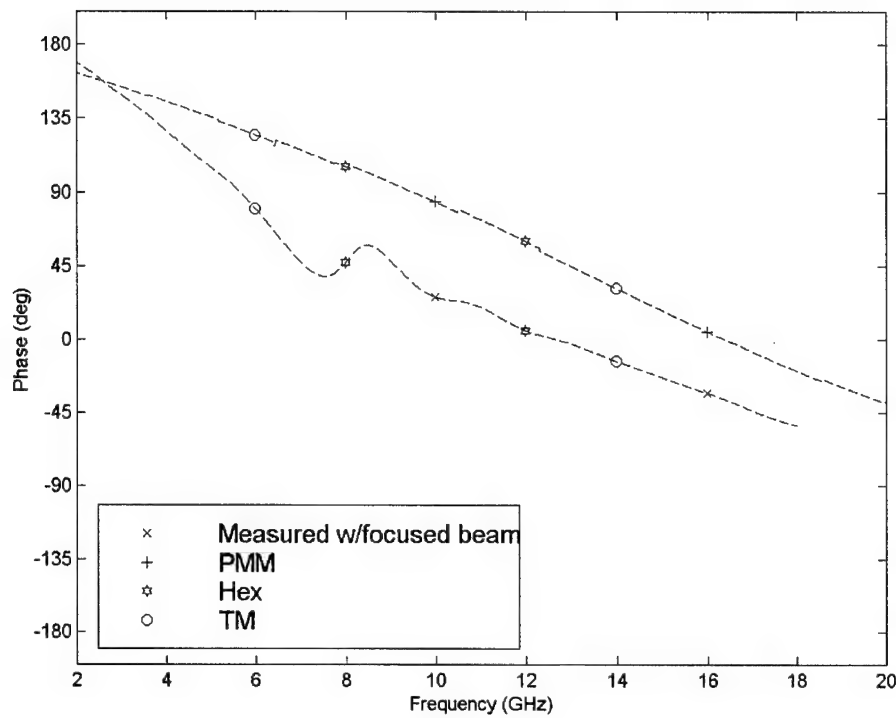


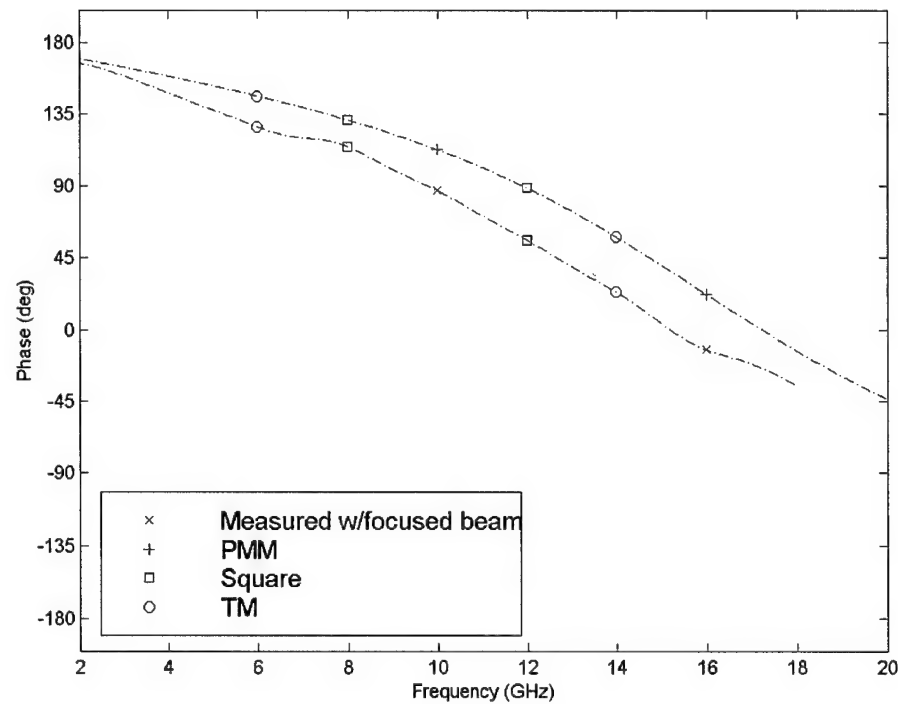
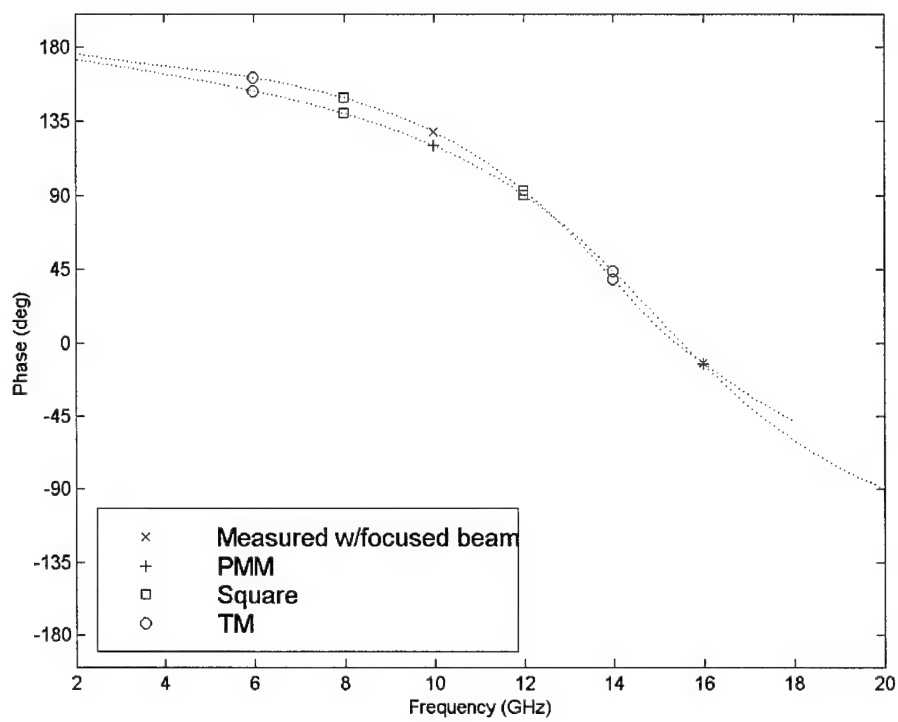


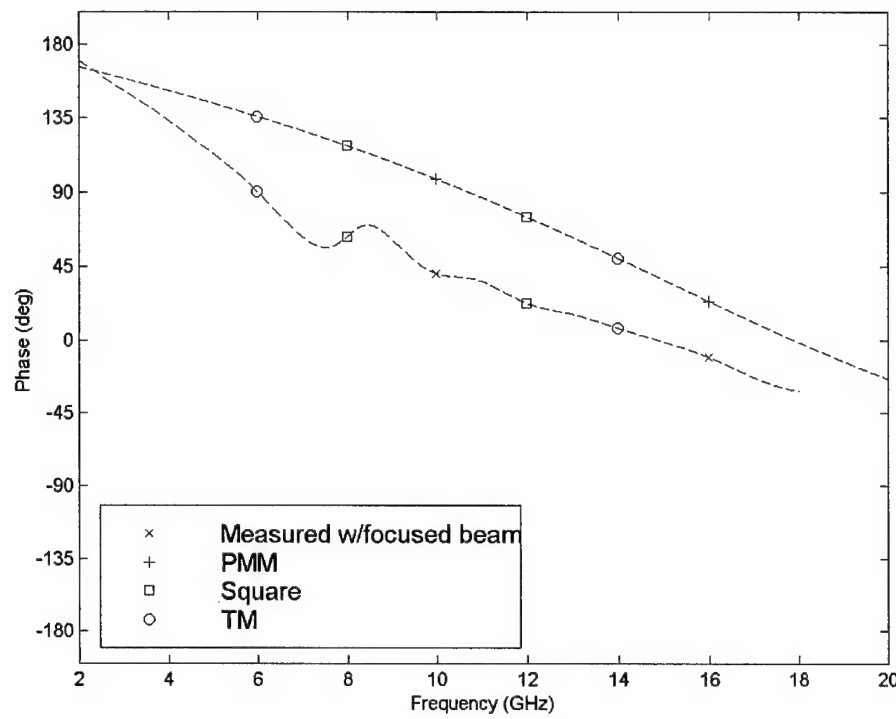




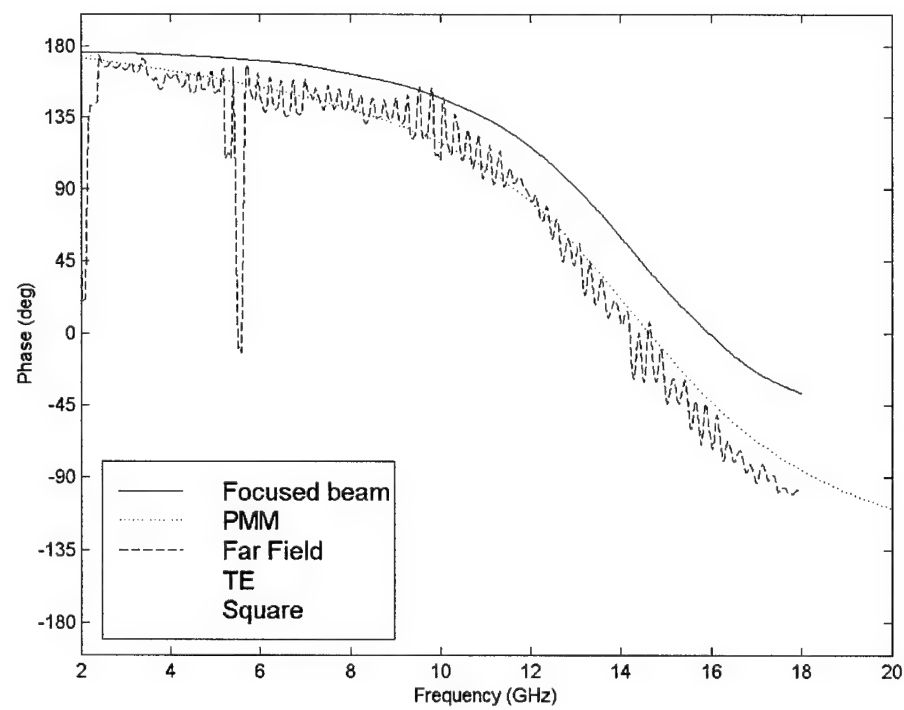
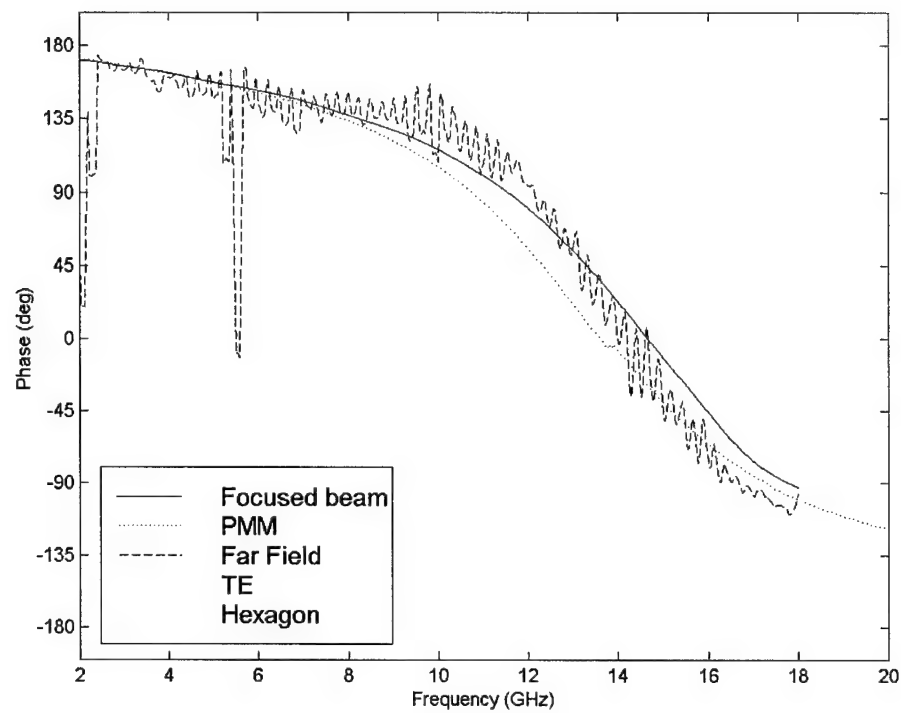


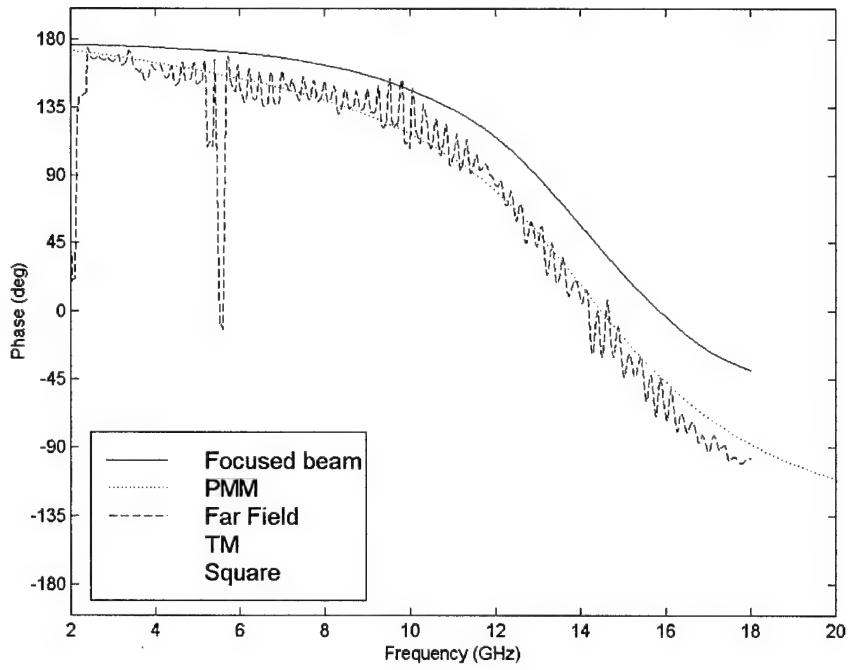
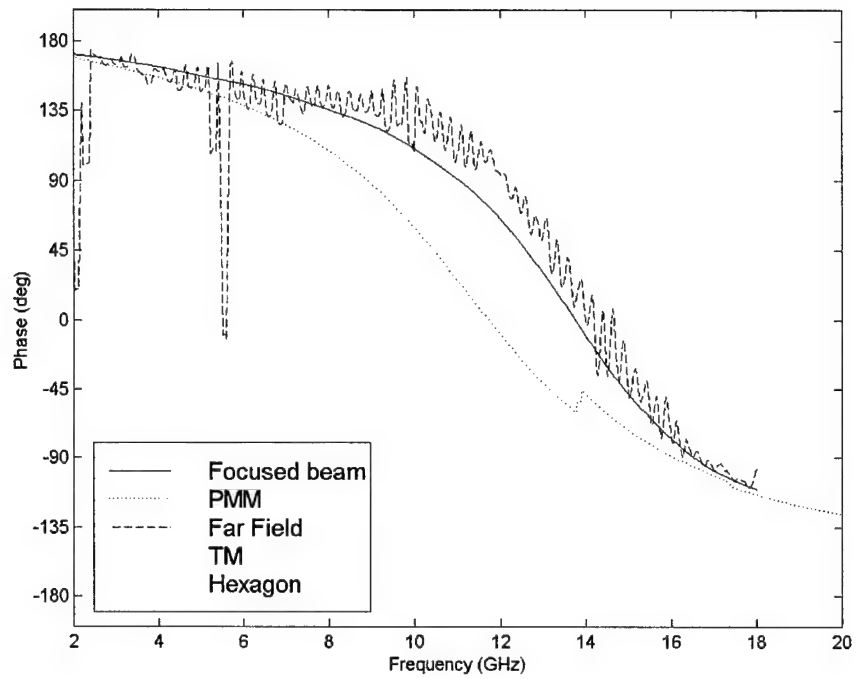






b. Far field reflection measurement data

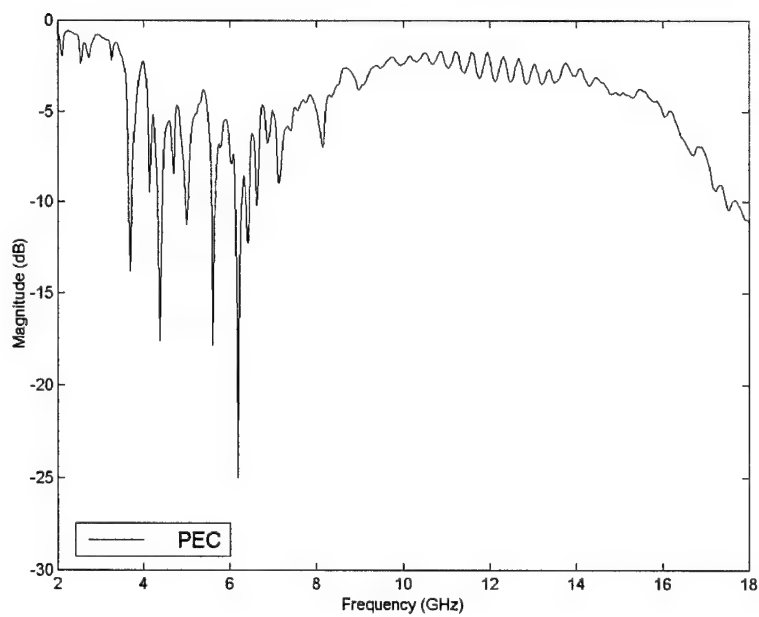
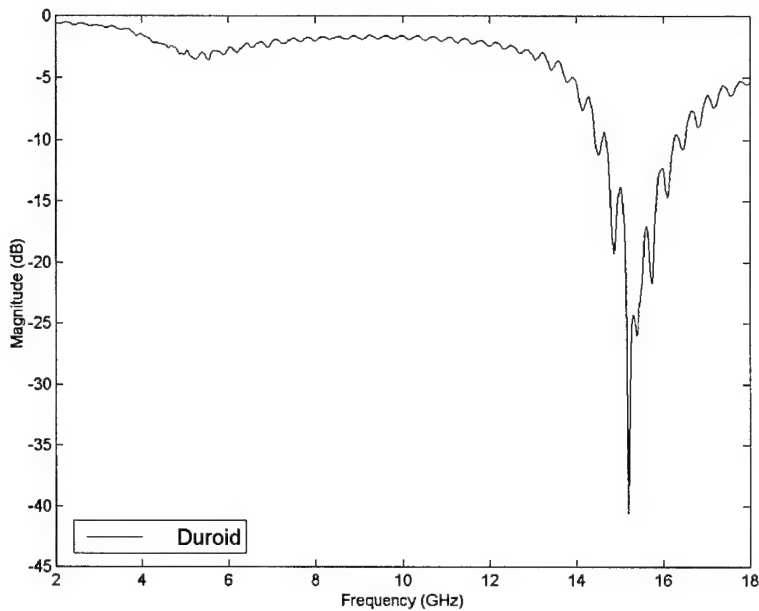


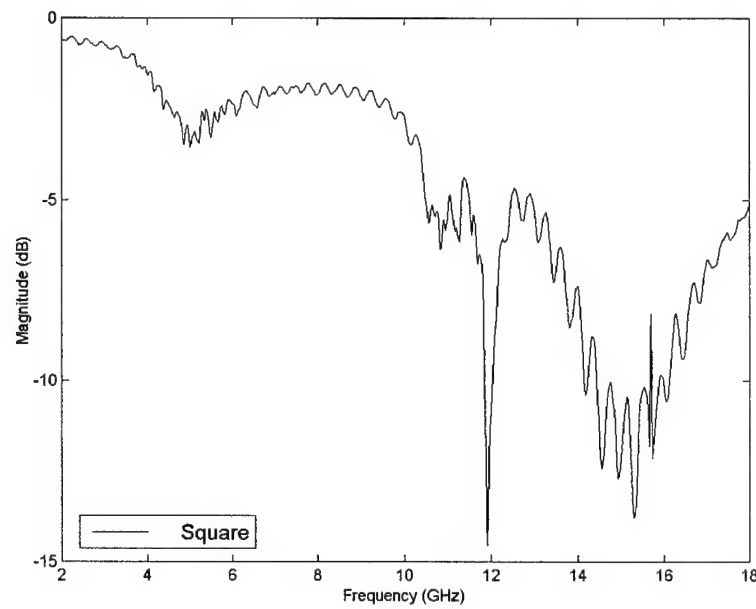
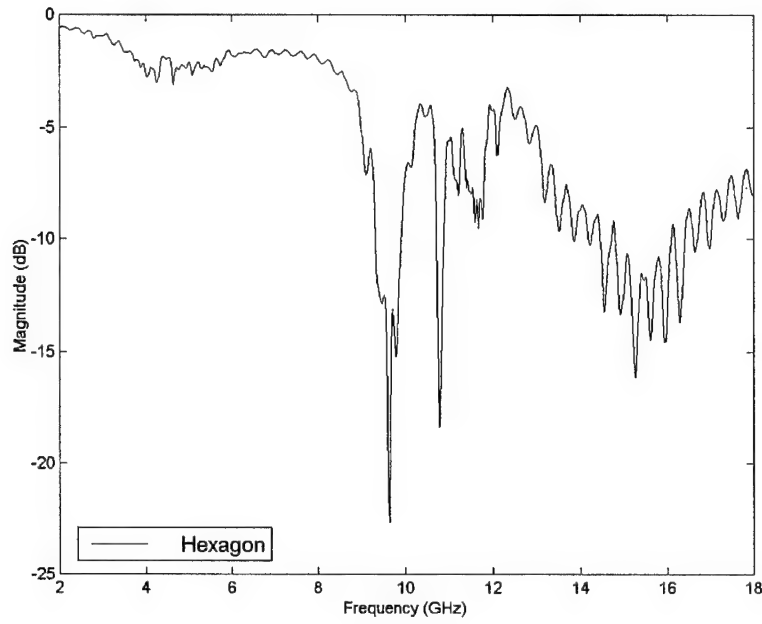


Appendix B. Antenna Patterns.

a. SWR measurements.

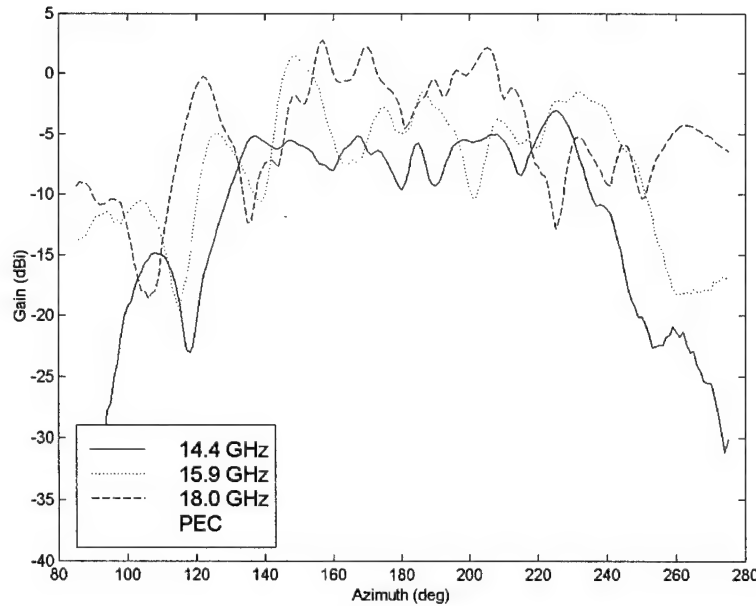
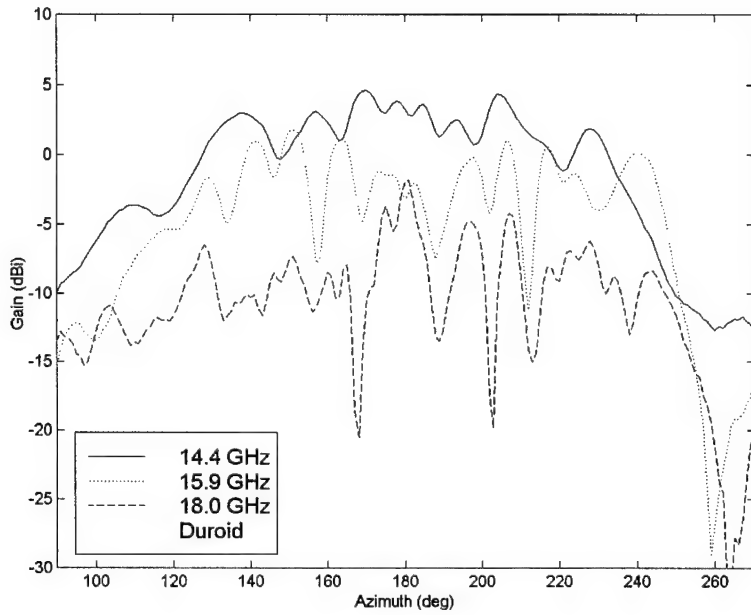
Measured S_{11} data from HP8510.

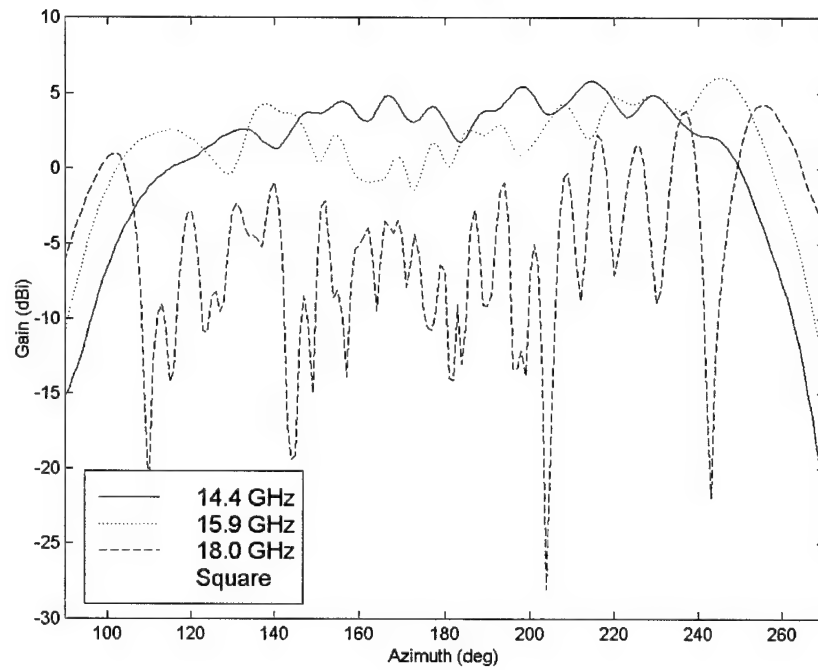
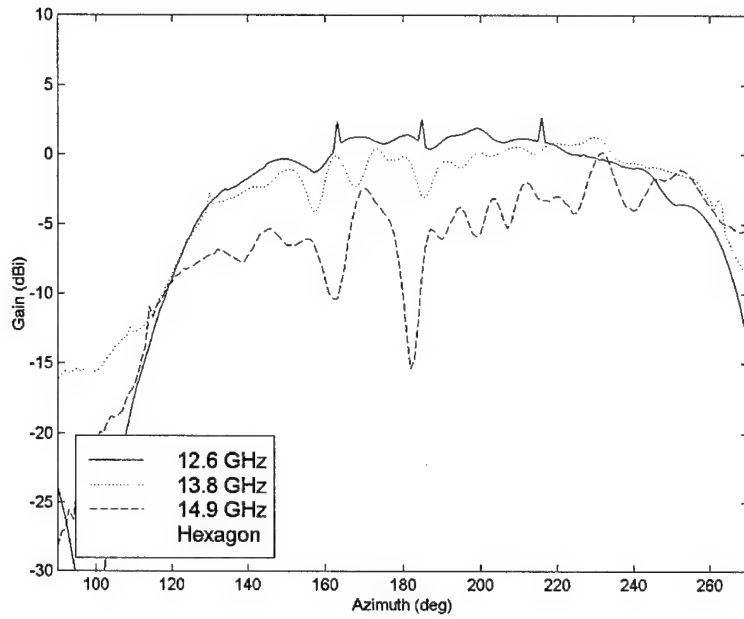




b. E-Plane patterns of monopole antenna.

The frequencies represent the lower band, center band, and upper band frequency when possible. The patterns are from 90 degrees to 270 degrees with 180 degrees being broadside.





References.

- [1] C. A. Balanis, Antenna Theory – Analysis and Design, 2nd edition, New York: John Wiley & Sons, 1997.
- [2] C. A. Balanis, Advanced Engineering Electromagnetics. New York: John Wiley & Sons, 1989.
- [3] E. Yablonovitch, Photonic Band Engineering: Interim Progress Report to US Army Research Office, 1 January 1998-31 December 1998. Contract DAAH04-96-1-0389.
- [4] E. Yablonovitch, "Inhibited Spontaneous Emission in Solid State Physics and Electronics," *Physical Review Letters*, vol. 58, pp. 2059-2062, May 1987.
- [5] E. Yablonovitch, T. J. Gmitter. "Photonic band structures: The face-centered cubic case," *Physical Review Letters*, vol. 63, pp. 1950-1953, Oct. 1989.
- [6] E. Yablonovitch. "Photonic band-gap structures," *J. Opt. Soc. Am. B*, vol. 10, pp. 283-295, Feb. 1993.
- [7] J. Callaway, Energy Band Theory, New York and London Academic Press, 1964.
- [8] E. Yablonovitch, T. J. Gmitter, and K. M. Leung. "Photonic Band Structure: The Face-Centered Cubic Case Employing Nonspherical Atoms," *Physical Review Letters*, vol. 67, pp. 2295-2298, Oct. 1991.
- [9] K. Ho, C. Chan, and C. Soukoulis. "Existence of a Photonic Gap in Periodic Dielectric Structures," *Physical Review Letters*, vol. 65, pp. 3152-3155, Dec. 1990.
- [10] K. Schloer, Antenna Gain Enhancement Using a Photonic Band Gap Reflector, MS thesis, AFIT/GE/ENG/99M-26. School of Engineering, Air Force Institute of Technology, Wright-Patterson AFB OH, Mar. 1999.
- [11] D. Sievenpiper, E. Yablonovitch, J. Winn, S. Fan, P. Villeneuve, J. Joannopoulos, "3D Metallo-Dielectric Photonic Crystals with Strong Capacitive Coupling between Metallic Islands," *Physical Review Letters*, vol. 80, pp. 2829-2832, Mar. 1998.
- [12] J. Joannopoulos, Photonic Crystals: Molding the Flow of Light, Princeton: Princeton Univ. Press, 1995.
- [13] M. Boroditsky, R. Cocciali, E. Yablonovitch, "Analysis of photonic crystals for light emitting diodes using finite difference time domain technique," *SPIE*, vol. 3283, pgs. 184-190, Jan. 1998.
- [14] P. K. Kelly, J. G. Maloney, B. L. Shirley, and R. L. Moore, "Photonic Band Structures of Finite Thickness: Theory and Experiment," *IEEE Ant. & Prop. Symp. Proc.*, pgs 718-721, 1998.
- [15] J. S. Colburn and Y. Rahmat-Samii, "Linear Taper Slot Antenna Directivity Improvement via Substrate Perforation: A FDTD Evaluation," *IEEE Ant. & Prop. Symp. Proc.*, pgs 1176-1179, 1998.

[16] A. S. Barlevy, D. F. Sievenpiper, and Y. Rahmat-Samii. "Photonic Bandgap (PBG) Structures of Multiple Metallic Periodic Screens: Efficient Electromagnetic Characterization," *IEEE Ant. & Prop. Symp. Proc.*, 1216-1219, 1998.

[17] M. Thevenot, C. Cheype, A. Reineix, and B. Jecko, "Directive Photonic-Bandgap Antennas," *IEEE Trans. Microwave Theory Tech.*, vol.47, no. 11, pgs. 2115-2122, Nov. 1999.

[18] D. Sievenpiper, L. Zhang, R.F. J. Broas, N. G. Alexopolous, and E. Yablonovitch, "High-Impedance Electromagnetic Surfaces with a Forbidden Frequency Band," *IEEE Trans. Microwave Theory Tech.*, vol.47, no. 11, Nov. 1999, pgs. 2059-2074.

[19] D. Sievenpiper, High-Impedance Electromagnetic Surfaces, Ph.D. dissertation, University of California at Los Angeles, Los Angeles, CA, 1999.

[20] Y. qian, R. Cocciali, D. Sievenpiper, V. Radisic, E. Yablonovitch, T. Itoh, "A Microstrip Patch Antenna Using Novel Photonic Band-Gap Structures," *Microwave Journal*, pgs 66-76, Jan. 1999.

[21] N. Tea, V. Milanovic, C. Zincke, J. Suehle, M. Gaitan, M. Zaghloul, J. Geist, "Hybrid postprocessing etching for CMOS-compatible MEMS," *Journal of Micromechanical Systems*, vol. 6, no. 4, Dec 1997.

[22] J. S. Zaren, Improving the Performance of Cavity-Backed Antennas by Using Passive Scatterers, MS thesis, AFIT/GE/ENG/94D-34. School of Engineering, Air Force Institute of Technology, Wright-Patterson AFB OH., Dec. 1994.

[23] S. W. Schneider, J. A. Tenbarge, J. Tuss, "Conformal Loadbearing Antenna Structures," *IEEE AP-S Int. Symp. And USNC/URSI National Radio Science Meeting*, pg. 342, Jul. 1999.

[24] L. C. Kempel, "Advances in Modeling Conformal Antennas on Cylinders," *IEEE AP-S Int. Symp. And USNC/URSI National Radio Science Meeting*, pg. 343, Jul. 1999.

[25] LC, An Electromagnetic Anaylsis Tool, Version 2.9, Workstation computer software, <http://lc.cray.com/downloads>, Silicon Graphics, Inc., circa 1999.

[26] A. Taflove, Computational electrodynamics: the finite-difference time-domain method, Boston, Artech House, c1995.

[27] The Ohio State University Electromechanical Laboratory, Introduction to PMM, technical report 715582-5, contract F33615-83-C-1013, Feb. 1986.

[28] K. Ma, F. Yang, Y. Qian, T. Itoh, "A Novel Ground Plane for Wireless Communications Antennas," *IEEE AP-S Int. Symp. And USNC/URSI National Radio Science Meeting*, pg. 234, Jul. 1999.

[29] J. Devore, Probability and statistics for engineering and the sciences, 4th edition, Belmont, Duxbury Press, c1995.

Vita.

Lt Michael A. Saville was born 9 September 1967 in Los Angeles, California. He graduated from Culver City High School in 1985 and enlisted in the Air Force as an Air Traffic Control Radar Maintenance Specialist. He served as Chief, TPN-24 Airport Surveillance Radar Facility and principal trainer for the MPN-14 radar approach control facility while assigned to the 2nd Combat Communications Group, Patrick Air Force Base, Florida and Joint Task Force Bravo, Soto Cano Air Base, Honduras, respectively. When he returned from overseas, he retrained into the Precision Measurement Equipment Laboratory career field and was the assistant lab chief of the F-16/15 Type IV PMEL, 412th Component Repair Squadron, Edwards AFB, California. Then a SSgt, he was recognized with multiple NCO of the quarter and maintenance achievement awards, and Air Force Achievement Medals for outstanding achievement.

In 1994, he was selected for the Airman Education and Commissioning Program and attended Texas A&M University to complete a Bachelor of Science Degree in Electrical Engineering. Graduating with honors, he won the Best Engineering Thesis award for his thesis "Experimental Design of RFID Microstrip Antennas". He attended Officer Training School at Maxwell AFB, Alabama and was commissioned a Second Lieutenant 30 September 1997.

Lt Saville was assigned as an Avionics Engineer with the Defensive Systems Branch, Engineering Division, Aeronautical System Center, Wright-Patterson AFB, Ohio. He provided technical support to the U-2 system program office for defensive system upgrades and developed the modeling and simulation electronic configuration control handbook for the JSF support program office.

In August 1998, Lt Saville entered the School of Engineering, Air Force Institute of Technology, to begin a Master of Science program in Low Observables. While there, he served on the AFIT Student Association Council, and the chapter executive councils of Tau Beta Pi and Eta Kappa Nu honor societies. Upon graduation, 21 March 2000, he proceeded to the Air Force Information Warfare Center, Kelly Air Force Base, Texas. He and his wife Deysi have three children, Michael, Kristen, and Caitlyn.

REPORT DOCUMENTATION PAGE

Form Approved
OMB No. 0704-0188

The public reporting burden for this collection of information is estimated to average 1 hour per response, including the time for reviewing instructions, searching existing data sources, gathering and maintaining the data needed, and completing and reviewing the collection of information. Send comments regarding this burden estimate or any other aspect of this collection of information, including suggestions for reducing the burden, to Department of Defense, Washington Headquarters Services, Directorate for Information Operations and Reports (0704-0188), 1215 Jefferson Davis Highway, Suite 1204, Arlington, VA 22202-4302. Respondents should be aware that notwithstanding any other provision of law, no person shall be subject to any penalty for failing to comply with a collection of information if it does not display a currently valid OMB control number.

PLEASE DO NOT RETURN YOUR FORM TO THE ABOVE ADDRESS.

1. REPORT DATE (DD-MM-YYYY) 15-03-2000			2. REPORT TYPE Master's Thesis		3. DATES COVERED (From - To)	
4. TITLE AND SUBTITLE INVESTIGATION OF CONFORMAL HIGH-IMPEDANCE GROUND PLANES			5a. CONTRACT NUMBER			
			5b. GRANT NUMBER			
			5c. PROGRAM ELEMENT NUMBER			
6. AUTHOR(S) Michael A. Saville, 1Lt, USAF			5d. PROJECT NUMBER			
			5e. TASK NUMBER			
			5f. WORK UNIT NUMBER			
7. PERFORMING ORGANIZATION NAME(S) AND ADDRESS(ES) Air Force Institute of Technology Graduate School of Engineering and Management (AFIT/EN) 2950 P Street, Building 640 WPAFB OH 45433-7765					8. PERFORMING ORGANIZATION REPORT NUMBER AFIT/GE/ENG/00M-17	
9. SPONSORING/MONITORING AGENCY NAME(S) AND ADDRESS(ES) AFRL/SNRP Attn: Dr. Stephen W. Schneider 2241 Avionics Circle WPAFB OH 45433-7333 DSN: 785-4120					10. SPONSOR/MONITOR'S ACRONYM(S)	
					11. SPONSOR/MONITOR'S REPORT NUMBER(S)	
12. DISTRIBUTION/AVAILABILITY STATEMENT APPROVED FOR PUBLIC RELEASE; DISTRIBUTION UNLIMITED.						
13. SUPPLEMENTARY NOTES						
14. ABSTRACT Applique antennas are a long range vision for military vehicles because they are lighter, quicker to replace, less expensive, and can have better performance than conventional antennas. Two newly reported high-impedance ground planes have potential to begin the realization of the applique antenna vision and each is investigated for use with thin conformal antenna structures. Bistatic reflection measurements completely characterize the high-impedance region of planar, thumbtack high-impedance ground planes, and periodic moment method models validate the measurement results. Rigorous planar and conformal surface wave coupling measurements clarify the reported photonic band gap behavior of the thumbtack high-impedance ground plane, and give evidence that the published surface wave suppression results may in fact be inconclusive. In addition, an analysis of variance test identifies the optimum antenna frequency for horizontal wire antenna applications. Broadband antenna applications are explored using a printed log-periodic wire antenna, but unpredicted losses outside the high-impedance region produced inconclusive results and prevented the conformal antenna measurements.						
15. SUBJECT TERMS Periodic Structures, High-Impedance Ground Plane, Periodic Moment Method, Conformal Antenna, Photonic Crystal						
16. SECURITY CLASSIFICATION OF: a. REPORT UNCLASS			17. LIMITATION OF ABSTRACT UL	18. NUMBER OF PAGES 148	19a. NAME OF RESPONSIBLE PERSON Maj Peter Collins (PhD)	
					19b. TELEPHONE NUMBER (Include area code) (937) 255-6565 ext 4304	